UPCONVERTER AND DOWNCONVERTER LUMINESCENT MATERIALS: PROGRESS AND STRATEGIES TOWARDS HIGHLY EFFICIENT PHOTOVOLTAIC SOLAR CELLS

Alessandro Boccolini

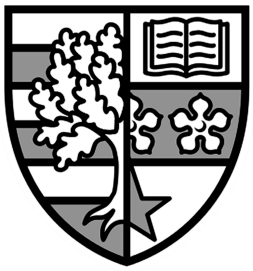

Submitted for the degree of Doctor of Philosophy

Institute of Photonics and Quantum Sciences

School of Engineering and Physical Sciences

Heriot-Watt University

Edinburgh EH14 4AS

United Kingdom

May 2016

Abstract

In this thesis, the downconversion (DC) and upconversion (UC) luminescence properties of rare earth doped materials were investigated for the spectral conversion of part of the solar spectrum, in order to enhance the performances of silicon photovoltaic devices. Significant progress were achieved regarding the understanding of loss mechanisms which limit the photoluminescence quantum yield (PLQY) of those materials. Achieving high PLQY values is of key importance for the successful realisation of DC- or UC-enhanced photovoltaic devices.

It was found that, in high absorbing materials, the PLQY can be reduced drastically by the self-absorption effect. The constraints imparted by this loss mechanism on the optical performances of the luminescent materials were determined using a one dimensional optical model developed by the author. The model was also experimentally validated via spectroscopic characterisation of a downconverting co-doped Ce^{3+}/Yb^{3+} borate glass.

The role of self-absorption within an hypothetical DC-enhanced photovoltaic (DC-PV) device was investigated to find out the physical performance limitations of the device. Moreover, an UC material consisting of Er^{3+}-doped hexagonal sodium yttrium fluoride (β-NaYF4) was theoretically investigated to look at the implications of self-absorption on two experimental situations: the case of a PLQY measurement, and on the effective performance in a UC-enhanced photovoltaic (UC-PV) device. The study demonstrates that an optimization of the thickness is essential in order to reduce the effect of self-absorption and maximize the possible additional photocurrent that could be harvested, and that the optimal thickness takes different values depending on the case considered.

As a major progress, an UC material consisting in barium yttrium fluoride (BaY_2F_8) single crystal doped with Er^{3+} was optically characterised resulting in a measured external photoluminescence quantum yield (ePLQY) of 12.1±1.2 % for a BaY_2F_8:30at%Er^{3+} sample of thickness 1.75±0.01 mm, and a measured internal photoluminescence quantum yield (iPLQY) of 14.6±1.5 % in a BaY_2F_8:20at%Er^{3+} sample with a thickness of 0.49±0.01 mm. Both values were obtained under excitation at 1493 nm and an irradiance of 7.0±0.7 Wcm^{-2}. The reported iPLQY and ePLQY values are among the highest achieved for monochromatic excitation in this research field. Finally, the losses due to self-absorption were estimated in order to evaluate the maximum iPLQY achievable by this promising UC material. The estimated iPLQY limit values were ∼19%, ∼25% and ∼30%, for 10%, 20% and 30% Er^{3+} doping level, respectively.

The self-absorption model clarifies the origin of the disparity between the theoretical and the experimental PLQY reported for some materials. The results from this work assist with the design and implementation of DC and UC layers for photovoltaic devices, as well as providing a framework for optimization of luminescent materials to other fields of optics and photonics.

Acknowledgements

I would like to thank Heriot-Watt University for having supported my PhD studies through the "James-Watt PhD Scholarship".

I would like to express my full gratitude to Prof. Bryce S. Richards, for giving the opportunity to pursue this PhD within Heriot-Watt University, and to Dr Robert R. Thomson for the excellent support received through the last part of my PhD.

I also would like to thank Prof. Mauro Tonelli, from University of Pisa, for providing the upconverter samples, and for the additional support received during my studies here and back in Pisa.

A big thank you also to all the people I met in this wonderful city, which helped in making this experience fulfilling and positive: my group mates Jonathan, Sean, Yiorgos, Jose, Dorothy, Junjie, Dave, Thymios, Dalila, Gudrun, Aruna, Diego, Eliyas and Paolo; the HWU friends Leonardo, Rosario, Aurora, Andrea, Daniele, Eleonora, Christina, Nathan, Silvia, Alessandro, Daniel, Wojciech, Mandy, Theo and Solenn; my Edinburgh friends Marco, Jana, Sam, Natalia, Eilidh and Blanca.

Finally, a special thanks to my wife Alice, with whom I am sharing the beauty that this wonderful city and this beautiful country offer to us. I am also grateful to my family and Alice's family for their love and support I have received through all my life.

Bimbi, dè, grazie anche a tutti voi amici Pisani ormai sparsi a giro per il mondo, che avete sempre tifato per me!

ACADEMIC REGISTRY
Research Thesis Submission

Name*:*			
School/PGI:			
Version: *(i.e. First, Resubmission, Final)*		Degree Sought (Award **and** Subject area)	

Declaration

In accordance with the appropriate regulations I hereby submit my thesis and I declare that:

1) the thesis embodies the results of my own work and has been composed by myself
2) where appropriate, I have made acknowledgement of the work of others and have made reference to work carried out in collaboration with other persons
3) the thesis is the correct version of the thesis for submission and is the same version as any electronic versions submitted*.
4) my thesis for the award referred to, deposited in the Heriot-Watt University Library, should be made available for loan or photocopying and be available via the Institutional Repository, subject to such conditions as the Librarian may require
5) I understand that as a student of the University I am required to abide by the Regulations of the University and to conform to its discipline.

* *Please note that it is the responsibility of the candidate to ensure that the correct version of the thesis is submitted.*

Signature of Candidate*:*		Date:	

Submission

Submitted By *(name in capitals):*	
Signature of Individual Submitting:	
Date Submitted:	

For Completion in the Student Service Centre (SSC)

Received in the SSC by *(name in capitals):*			
Method of Submission *(Handed in to SSC; posted through internal/external mail):*			
E-thesis Submitted ***(mandatory for final theses)***			
Signature:		Date:	

Please note this form should bound into the submitted thesis.

Updated February 2008, November 2008, February 2009, January 2011

Contents

1 Introduction **1**

1.1 Motivation 1

1.2 Fundamental Losses in Solar Cells 2

1.3 The Shockley-Queisser Limit 5

1.4 Reducing Losses via Spectral Conversion 7

1.5 Upconversion and Downconversion for Photovoltaics 8

1.6 Thesis Overview 10

2 Photonic Materials for Photovoltaics Applications **12**

2.1 Solar Energy Research 13

2.1.1 Historical Background 13

2.1.2 First Generation Solar Cells 17

2.1.3 Second Generation Solar Cells 18

2.1.4 Third Generation Solar Cells 20

2.2 Fundamentals of Photovoltaic Solar Cells 22

2.2.1 Solar Spectrum 23

2.2.2 Photon Electron Conversion 25

2.2.3 Equivalent Circuit of a Photovoltaic Solar Cell 27

2.2.4 Power Conversion Efficiency 30

2.2.5 The Shockley-Queisser Detailed Balance Limit 31

2.3 Theory of Rare Earths Doped Luminescent Materials 36

2.3.1 Overview on Rare Earths Elements 36

2.3.2 Energy Levels of Rare Earth Doped Materials 39

2.3.3 Energy Transfer Processes 44

2.3.4 Downconversion and Upconversion Mechanisms 46

2.3.5 Multiphonon Relaxation 48

2.4 Beyond the Shockley-Queisser Limit 51

2.4.1 Downconversion and Upconversion Enhanced PV Devices . . . 51

2.4.1.1 DC-PV device efficiency limit 52

2.4.1.2 UC-PV device efficiency limit 53

3 Materials and Methods **55**

3.1 Material Synthesis Methods 56

3.1.1 Ce^{3+}/Yb^{3+} Co-Doped Borate Glass 56

3.1.2 Er^{3+} Doped BaY_2F_8 Single Crystal 57

3.1.3 Polishing Techniques 58

3.2 Material Characterisation Methods 59

3.2.1 Absorption Measurements 59

3.2.2 Photoluminescence Measurements 66

3.2.3 Light Sources 69

3.2.4 Detectors 71

3.2.5 Determination of Absolute Photoluminescence Quantum Yields 72

3.2.6 Integrating Sphere 73

4 Ce^{3+}/Yb^{3+} Co-Doped Downcovnerting Borate Glasses: Effect of Self-Absorption 75

4.1 Downconversion for Solar Cells 76

4.1.1 Downconverters Based on Yb^{3+} Co-Doped Materials 76

4.1.2 Absorption Measurements 81

4.1.3 Photoluminescence Spectra 82

4.1.4 Photoluminescence Spectra Dependence on Yb^{3+} Concentration 83

4.2 Modelling Self-Absorption Losses 84

4.3 Experimental Validation Using Ce^{3+}/Yb^{3+} Borate Glasses 89

4.4 Conclusions 92

5 Role of Self-absorption on Downconversion and Upconversion Enhanced PV devices 93

5.1 Impact of Self-Absorption Losses on DC-PV Devices 94

5.2 Impact of Self-Absorption Losses on UC-PV Devices 96

5.3 Conclusions 103

6 Highly Efficient Upconversion in Er^{3+} Doped BaY_2F_8 Crystals 105

6.1 Upconverters Based on Erbium Doped Materials 106

6.1.1 State of the Art 106

6.2 Methodology 109

6.3 Results and Discussion 111

6.3.1 Absorption Measurements 111

6.3.2 Photoluminescence Quantum Yield Measurements 114

6.3.3 Estimation of Self-Absorption Losses 120

6.4 Conclusions 123

7 Conclusions 125

Bibliography 127

List of Tables

2.1 Rare earths elements. 37

5.1 Fitted parameters A and B and iPLQY values with their corresponding log-log slope at different power densities (150 Wm^{-2}, 970 Wm^{-2} and 10^6 Wm^{-2}) for different Er^{3+} doping levels. 100

6.1 Absorption coefficients relative to three different Er^{3+} concentration and at different wavelengths. 112

6.2 ePLQY and iPLQY values measured for all investigated samples and corresponding to 3 different excitation wavelenghts: 1556 nm, 1524 nm and 1493 nm. 119

List of Figures

1.1 Fundamental losses in a single p-n junction PV solar cell. 3

1.2 Fundamental losses within a solar cell depending on the energy bandgap. 5

1.3 Shockley-Queisser limit. 6

1.4 Spectral mismatch between the solar cell absorption spectrum and the incident solar spectrum. 7

1.5 Ideal design of a spectral conversion enhanced PV device. 9

2.1 Wall painting from the Uffizi Gallery, Stanzino delle Matematiche, in Florence, Italy. 13

2.2 Bell solar battery installed by an engineer in 1954. 15

2.3 Solar cell efficiencies chart. 16

2.4 Design evolution of first generation solar cells.a) Space silicon cell design developed in the early 1960s. b) The "Black" cell (1974). c) The passivated emitter, rear locally diffused (PERL) cell developed in the 1990s. 17

2.5 Schematic illustration of three different second generation thin film PV devices. In all three devices, cadmium telluride (CdTe, copper indium gallium selenide (CIGS) and amorphous silicon (a-Si), the layers are deposited onto a glass superstrate that allows sunlight to enter through the top layer, the transparent conducting oxide (TCO). The electrical current and voltage are produced in the lower layers. . 19

2.6 Schematic of a typical multijunction solar cell. The cell is composed by three sub-cells having different energy bandgap, each one converting different regions of the solar spectrum. 20

2.7 Comparison of solar spectrum outside Earth's atmosphere (orange), at sea level (blue), and the spectral radiance $S_\lambda(\lambda, T)$ of a black body at temperature 5800 K (dotted black line). 24

2.8 Air mass coefficient dependence on zenith angle. The AM1.5 solar spectrum, corresponding to a Zenith angle of 48.2°, represents the average illumination for US and European latitudes. 25

2.9 Equivalent circuit of a PV solar cell. A current generator represents the photogenerated carriers converted from sunligth that are flowing through an ideal diode (p-n junction). The equivalent circuit also includes a series resistance (R_s) and shunt resistance (R_{sh}) representing the internal losses of the solar cell. 27

2.10 V-I curve comparison between an ideal diode (solid line) and an illuminated solar cell (dotted line). The vertical shift is due to the presence of the current I_L connected to the photogenerated electron-hole pairs. 29

2.11 V-I curve characteristic of a PV solar cell intersecting the linear V-I curve of a load resistance (R_{load}), whose slope is proportional to $\frac{1}{R_{load}}$. The intersection between the two curves is called the solar cell's operating point. 29

2.12 Output current (dashed red) and output power (black solid) of a solar cell. The current and voltage values I_{max} and V_{max} corresponding to the maximum output power P_{max} have been highlighted. 30

2.13 Short-circuit current density J_{sc} versus the energy bandgap E_g. . . . 33

2.14 J-V curve for different bandgap energies $E_g = 0.8$ eV (solid line), $E_g = 1.4$ eV (dashed line) and $E_g = 2.0$ eV (dotted line). 35

2.15 (a) Open-circuit voltage V_{oc} and (b) power conversion efficiency η versus energy bandgap E_g. 36

2.16 Schematic of the electronic configuration of a trivalent rare earth ion. The unfilled 4f valence shell lies between the core electrons and the outer (filled) shell $5s^2 5p^6$. Each rare earth element is characterised by the different number of electrons populating the 4f shell. 38

2.17 Radial distribution function (density P^2 vs distance r) of 4f, 5s, 5p and 6s shell for a Gd^+ ion. 39

2.18 Schematic of the atomic interactions causing the 4f manifold splitting. 42

2.19 Dieke energy level diagram. 43

2.20 Energy transfer mechanisms. 45

2.21 Downconversion mechanism via cross-relaxation. 46

2.22 Schematic of the upconversion mechanism. 47

2.23 Two photons upconversion mechanisms. Two photons upconversion mechanisms: (a) energy transfer upconversion (ETU), (b) two-steps absorption, (c) cooperative sensitisation, (d) cooperative luminescence, (e) second harmonic generation, (f) two-photon absorption excitation. 47

2.24 Non-radiative multiphonon transition rate dependence on the temperature. 50

2.25 Downconversion and Upconversion Enhanced PV Devices. 51

3.1 Ce^{3+}/Yb^{3+} Co-Doped borate glass. 56

3.2 Czochralski method. 58

3.3 Boule of Barium yttrium fluoride (BaY_2F_8) single crystal. 58

3.4 BaY_2F_8 sample cut and polished. 59

3.5 LaboPol-1 polishing machine from Struers integrating a self-made sample holder. 60

3.6 Sample holder. 60

3.7 Grinding process. 61

3.8 Absorption in a medium of thickness L. 61

3.9 Absorption and emission processes in a two-level quantum system. a) Ground state absorption/Excited state absorption, b) spontaneous emission, c) stimulated emission. 62

3.10 Spectrophotometer *Perkin-Elmer Lambda 950*. 63

3.11 Schematic of the optical system of Perkin Elmer Lambda 950 spectrophotometer. 64

3.12 Edinburgh Instrument FLS920 spectrofluorometer. 66

3.13 Internal schematic of the spectrofluorometer Edinburgh Instrument FLS920. 67

3.14 Gratings response 68

3.15 Sample chamber of the spectrofluorometer Edinburgh Instrument FLS920. 68

3.16 Xe900 450 W Xenon arc lamp emission spectrum. 69

3.17 HP-Agilent 8168F tunable laser. 70

3.18 μF900 microsencond pulsed flashlamp emission spectrum. 70

3.19 Extended Red and NIR PMT detector's spectral response. 71

3.20 Spectralon reflectivity. 73

3.21 Integrating sphere scheme. 74

4.1 First-order downcoversion. 77

4.2 Second-order downcoversion via cooperative energy transfer (CET). . 78

4.3 Schematic of downconversion (DC) via CET in Ce^{3+}/Yb^{3+} system. . 79

4.4 UV/VIS/NIR absorption spectrum for the sample Ce0.5%-Yb1%. The inset graph shows the NIR absorption for four different Yb^{3+} molar concentrations. 81

4.5 Overlapping of absorption and emission spectrum in the near infrared (NIR) region for the sample Ce0.5%-Yb1%. 82

4.6 Emission spectra for different Yb^{3+} doping level concentration and relative emission branching ratio. 83

4.7 Schematic diagram of the 1D DC model scheme. 85

4.8 ePLQY calculated for a specific case. 89

4.9 Emission spectra for Ce^{3+} 0.5 %mol -Yb^{3+} 1%mol of varying thicknesses. 90

4.10 Integrated fluorescence relative to the peak at 978nm. 91

5.1 ePLQY dependence on thickness and doping concentration. 95

5.2 iPLQY data taken from Ivaturi *et al.* plotted together with the fitted curves defined by Eq.5.2 for each Er^{3+} molar concentration 99

5.3 UC emission in two different experimental situations 101

5.4 Simulated ePLQY using Eq.5.1 for the $NaYF_4$:Er^{3+}(25%) as a function of thickness, for three different pump power densities in the two configurations described in Fig.5.3. 102

5.5 Maximum ePLQY achievable 103

6.1 Two sub-bandgap photons are converted into a higher energy photon by an UC layer placed underneath a bifacial solar cell. 106

6.2 Experimental setups used for photoluminescence measurements, with (a) and without (b) integrating sphere. 110

6.3 Absorption coefficient spectra in the range 1400-1650 nm of the investigated Er^{3+} doped BaY_2F_8 crystals for doping levels of 10%, 20% and 30%. 111

6.4 Comparison of solar spectrum AM1.5D and a 1.73 mm thickness BaY_2F_8:30%Er^{3+} optical density 113

6.5 Comparison of emission spectrum (measured without integrating sphere) and ground state absorption spectrum in the range 950-1050 nm . . . 115

6.6 NIR photoluminescence spectra measured for 3 different excitation wavelengths: 1556 nm, 1524 nm and 1493 nm. 117

6.7 Normalized NIR photoluminescence spectra measured for 3 different excitation wavelengths: 1556 nm, 1524 nm and 1493 nm. 120

6.8 Estimated losses due to self-absorption comparing the integrated emission spectra measured in the integrating sphere and without integrating sphere. 121

List of Acronyms

μc-Si microcrystalline silicon.

a-Si amorphous silicon.

BaY_2F_8 barium yttrium fluoride.

c-Si crystalline silicon.

CdTe cadmium telluride.

CET cooperative energy transfer.

CIGS copper indium gallium selenide.

DC downconversion.

DC-PV downconversion enhanced photovoltaic device.

ePLQY external photoluminescence quantum yield.

EQE external quantum efficiency.

ESA excited state absorption.

ETE energy transfer efficiency.

ETU energy transfer upconversion.

FWHM full width at half maximum.

GSA ground state absorption.

iPLQY internal photoluminescence quantum yield.

IR infrared.

$LaCl_3$ lanthanum chloride.

LED light emitting diode.

mc-Si multicrystalline silicon.

NA numerical aperture.

NIR near infrared.

OD optical density.

PLQY photoluminescence quantum yield.

PMT photomultiplier tube.

PV photovoltaic.

RE^{3+} trivalent rare earth.

STC standard test conditions.

UC upconversion.

UC-PV upconversion enhanced photovoltaic device.

UV ultraviolet.

VIS visible.

VUV vacuum ultraviolet.

Chapter 1

Introduction

1.1 Motivation

In 2011 the size of world's population reached 7 billion, and is expected to increase up to 10 billion by 2060 [1]. The high growth rate, which has mostly affected the less developed countries of Asia and Africa, is also accompanied by a rapid industrial development of those countries and by a massive urbanisation process [2]. To sustain this ongoing trend an increasingly higher energy supply is required.

The large availability of fossil fuels, like oil, natural gases and carbon, as well as the support of nuclear energy, have been sufficient so far for meeting the global energy demand. In fact, nowadays more than 80% of the total primary energy supply is provided by fossil fuels and nuclear power [3].

However, it is well-known that those are finite resources, which will inevitably run out in a not too far future. Beyond that, they are recognised to have a negative impact on the global environment. Fossil fuels are the primary cause of carbon dioxide emissions [4], while nuclear power presents several issues regarding storage, recycling and disposal of nuclear waste [5]. The use of alternative viable resources becomes necessary to meet the increasing energy demand and to progress towards the direction of a more sustainable approach to energy production.

Renewable energies, such as wind, solar, hydroelectric, geothermal and biomass, represent both a clean and inexhaustible resources for the production of energy and for this reason they gained major attention in the last decades [6].

Among them, solar energy represents a vast resource, which could in principle meet the world's needs for clean power generation. A common argument used to support this statement comes from the fact that the Sun provides Earth with as much energy every hour as human civilization uses every year (170,000 TWh) [7].

Clearly, it is not possible to collect the whole solar radiation incident on the Earth's surface, and we also have to consider that the device allowing the conversion of solar energy into electricity, the *photovoltaic (PV) solar cell*, could not harvest the whole solar spectrum.

Currently, PV solar cells have reached record efficiencies up to 46% using costly technologies like multijunctions solar cells. However, the actual PV market is dominated by silicon technology [8], whose record efficiency currently reached 27.6% [9].

Despite its lower efficiency, silicon technology still represents the best cost-effective solution, and it is expected to dominate the PV market for the next decades [10]. For these reasons, achieving higher efficiency PV solar cells utilising a well-established technology, like silicon, is economically convenient.

In this thesis we will focus on one possible way to improve the efficiencies of silicon-based PV devices, taking advantage of the spectral conversion properties of rare-earth doped luminescent materials, which could be used to reduce some of the fundamental losses that occur in a traditional solar cell.

1.2 Fundamental Losses in Solar Cells

A traditional silicon-based PV solar cell consists of a single p-n junction (a solid-state semiconductor diode) equipped with metal contacts on the top and on the bottom of the device.

Due to the existence of an inaccessible energy gap in the band-like electronic structure of semiconductor materials, incident light on a solar cell could only be absorbed if the photons possess an energy greater than a certain threshold value, the *energy bandgap*.

Its value depends on the type of semiconductor material employed, and it determines the energy separation between the valence band and the conduction band. A photon with energy above the energy bandgap is absorbed by the p-n junction and promotes an electron from the valence to the conduction band, leaving a positively charged hole in the valence band. The resulting carriers are then collected by the conductive metal contacts, which allow the current to flow in an external electrical load.

The resulting external quantum efficiency (EQE) of the solar cell, defined as the number of photogenerated electrons per incident solar photon, may vary considerably depending on the wavelength of the incident radiation. In fact, not all photons coming from the Sun can be absorbed, and also not all the photons absorbed by the cell eventually leads to charge generation. This is due to the existence of different fundamental losses, which are schematised in Fig. 1.1.

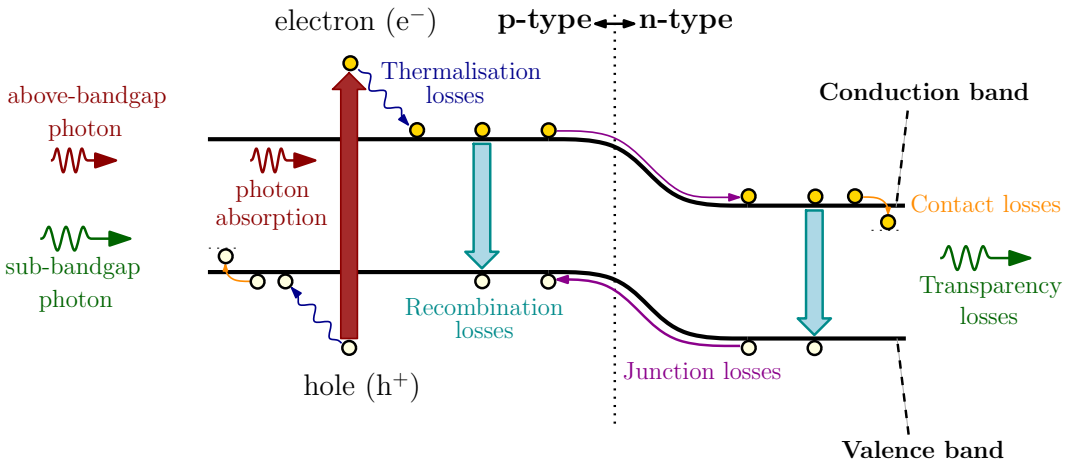

Figure 1.1: Fundamental losses in a single p-n junction PV solar cell. Adapted from [11]

The fundamental losses that can occur in a single p-n junction solar cell are:

- ***Transparency losses***. This include all those photons with energy below the semiconductor bandgap (sub-bandgap photons) which are not absorbed by the solar cell.
- ***Thermalisation losses***. Absorbed photons with energy much greater than the bandgap excite electrons at higher states of the conduction band, which eventually relax to the band edge. This relaxation is called *thermalisation* and it mainly causes an electron kinetic energy loss which is dissipated as heat.
- ***Recombination losses***. Every electron-hole pair formed in a p-n junction is in a meta-stable state, which means that both carriers tend to annihilate each other. The annihilation, more commonly referred as *recombination*, could be *radiative*, releasing a photon with energy close to the energy bandgap, or *non-radiative*, thus without emitting any photon. The latter effect is known as Shockley-Read-Hall recombination [12], and it is caused by the presence of defects in the semiconductor.
- ***Junction losses***. This includes the loss of energy of electrons flowing through the junction interface between the n-type and p-type layers which leads to a voltage drop.
- ***Contact losses***. Those losses are similar to the previous as they involve again a voltage drop, which in this case is due to the junction between the semiconductor and the metal contacts.

Junction and contact losses usually represent just a few percent of the total dissipated energy (1%). Instead, the major losses mechanisms are due to thermalisation losses, transparency losses and electron-hole recombination losses. As calculated by Shalav *et al.* [11], the amount of those losses is bandgap dependent (see Fig. 1.2).

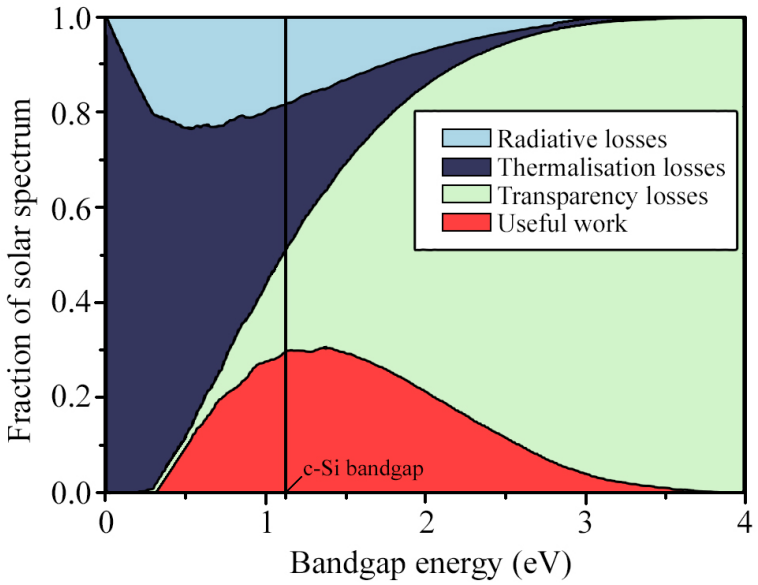

Figure 1.2: Fundamental losses within a solar cell depending on the energy bandgap. Adapted from [11].

According to Fig.1.2, for a bandgap of 1.12 eV (crystalline silicon (c-Si) bandgap) the amount of transparency losses results about 20% of the total energy provided by the Sun, and 30% is the amount of losses caused by thermalisation. The useful work that can be extracted is 30%, and is called the *Shockley-Queisser limit*.

1.3 The Shockley-Queisser Limit

The Shockley-Queisser [13] limit refers to the maximum theoretical energy efficiency conversion that could be achieved by a solar cell based on a single p-n junction.

It was proposed in 1961 by Shockley and Queisser as a way to calculate the solar cell limitations using a non-empirical method, i.e. not requiring all different cell parameters to be known. Their calculation is based on the principle of detail balance, which states that, at equilibrium, each elementary process should be equilibrated by its reverse process.

In their study the elementary process taken in consideration is the generation of electrons-hole pairs by photon absorption, while the reverse process its their radiative recombination. The photons are provided by the Sun, which is supposed

to have the same emission spectrum of a blackbody radiation at a temperature of 6000 K.

Shockley and Queisser found an efficiency limit of 33% for an optimal bandgap energy of 1.4 eV, while for a bandgap of 1.12 eV (case of c-Si) the efficiency resulted limited to 30% (see Fig. 1.3).

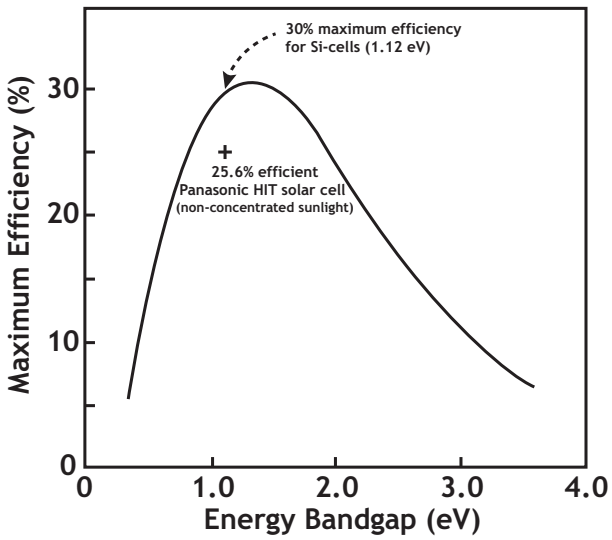

Figure 1.3: Maximum PV efficiency which can be obtained for a given energy bandgap. The curve's maximum represents the so-called Shockley-Queisser limit. The figure has been adapted from [13]. The additional point shows the current world record silicon PV efficiency measured at Panasonic laboratory under non-concentrated sunlight.

In Fig. 1.3 the best experimental efficiency measured for non-concentrated light (25.6% Panasonic HIT Solar Cell [14]) has been plotted to show that current research has been able to get closer to the fundamental limit described by Shockley-Quiesser.

The energy conversion efficiency limit originates from the fundamental losses taking place within the solar cell. By reducing those losses, not only we are able to approach the Shockley-Queisser limit, but we can actually overcome the limit because the lossless system would change the assumptions of the detailed balance treatment.

Therefore, the Shockley-Queisser limit represents an ultimate limit only for a device based on a single p-n junction in its simplest form. Every improvement involving the device optimisation, such as the employment of new materials, has to

be regarded as a new system and will be characterised by its own limit. Overcoming the Shockley-Quiesser limit is not against the laws of physics but it is actually something feasible.

The "ultimate" efficiency limit for a generalised system converting sunligth into electricity is the so called *thermodynamic limit*. In this case the solar cell is described has a heat engine undergoing a Carnot cycle within the temperature of the Sun (5800 K) and the temperature of the absorber (300 K) and the maximum efficiency results 93% [15].

1.4 Reducing Losses via Spectral Conversion

The primary cause of the fundamental losses in a solar cell is the so called *spectral mismatch* between the incident solar spectrum and the solar cell absorption spectrum.

Figure 1.4 displays the mismatch in the case of a silicon solar cell transparent for photons with wavelength longer than 1100 nm.

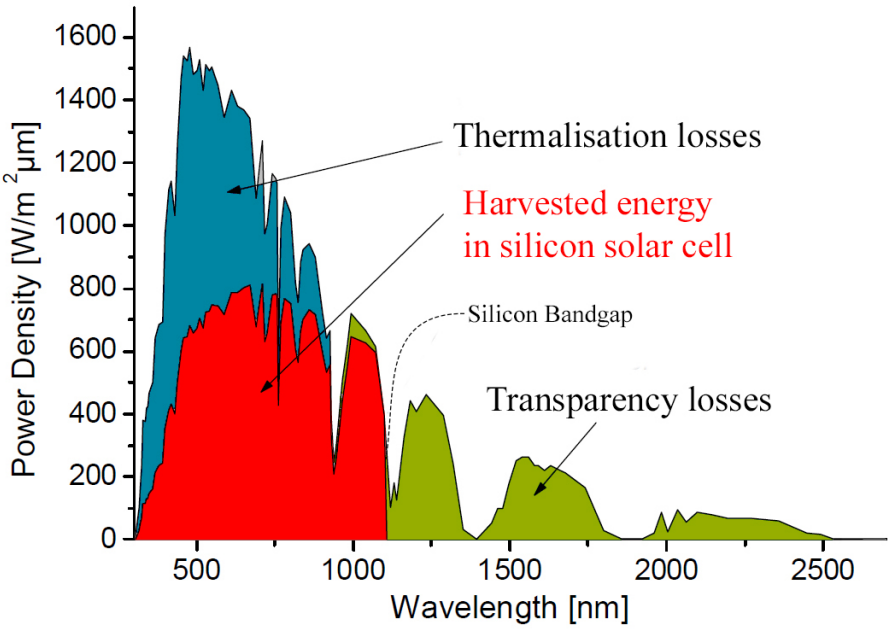

Figure 1.4: Spectral mismatch between the solar cell absorption spectrum and the incident solar spectrum. Adapted from [16].

Different approaches to solve the spectral mismatch problem have been reviewed

[17–19] and will be presented later in Section 2.1.4. One of those approaches, which will be the main topic of this thesis, is to use *spectral conversion*.

The idea behind it, is to effectively modify the solar spectrum incident on the solar cell, employing photoluminescent materials in which absorbed light can be downconverted (one high-energy photon into two low-energy photons) or upconverted (two low-energy photons to one high-energy photon). The resulting down- or upconverted emission is absorbed and efficiently converted into electricity as it is emitted in a spectral region where the solar cell performs at its best, i.e. close to the energy bandgap.

1.5 Upconversion and Downconversion for Photovoltaics

In principle, the employment of spectral converter is a promising way to increase the efficiency limit imposed by Shockley-Queisser. Ideally, an enhanced PV device harvesting the spectral conversion properties of both DC and upconversion (UC) would consist in a bifacial silicon solar cell with a downconverter layer placed over the top side and an upconverter layer placed between the bottom side of the cell and a reflecting layer, as shown in Fig. 1.5.

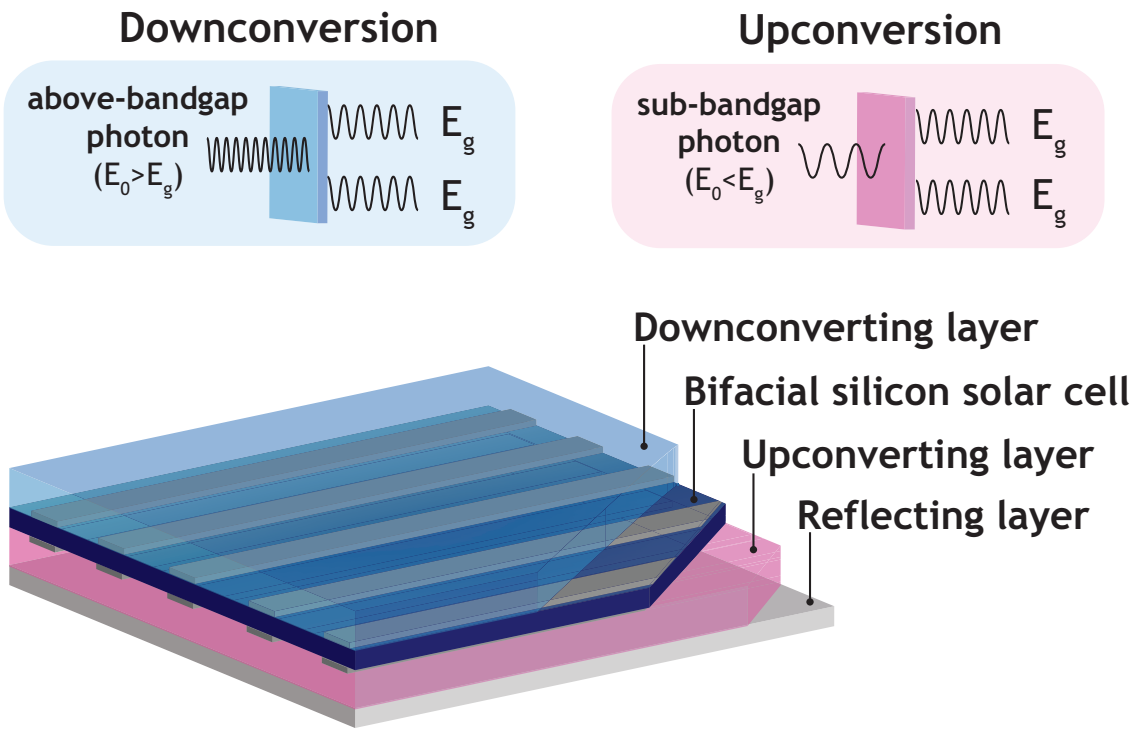

Figure 1.5: Ideal design of a spectral conversion enhanced PV device.

The main feature of an enhanced PV device is that the downconverter and upconverter layers are optically active but electrically passive, meaning that they can increase the output current of the device keeping constant the output voltage. This represents an advantage comparing, for example, to conventional serial connected multijunctions solar cells, which are limited by current matching restrictions [20].

The disadvantages of such a technology are instead represented by the low efficiencies of the downconverter and upconverter materials. Theoretically, their iPLQY, defined as the number of downconverted/upconverted photons for absorbed photons, could achieve more than 100% for DC and up to 50% for UC. In practice, those values are difficult to achieve due to additional optical losses degrading the luminescent properties of those materials. How to overcome those limitations is the aim of this thesis.

1.6 Thesis Overview

The thesis investigates the potential benefits of rare-earth-doped downconverter and upconverter materials in the framework of increasing the efficiency of silicon-based PV devices.

Chapter 2 presents a brief history of solar energy research followed by the description of the operating principles of solar cells and the derivation of the Shockley-Quiesser efficiency limit. The theory of Rare Earths luminescent materials is also introduced, with a particular focus on two main properties: DC and UC of light. The description of an ideal PV device enhanced by the use of downconverter and upconverter luminescent layers is presented.

Chapter 3 describes the materials and methods common to most of the experiments presented in this thesis. It contains the description of the synthesis technique used to grow the materials investigated and the different optical set-ups used to perform spectroscopy measurements to characterise the downconverter and upconverter materials.

Chapter 4 reviews the current state of the art of DC studies for PV applications. It also reports about the luminescent properties of a specific downconverting borate glass co-doped with cerium and ytterbium. Following the discussion of the results, an analytical model describing the self-absorption loss mechanism is proposed and experimentally validated via the analysis of photoluminescence emission spectra measured for different sample's thicknesses.

Chapter 5 discusses the impact of self-absorption on absolute photoluminescence quantum yield analysis and on DC and UC enhanced PV devices. Specifically, this chapter shows how the self-absorption loss mechanism depends strongly on the experimental conditions used to measure the photoluminescence properties. Finally, it examines the combined effect of the exponential absorption of incident light and the non-linear power dependence of the UC process.

Chapter 6 presents a review of upconverter materials used for PV applications and reports the promising results showed by an erbium doped barium yttrium fluoride upconverter crystals achieved by reducing the self-absorption loss mechanism discussed in the previous chapters.

Chapter 7 draws the conclusions on the basis of the results obtained in this work and suggests further work in the area of spectral conversion in order to achieve highly efficient PV solar cells.

Chapter 2

Photonic Materials for Photovoltaics Applications

This chapter begins with a brief history of solar energy research, from the earliest studies to the recent developments, which introduce the three generations of solar cell technologies. The theoretical background on the fundamental physics of solar cells is provided in order to understand the operation and the dominant mechanisms which leads to the Shockley-Queisser efficiency limit of a PV device. The discussion is followed by presenting the theory of rare earth doped luminescent materials, which is necessary to comprehend the mechanisms causing the spectral conversion properties, with particular focus on the DC and UC processes. Finally, we will show how we can combine the luminescent properties of rare earth with an established solar cell technology in order to design a PV device overcoming the Shockley-Queisser limit.

2.1 Solar Energy Research

2.1.1 Historical Background

A legend says that around 212 BC the Greek city of Syracuse, under siege by Romans, used a solar powered defensive weapon developed by the famous inventor and mathematician Archimedes. Supposedly, the Syracusans were able to concentrate the sunlight with a collection of mirrors on the upcoming Romans ships and set them on fire (see Fig. 2.1). Despite the veracity of its actual realisation, this legend told us that more than 2000 years ago it was already present the idea of harvesting the energy provided by the Sun.

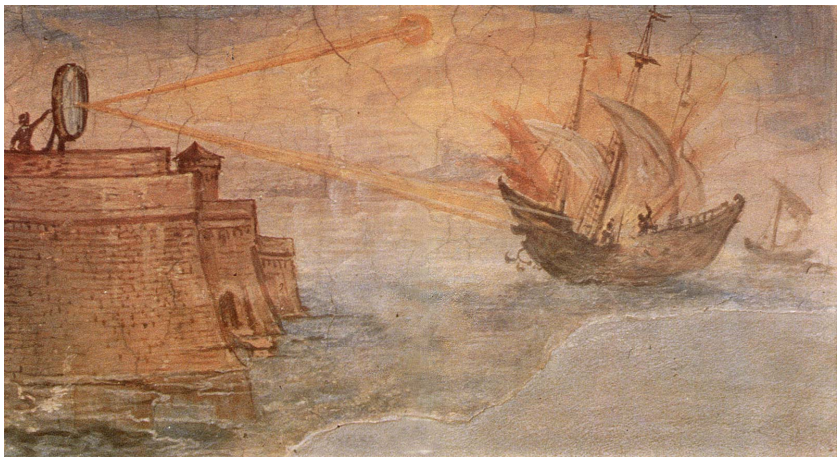

Figure 2.1: Wall painting from the Uffizi Gallery, Stanzino delle Matematiche, in Florence, Italy, showing the Archimedes' mirror used to burn a Roman military ship. Painted by Giulio Parigi in 1600.

Generating heat from the Sun is quite a familiar concept because it is closely linked to the warming feeling we could experience on a sunny day, whereas it is less obvious how to generate electricity from sunlight.

A crucial experiment performed by the French physicist Edmond Becquerel in 1839 showed for the first time that it was possible to produce electric current from light. In the experiment he created an electrolytic cell from two platinum electrodes coated with silver chloride in an acidic solution [21]. Eventually, he noticed that exposing the cell to the sunlight resulted in an increased current generated by the

electrolytic cell.

In 1876, Adams and Day observed the effect of light in selenium [22]. The cell consisted of a thin layer of gold on top of selenium and it had an energy conversion efficiency less than 1%. This prototype led to the first solar cell device made by Charles Fritts [23] in 1883.

At the beginning of the twentieth century two crucial breakthroughs were achieved: the first due to Albert Einstein, who, in 1905 explained the theory of the *photoelectric effect* [24], experimentally demonstrated by Robert Millikan in 1916 [25]. The second, due to Jan Czochralski, who, in 1918, developed a method to grow silicon single crystals.

Einstein's theory was necessary to understand the underlying physics of the photovoltaic effect, while the invention of the crystal growing technique, called *Czochralski process*, made it possible to grow bulk single crystals of silicon. This technique is nowadays the most widely used industrial method for the production of silicon solar cells. It was in fact with the advent of silicon that PV devices began to show their real potential.

In 1954, *Bell Laboratories* produced the first p-n junction silicon solar cell, and successively, in 1954, developed the first solar battery having an efficiency of about 6% [26] (see Fig. 2.2). Despite the low energy conversion efficiency and short operation lifetime, this cell can be recognised as the closest device to the modern solar cells based on single junction semiconductors.

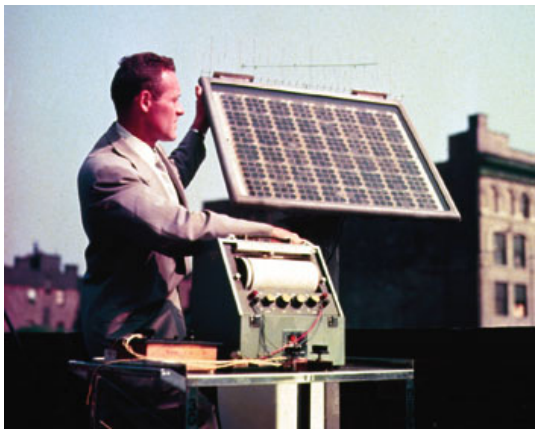

Figure 2.2: Bell solar battery installed by an engineer in 1954. Image adapted from [27].

Since then much effort has been made to increase the efficiency of silicon solar cells, with particular regards to spacecraft applications, but it is only in the last few decades that PV research has been focused in the energy production for terrestrial applications.

Today, solar cells are used in everyday life, from calculators to rooftop solar panels. Thanks to improved designs and new materials development, solar cell efficiencies have reached values over 40% (see Fig. 2.3). PV research continues with the goal of bringing the cost down while raising the efficiency to make solar power a valid alternative energy resource. From the first solar cell developed by Bell Laboratories to our present, different approaches and technologies have been developed. Those can be classified into three generations.

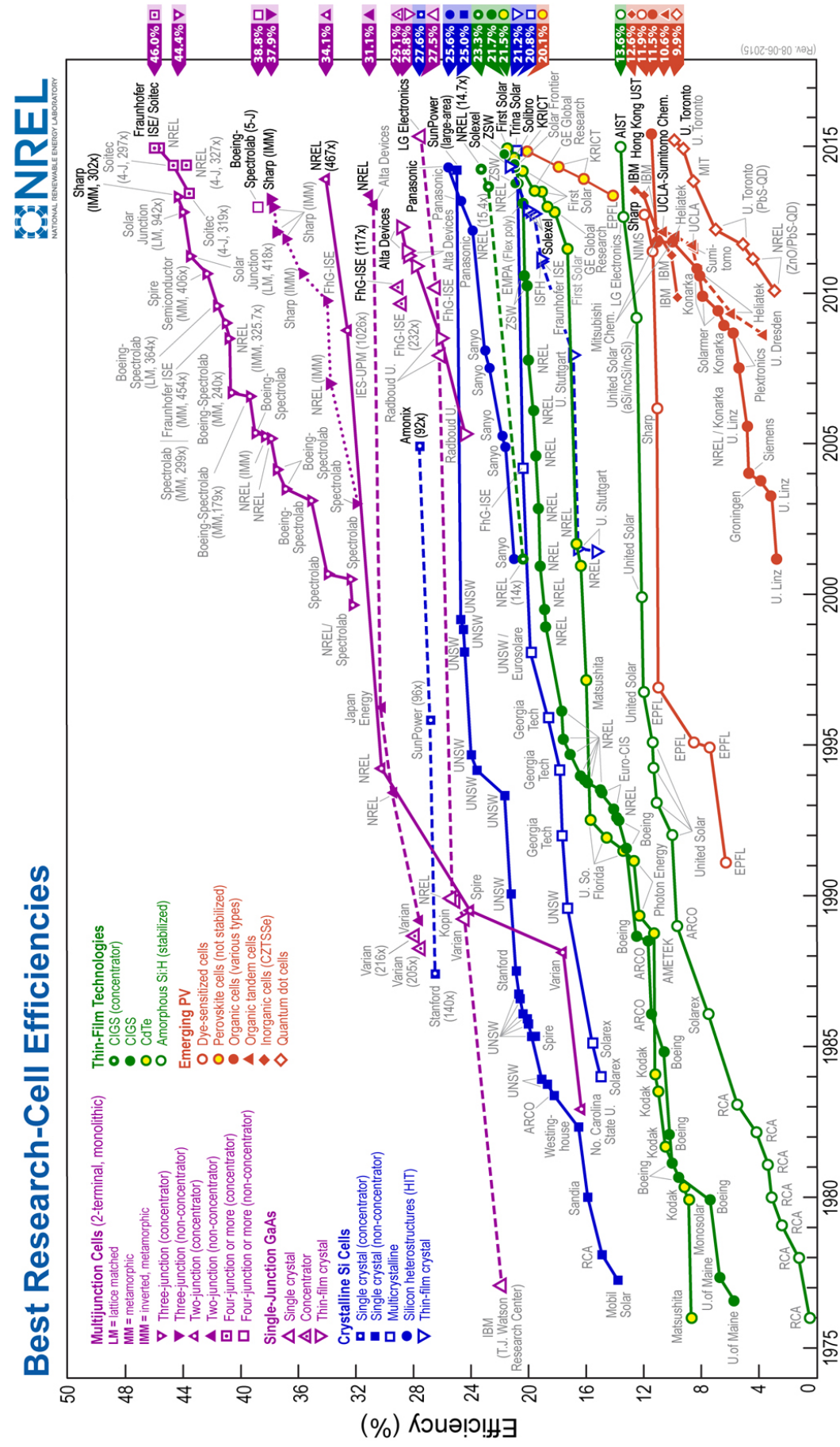

Figure 2.3: Solar cell efficiencies chart. Image taken from [28].

2.1.2 First Generation Solar Cells

First generation solar cells includes single p-n junction solar cells made of c-Si or multicrystalline silicon (mc-Si). They are the most reliable in terms of stability and efficiency, and to date they retain the dominant share of the PV market (∼90%) [8,10]. c-Si based solar cells demonstrated a energy conversion efficiency of 25.0% for non-concentrated sunlight, and 27.6% for concentrated sunlight (concentration factor of 92x). Solar cell technology based on mc-Si achieved energy efficiency conversion of 20.8% (under non-concetrated sunlight), but they have the advantage of a lower cost production [29]. A chronological evolution of first generation solar cell design is represented in Fig. 2.4.

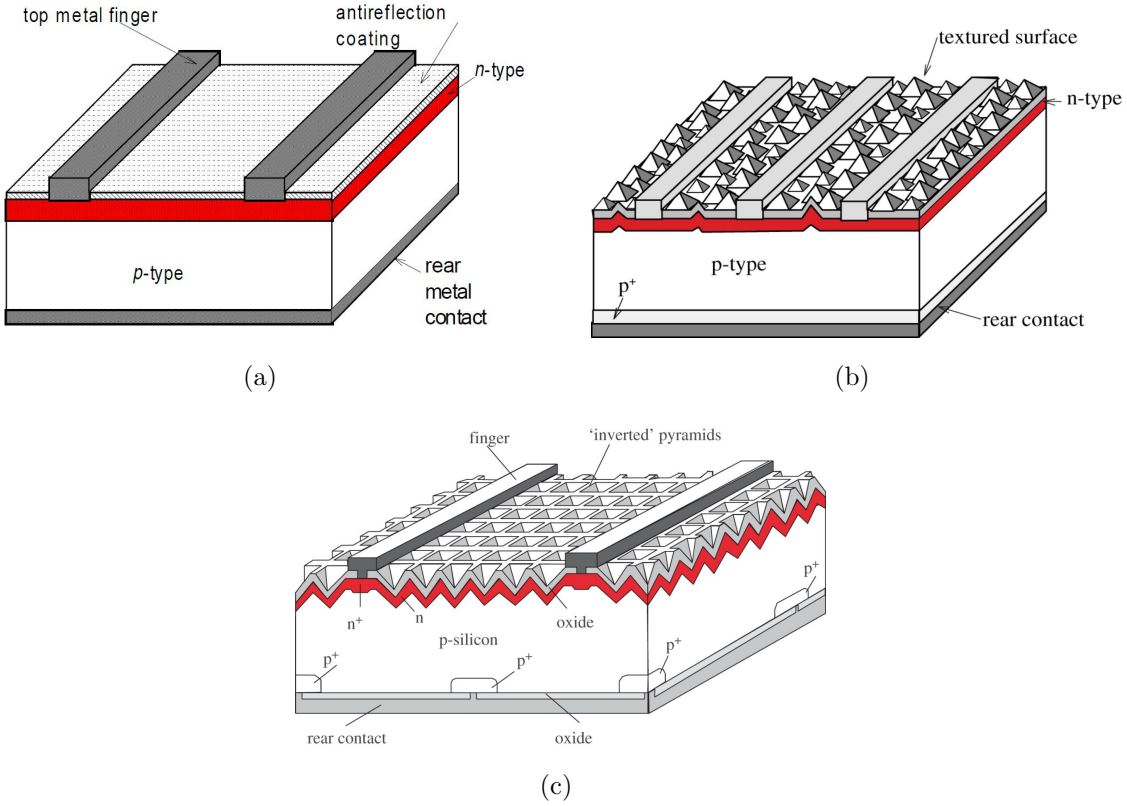

Figure 2.4: Design evolution of first generation solar cells.a) Space silicon cell design developed in the early 1960s. b) The "Black" cell (1974). c) The passivated emitter, rear locally diffused (PERL) cell developed in the 1990s. All images adapted from [30].

The space silicon cell of Fig. 2.4a was developed in the early 1960s. For over a decade it was the standard design of a solar cell. The device was composed of a p-n

junction with two metallic contacts placed on top (fingers) and at the bottom of the cell. The improvement in the design led to the creation of the "Black cell" in 1974 (Fig. 2.4b), and later, in the 1990s, to the passivated emitter rear locally diffused cell (PERL cell) developed by UNSW (Fig. 2.4c), which took the energy conversion efficiency above 24%.

First generation solar cell represents the most widely installed technology in the PV market, and this is due to the well-established silicon manufacturing industry dominated by the integrated circuit industry. The limitations of first generation solar cells lie on two main factors. Firstly, the use of a single junction which inevitably introduces a constraint on the energy which can be harvested (leading to the Shockley-Queisser limit). Secondly, the high production cost of the technology, which reduces the economic competitiveness versus fossil fuels.

2.1.3 Second Generation Solar Cells

The PV market demand for cost reduction has pushed the research towards thin film technology. Thin film solar cells have the advantage of lowering the manufacturing cost and provide features like lightness and flexibility, which make them attractive for either terrestrial or space applications. Nevertheless, they are made of materials which have a lower efficiency compared to first generation solar cells.

Thin film technology includes solar cells based on copper indium gallium selenide (CIGS), cadmium telluride (CdTe), amorphous silicon (a-Si) and microcrystalline silicon (μc-Si) (Fig. 2.5).

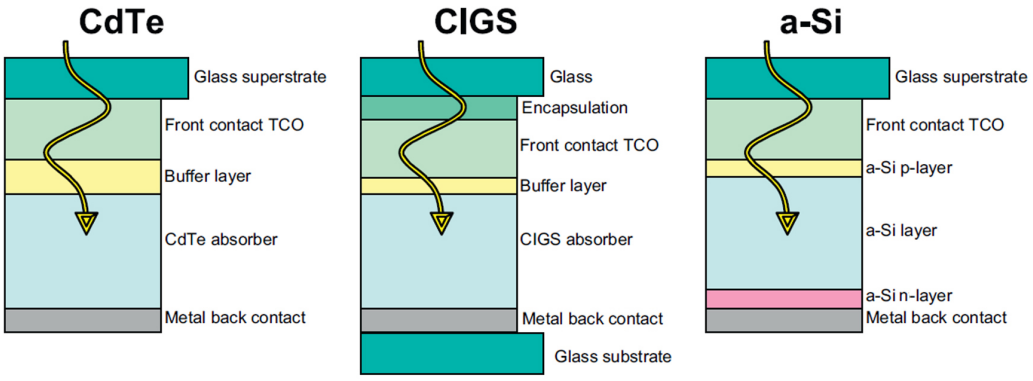

Figure 2.5: Schematic illustration of three different second generation thin film PV devices. In all three devices, cadmium telluride (CdTe, copper indium gallium selenide (CIGS) and amorphous silicon (a-Si), the layers are deposited onto a glass superstrate that allows sunlight to enter through the top layer, the transparent conducting oxide (TCO). The electrical current and voltage are produced in the lower layers. Image taken from [31].

Those materials absorb the sunlight much more efficiently than c-Si or mc-Si allowing the thickness of the active material to be in the range of 1-10 μm. This represents a considerable saving in terms of used material comparing to a typical thickness of 160-240 μm of first generation solar cells [32].

The potential of thin film technologies, especially of CIGS and CdTe, is supported by the record efficiencies values recently achieved. CIGS technology reached 21.7% efficiency, similar to the 21.5% achieved by CdTe technology, while the highest efficiency reported for a-Si thin film solar cells is 13.6% (please refer to Figure 2.3 for dates and historical record efficiencies).

In spite of that, PV based on either CIGS or CdTe has been slow to scale up, due to pending problems related to poor material reproducibility and uniformity over large areas [33]. Another fundamental issue for both CIGS and CdTe technologies is the historical absence of symbiosis with a highly profitable integrated circuit industry [31].

2.1.4 Third Generation Solar Cells

Third generation PV covers a wide range of technologies. Those include new strategies which aim to increase solar cell efficiencies over the Shockley-Queisser limit, together with the development of novel inexpensive materials easy to process on a large scale.

We can divide this category into two subcategories, namely inorganic and organic. Inorganic third generation technologies have been extensively reviewed in literature [18, 19, 34] and include:

- ***Multijunction cells*** Different sub-cells are stacked on top of one another, with each sub-cell converting a specific part of the solar spectrum. Multijunction solar cells have been used in space applications for over 20 years, and are more efficient in comparison to conventional solar cells, but also more expensive to produce due to lattice mismatch and current matching problems [20]. A typical design of a multijunction solar cell is shown in Fig. 2.6.

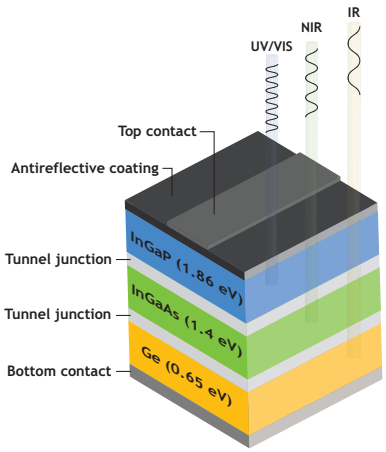

Figure 2.6: Schematic of a typical multijunction solar cell. The cell is composed by three sub-cells having different energy bandgap, each one converting different regions of the solar spectrum.

- ***Multiple carrier excitation*** This phenomenon, also called multiple excition generation, requires the use of semiconductor quantum dots or nanocrystals. In those systems the excitation of a charge carrier due to single photon absorption could generate additional carriers via impact ionisation. The rate of

impact ionisation could be quite efficient because of the carrier confinement in a quantum-confined semiconductor. Generating multiple carriers from a single photon would improve the performances of a solar cell especially at shorter wavelength reducing thermalisation losses. Multiple excitons generation was first demonstrated in 2004 using colloidal PbSe quantum dots [35].

- ***Intermediate-band cells*** This strategy consists in the introduction of an impurity level in the semiconductor bandgap, partially filled with electrons. Photons with insufficient energy to pump electrons from the valence band to the conduction band can use this intermediate band as a stepping stone to generate an electron-hole pair. The intermediate-band solar cell would then reduce transmission losses and it is designed to provide a large photogenerated current while maintaining a high output voltage [36].

- ***Hot carrier*** The concept underlying a hot carrier solar cell is to slow the rate of photoexcited carrier cooling, caused by phonon interaction in the lattice, to allow time for the carriers to be collected whilst they are still at elevated energies (from here the term "hot electrons"), and thus allowing higher voltages to be achieved from the cell [37].

- ***Thermal approaches*** Thermal approaches include thermophotovoltaics, in which a narrow bandgap cell is illuminated by the black body radiation of a hot source at lower temperature than the Sun. Efficiencies can be boosted by use of a selective emitter that only allows light just above its bandgap to be incident on the cell, the rest being reflected back to reheat the primary emitter [38].

- ***Spectral conversion*** This approach aims to modify the solar spectrum before being absorbed by the solar cell such that the photon distribution is concentrated to wavelengths where the solar cell performs at its best. The spectral conversion is a property possessed by rare earth materials, which has already been used for years in the field of laser development or detection systems.

Organic solar cell are another research area showing a huge improvement in the last decade. Their low-cost capacity and recent prototypes showing the ability to overcome 10% efficiency make them an attractive research topic. Their actual disadvantage is mostly on the stability of the organic materials which lower drastically their lifetime comparing to inorganic technologies [39].

The given picture of the actual PV research can be summarised by the "Best Research-Cell Efficiencies Chart" (Fig. 2.3) regularly updated by the National Renewable Energy Laboratory (NREL).

As can be seen from Fig. 2.3, among third generation PV, multijunction solar cells are the more promising technology reaching the highest efficiencies. However, as previously stated, this is a costly technology which could not, at the moment, be employed for large scale PV.

Moreover, most of the highest efficiencies are achieved by using a concentrating system, which requires less PV material but at the same time a tracking system has to be employed to follow the change of Sun position during the day, as well as an heat-dissipation systems which require additional economical efforts.

Despite the economical factors, the development of new PV devices which can surpass the actual energy conversion efficiencies is driven by the possibility of overcoming the limiting factors of current technologies. To identify those limiting factors, and to emerge with new strategies we need to comprehend much more in detail how a solar cell works. This is the aim of the next Section.

2.2 Fundamentals of Photovoltaic Solar Cells

In order to understand the physics behind the solar energy production it is easier to consider separately the properties of the two main elements: the Sun, i.e. the source of energy, and the solar cell, which absorbs and convert photons into electricity.

The Sun has a broad emission spectrum, which includes photons with energies

from ultraviolet (UV) to infrared (IR), while a solar cell is characterised by a wavelength dependent photoresponse spectrum. As introduced in Chapter 1, most of the factors which limit the energy conversion efficiency of a PV cell originate from the mismatch of the two spectra.

2.2.1 Solar Spectrum

The solar radiation reaching our planet, before interacting with the atmosphere, can be roughly approximated with the Plank's distribution of a black body radiator with a temperature of about 5800 K. The expression for the spectral radiance $S_\lambda(\lambda, T)$ of a black body at temperature T is defined by Planck's law:

$$S_\lambda(\lambda, T) = \frac{8\pi hc}{\lambda^5} \frac{1}{e^{\frac{hc}{\lambda kT}} - 1} \tag{2.1}$$

where h is the Planck's constant, λ the photon wavelength, c the velocity of light and k the Boltzmann constant. The resulting emission spectrum, as shown in Fig. 2.7, covers a broad range of wavelengths from UV to IR with the highest peak in the visible (VIS).

The solar spectrum at sea level is modified by the interaction with the atmosphere, causing absorption by contents like water vapour (H_2O), carbon dioxide (CO_2), oxygen (O_2), ozone (O_3), and also scattering by molecules and aerosol particles present in the air. Moreover, the overall intensity of the total irradiance changes along with the optical density of the atmosphere, whose value depends on the illumination conditions.

To take into account different illumination conditions, the zenith angle z, which is the angle between the normal to the Earth's surface and the direction to the Sun, is introduced to define the so called air mass (AM) coefficient:

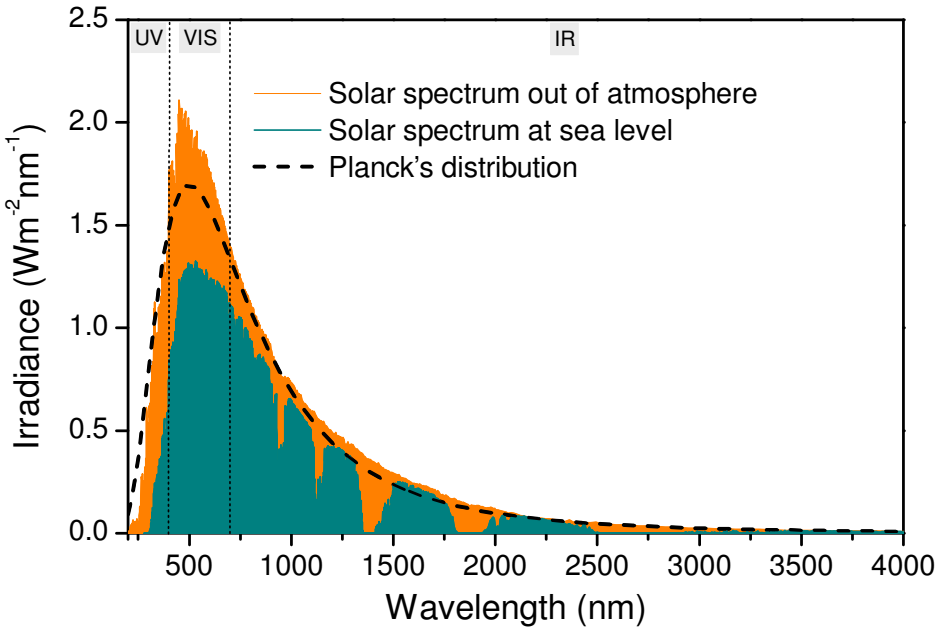

Figure 2.7: Comparison of solar spectrum outside Earth's atmosphere (orange), at sea level (blue), and the spectral radiance $S_\lambda(\lambda, T)$ of a black body at temperature 5800 K (dotted black line).

$$AM \approx \frac{L}{L_0} = \frac{1}{\cos z} \tag{2.2}$$

The AM coefficient is defined as the ratio between the atmosphere thickness L_0 and the effective path length L through the atmosphere of a sun ray incident with an zenith angle different from zero. The approximation is due to the fact that there are other factors which contribute to longer path lengths like the inhomogeneity of the components. Other definitions exist in literature that provide a more accurate way to calculate the AM coefficient. The chosen definition, is the simplest and can be used with a good approximation for $z < 75°$.

Figure 2.8 represents the commonly used solar spectra standards in PV, which are known as AM0, AM1, AM1.5 and AM2. The AM0 corresponds to the solar spectrum outside of earth's atmosphere. The spectra AM1, AM1.5 and AM2 refer to solar spectra at sea level, and accordingly to Eq. 2.2, they correspond to zenith angle of z=0, 48.2°, 60° respectively. The AM1.5 solar spectrum is particularly relevant for US and European countries because it corresponds to the average illumination

conditions at those latitudes.

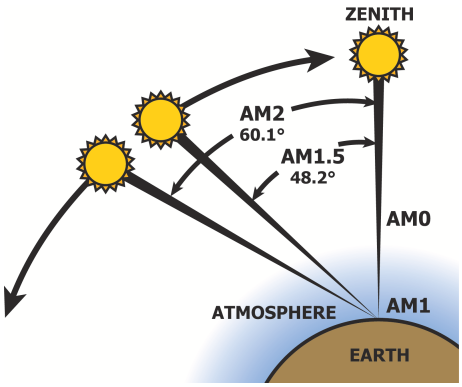

Figure 2.8: Air mass coefficient dependence on zenith angle. The AM1.5 solar spectrum, corresponding to a Zenith angle of 48.2°, represents the average illumination for US and European latitudes.

The need to define a standard for solar illumination is important to compare efficiencies of different solar cells, as factors like spectral distribution and orientation angles might change considerably the performance of a PV device.

For this reason power conversion efficiencies are measured under standard test conditions (STC) unless stated otherwise. The STC correspond to an operating temperature of 25 °C under an AM1.5 solar spectrum, whose total irradiance is 1000 Wm^{-2}.

2.2.2 Photon Electron Conversion

The conversion from solar energy to electricity is based on the photoelectric effect, in which light striking a metallic surface causes the emission of electrons. The energy required to eject the electrons from an atom is called *ionisation energy*, and this is typically higher than 5 eV. The Sun provides photons with energy up to 4.5 eV, which is less than typical ionisation energies, for this reason semiconductor materials are employed due to the existence of two electronic states, the bound state (valence band) and the unbound state (conduction band) separated by an energy bandgap E_g, whose value can cover order of magnitude of 10^{-1} - 10 eV.

The photoelectric effect, in the case of a semiconductor material, allows the

absorbed photon to promote an electron from the valence band to the conduction band, providing the photon energy is equal to or higher than E_g. Therefore the excited electron does not escape outside the material, and can freely move within the conduction band. At the same time a lack of electron, a hole, is propagating in the valence band. The negatively charged electron and positively charged hole tends to recombine after a certain amount of time to restore the equilibrium.

The recombination process needs to be inhibited in order to utilise the photo-generated carriers for current production. To do so a junction made of same semiconductor material doped with an excess of electrons (n-type) and with an excess of holes (p-type) is created. Silicon for example, which is a member of the group IV semiconductors, can be doped with a group V or a group III element to create a n-type or a p-type semiconductor substrate, respectively. Commonly, n-type semiconductor is obtained via doping silicon with phosphorus, while for p-type the used dopant is boron.

When a p-n junction is formed some of the electrons in the n-type region diffuse to the p-type region and vice versa. The consequent recombination between the diffused free carriers produces a charge distribution at the interface in which an electric field is established, known as *depletion region*. The electric field, or equivalently the potential barrier in the depletion region, avoid additional electrons diffusing to the p-region or additional holes diffusing to the n-region.

If a potential difference is applied externally across the junction the potential barrier at the depletion region is reduced or increased depending on the voltage polarity, leading to the forward bias or reverse bias case. In presence of forward biasing the depletion region is reduced and current can flow across it, while in case of reverse biasing the depletion region is enhanced and the current flow is avoided. This is the common use of a p-n junction acting as a diode.

In a solar cell instead no voltage is applied externally. Light incident on the top of the solar cell is absorbed through the cell by silicon atoms generating electron-holes.

The electron-hole pairs generated in the n-type or p-type regions tend to rapidly recombine while pairs generated in the depletion region feel the electric field which separates them creating a flow of electrons towards the n-type region and of holes towards the p-type region. The flowing carriers are finally collected by the electrodes placed on the top and on the bottom generating the usable electric current.

2.2.3 Equivalent Circuit of a Photovoltaic Solar Cell

The laws describing the operation of a solar cell can be deduced from the principles of electric circuits. A generalised model describing the PV solar cell operation can be developed by using the equivalent circuit schematised in Fig. 2.9.

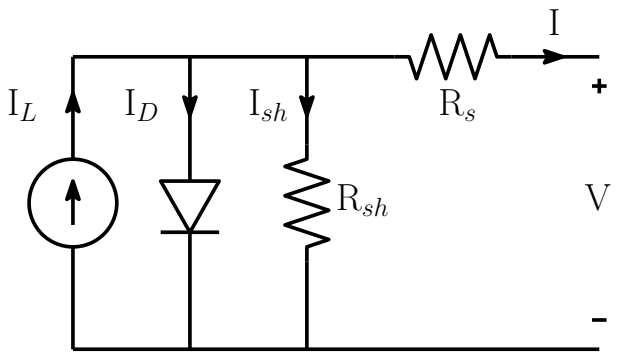

Figure 2.9: Equivalent circuit of a PV solar cell. A current generator represents the photogenerated carriers converted from sunligth that are flowing through an ideal diode (p-n junction). The equivalent circuit also includes a series resistance (R_s) and shunt resistance (R_{sh}) representing the internal losses of the solar cell.

The circuit is composed of a direct current source I_L, representing the electrons-holes generated by sunlight absorption, connected in parallel to an ideal diode (representing the p-n junction) in which flows a current I_D and two dissipative elements, a series resistance (R_s) and a shunt resistance (R_{sh}), which relate to losses occurring in a real device. We call I_{sh} the current flowing through the shunt resistance, while the current flowing through the series resistance is the output current I.

The losses connected to R_s include current drop through the emitter and base of the solar cell, contact resistance between the metal contacts and the silicon, and the resistance of the top and rear metal contacts. Instead, R_{sh} represents losses due

to presence of defects in the device causing primarily a drop in voltage output.

To solve the equivalent circuit of Fig. 2.9 we first consider the current flow in the ideal diode I_D. This is given by the *Shockley equation*:

$$I_D = I_0(e^{\frac{q(V+IR_s)}{kT}} - 1), \tag{2.3}$$

where I is the current delivered by the cell, q the electron charge, k the Boltzmann constant, T the operating temperature of the cell, I_0 the diode saturation current and V the potential difference at the terminals of the circuit.

Always referring to the equivalent circuit, it is possible to relate the different currents in each closed loop using Kirchhoff's circuit law. It results that

$$I = I_L - I_D - I_{sh}. \tag{2.4}$$

Finally, combining Eq. 2.3 and Eq. 2.4, and knowing that $I_{sh} = \frac{V+IR_s}{R_{sh}}$, the implicit form of the current delivered by the solar cell can be derived:

$$I = I_L - I_0(e^{\frac{q(V+IR_s)}{kT}} - 1) - \frac{V + IR_s}{R_{sh}}. \tag{2.5}$$

The analytical solution for the output current defined implicitly in Eq.2.5 depends on the values of R_{sh} and R_s, which are never known unless the solar cell is tested experimentally. The equation can also be numerically solved so to obtain a solution for the current in the explicit form $I(V)$.

The resulting current-voltage curve is closely related to the diode characteristic curve, with a negative offset introduced by the injected photogenerated electrons (I_L) while the cell is illuminated (see Fig. 2.10).

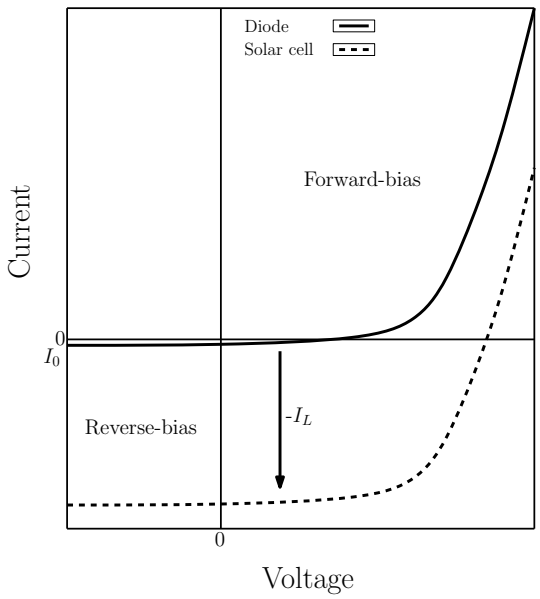

Figure 2.10: V-I curve comparison between an ideal diode (solid line) and an illuminated solar cell (dotted line). The vertical shift is due to the presence of the current I_L connected to the photogenerated electron-hole pairs.

As the solar cell is used as a battery, and hence representing a voltage source, the corresponding graph in the IV quadrant of Fig. 2.10 is flipped on the x-axis. The resulting characteristic V-I curve is shown in Fig. 2.11.

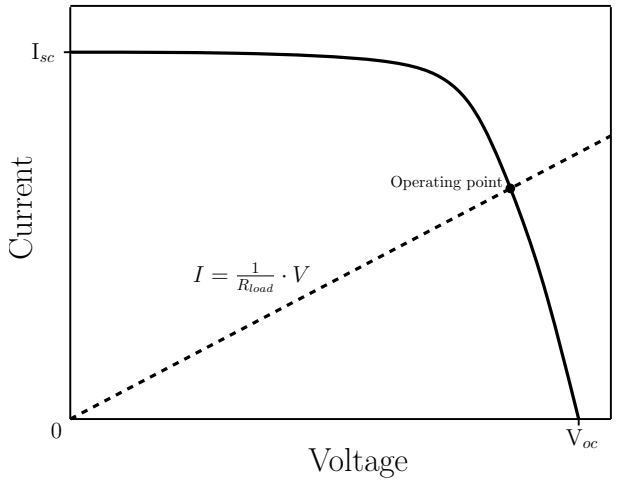

Figure 2.11: V-I curve characteristic of a PV solar cell intersecting the linear V-I curve of a load resistance ($\mathrm{R_{load}}$), whose slope is proportional to $\frac{1}{R_{\mathrm{load}}}$. The intersection between the two curves is called the solar cell's operating point.

The two main points that can be extrapolated from a V-I curve are the short circuit current (I_{sc}), and the open circuit voltage (V_{oc}). They correspond to the current at $V = 0$ (short-circuit configuration) and to the voltage at $I = 0$ (open-

circuit configuration), respectively.

The V-I curve characteristic of a solar cell can be obtained experimentally and it represents the way of calculating many important parameters like the power conversion efficiency. The experimental determination of the V-I curve is done illuminating the cell using the STC parameters and connecting it to a variable load (R_{load}). As shown in Fig. 2.11, the operating point, i.e. the point at which the cell is operating while connected to R_{load}, results from the intersection between the load line, defined by $I = \frac{V}{R_{\text{load}}}$ and the V-I characteristic curve of the solar cell.

2.2.4 Power Conversion Efficiency

The output power P_{out} can be obtained multiplying the output voltage V by the output current I:

$$P_{out} = V \cdot I \tag{2.6}$$

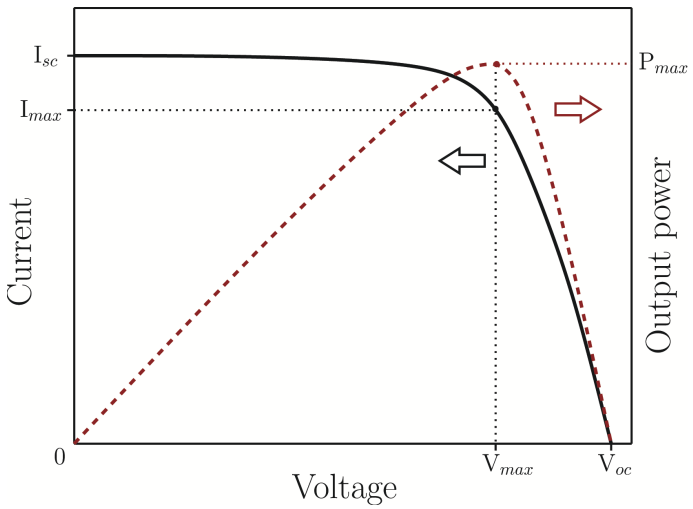

Figure 2.12: Output current (dashed red) and output power (black solid) of a solar cell. The current and voltage values I_{max} and V_{max} corresponding to the maximum output power P_{max} have been highlighted.

Fig. 2.12 shows that the output power has a maximum value (P_{max}) corresponding to specific current and voltage values indicated as V_{max} and I_{max}. Those values

are associated with an optimal load for which the solar cell power output is maximised. P_{max} divided the incoming power P_{in}, calculated from the solar irradiance by the cell surface, gives the maximum power efficiency, η_{max}, of the cell:

$$\eta_{max} = \frac{P_{max}}{P_{in}} = \frac{I_{max}V_{max}}{P_{in}} \tag{2.7}$$

Another useful parameter is the fill factor (FF) defined by:

$$FF = \frac{I_{max}V_{max}}{I_{sc}V_{oc}} \tag{2.8}$$

This is equivalent to the ratio between P_{max} and the maximum theoretically achievable by an ideal cell. The FF is a measure of the quality of the cell. High values of R_s, or low values of R_{sh} will decrease the FF value. An ideal cell has a FF equal to 1.

2.2.5 The Shockley-Queisser Detailed Balance Limit

In the previous subsection we showed that the two more important parameters are the short circuit current I_{sc}, or equivalently the short-circuit current density J_{sc} (I_{sc} divided by the illuminated area of the cell) and the open circuit voltage V_{oc}. In a single junction solar cell those values depend essentially from the energy bandgap E_g because it controls the amount of sunlight photons that can be absorbed by the cell (proportional to J_{sc}), and at the same time determines the energy at which the electron are collected (proportional to V_{oc}).

Low values of E_g will increase the amount of J_{sc} and decrease the V_{oc}, while the opposite will happen increasing E_g. Therefore, because the efficiency conversion is proportional to the product $J_{sc}V_{oc}$, it is expected that there exists an optimal bandgap with maximum electric power output.

In 1961, a theoretical study performed by Shockley and Queisser [13] investigated the problem of finding the highest power conversion efficiency that a single junction solar cell can achieve as a function of the energy bandgap E_g.

Their calculation found that the efficiency of an ideal solar cell based on single junction semiconductor technology is limited to about 33%. Here we present the derivation of this limit in order to understand in a quantitative way where the limitations come from and also why silicon technology is so far the most commercialised.

The Shockley-Queisser's model is based on the detailed balance principle, in which every elementary process considered is balanced by its reverse process. We here follow the logic and derivation presented in [40].

In Shockley-Queisser's work the following assumptions were made:

(i) The probability of an absorbed photon to produce a electron-hole pair is zero if the photon energy $E_{ph} < E_g$, while its equal to one if $E_{ph} \geq E_g$.

(ii) All photogenerated charge carriers thermalise at the conduction band edge.

(iii) The probability to collect the photogenerated carries in short circuit mode is equal to one.

(iv) The only loss mechanism additional to the non absorption of sub-bandgap photons, and thermalisation losses is the spontaneous emission due to the electron-hole pairs recombination.

Due to assumption (iii), the maximum available short-circuit current density $J_{sc,SQ}$ is directly proportional to the number of solar photons absorbed by the solar cell, integrated over all photon energies:

$$J_{sc,SQ} = q \int_0^\infty A(E)\Phi_{inc}(E)\, dE = q \int_{E_g}^\infty \Phi_{inc}(E)\, dE, \tag{2.9}$$

where q is the electron charge, $A(E)$ the photon absorption spectrum of the solar cell, and $\Phi_{inc}(E)$ the total flux of incident photons. The integration interval has been transformed from [0,∞] to [E$_g$,∞] due to assumption (i), from which it is assumed $A(E)$ equal to zero for $E_{ph} < E_g$ and $A(E)$ equal to 1 for $E_{ph} \geq E_g$.

In this case Φ_{inc} is calculated using the solar spectrum AM1.5, while in their original work Shockley and Queisser used the spectrum of a blackbody at temperature 6000 K. In this way it is possible to plot J_{sc} as a function of the energy bandgap E_g as reported in Fig.2.13

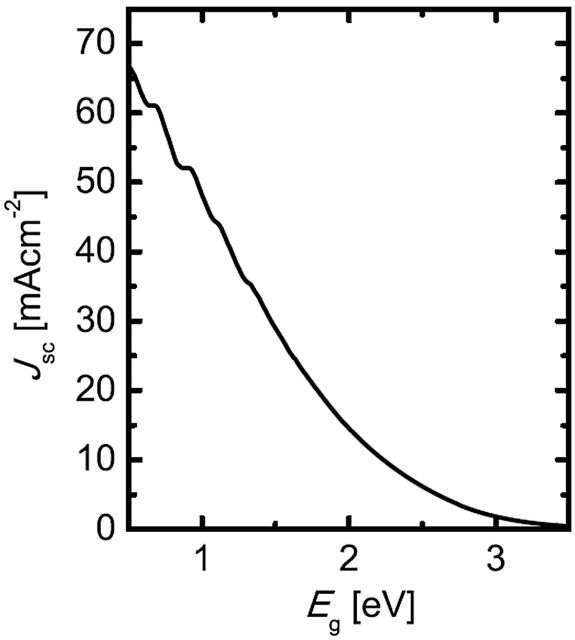

Figure 2.13: Short-circuit current density J_{sc} versus the energy bandgap E_g. Image adapted from [40].

Let us consider the solar cell in the dark being in equilibrium with the surrounding environment at temperature T. According to Kirchoff's law of thermal radiation, the emissivity Φ_{em} of the solar cell due to electron-hole recombination, and the absorption of the outer blackbody radiation $A(E)\Phi_{bb}(E,T)$ has to be equal:

$$\Phi_{em} = A(E)\Phi_{bb}(E,T) \tag{2.10}$$

When a potential difference V is applied to the solar cell, from Wurfel's generalisation of Kirchoff's law [41], we can write the recombination current density $J_{rec,SQ}(V)$ as follows:

$$J_{rec,SQ}(V) = q\int_0^\infty A(E)\Phi_{bb}(E,T)\exp\left(\frac{qV}{kT}\right)\,dE = q\int_{E_g}^\infty \Phi_{bb}(E,T)\exp\left(\frac{qV}{kT}\right)\,dE. \tag{2.11}$$

Again, the second passage follows from assuming $A(E)$ as a step-function with a cut-off value defined by the bandgap E_g. Equation 2.11 represents the current density due only to pair's recombination when the solar cell is not illuminated.

The general expression of $J(V)$ is finally calculated considering both the contribution of $J_{sc,SQ}$ and $J_{rec,SQ}$. It results then:

$$J(V) = J_{rec,SQ}(V) - J_{sc,SQ} = q\int_{E_g}^\infty \Phi_{bb}(E)\,dE\exp\left(\frac{qV}{kT}\right) - q\int_{E_g}^\infty \Phi_{inc}(E)\,dE \tag{2.12}$$

In the general case Φ_{inc} can be written as the sum of the flux of solar photons Φ_{sun} and the one deriving from the environment at temperature T, indicated by Φ_{bb}.

$$\Phi_{inc} = \Phi_{sun} + \Phi_{bb} \tag{2.13}$$

Substituting Eq. 2.13 in Eq. 2.12 we obtain

$$J(V) = q\int_{E_g}^\infty \Phi_{bb}(E)\,dE\left[\exp\left(\frac{qV}{kT}\right) - 1\right] - q\int_{E_g}^\infty \Phi_{sun}(E)\,dE. \tag{2.14}$$

The last expression represents the typical diode equation for current density with the additional contribution of the photogenerated current density. Considering

three different values of $E_g = 0.8$, $E_g = 1.4$, $E_g = 2.0\,eV$ we obtain the J-V curve characteristic represented in Fig. 2.14.

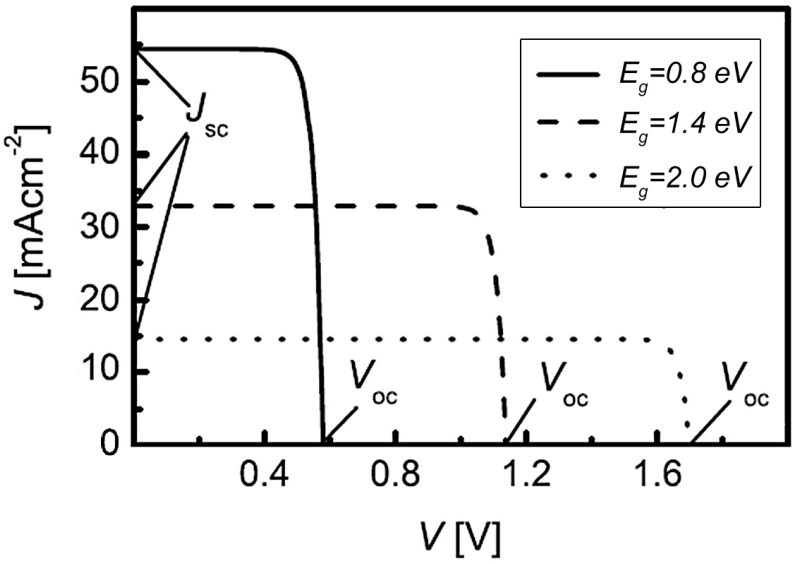

Figure 2.14: J-V curve for different bandgap energies E_g = 0.8 eV (solid line), E_g = 1.4 eV (dashed line) and E_g = 2.0 eV (dotted line). Image adapted from [40].

Evaluating Eq. 2.14 at $J = 0$ we also find the open-circuit voltage V_{oc} resulting:

$$V_{oc} = \frac{kT}{q} \ln \left(\frac{\int_{E_g}^{\infty} \Phi_{sun}(E)\, dE}{\int_{E_g}^{\infty} \Phi_{bb}(E)\, dE} + 1 \right) = \frac{kT}{q} \ln \left(\frac{J_{sc,SQ}}{J_{0,SQ}} + 1 \right) \tag{2.15}$$

$J_{0,SQ}$ indicates the saturation current in the limit of Shockley-Queisser, namely the smallest possible current provided by the bandgap energy of the semiconductor. Finally, we can calculate the output power multiplying V by $J(V)$. Its maximum value divided the incoming power, associated with the solar flux, corresponds to the maximum power conversion efficiency η_{max}:

$$\eta_{max} = \frac{\max |J(V) \cdot V|}{P_{inc}} = \frac{\max |J(V)V|}{\int_{E_g}^{\infty} E\Phi_{sun}(E)\, dE}. \tag{2.16}$$

Figure 2.15 shows both $V_{oc}(E_g)$ and $\eta(E_g)$ dependence with respect to the energy

bandgap E_g. It is found that the efficiency limit has its maximum at around 33% for energy bandgaps in the range of 1.1< E_g <1.4. This value slightly differs from the one of Shockley-Queisser because here it has been considered for the solar spectrum the modern standard AM1.5 instead of a blackbody emission.

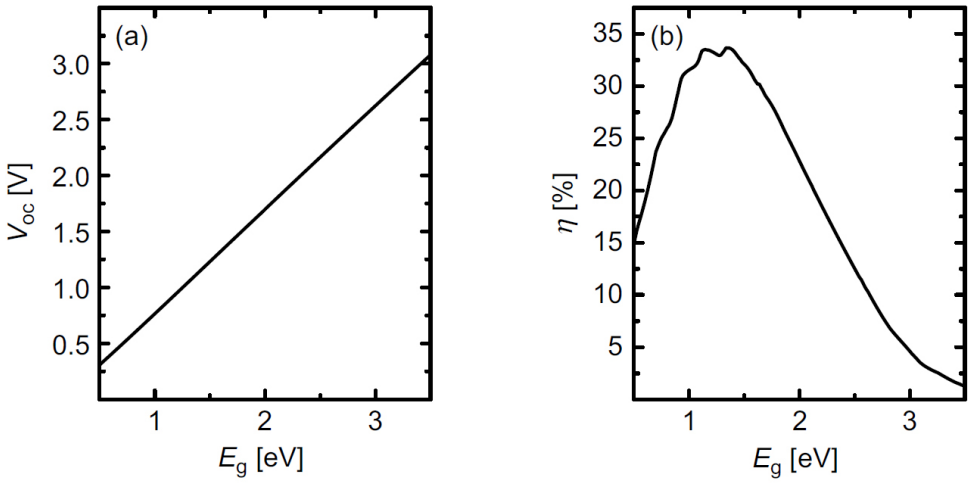

Figure 2.15: (a) Open-circuit voltage V_{oc} and (b) power conversion efficiency η versus energy bandgap E_g. Images adapted from [40].

c-Si, with a bandgap of 1.1 eV, shows its advantage for being employed in single junction solar cells. At the same time 33% efficiency for an ideal device, as modelled in this analysis, represents a significant limitation. Overcoming this limit is the main challenge of current PV research.

2.3 Theory of Rare Earths Doped Luminescent Materials

2.3.1 Overview on Rare Earths Elements

Rare earths is the name given to those elements with an atomic number between 57 and 71. Despite the name, those elements are not rare at all, as their abundance is comparable with commonly used metals like copper, zinc, lead and nickel.

Their electronic configuration is the same of Xenon noble gas ($1s^2$ $2s^2$ $2p^6$ $3s^2$ $3p^6$ $3d^{10}$ $4s^2$ $4p^6$ $4d^{10}$ $5s^2$ $5p^6$) plus two electrons in the 6s shell, one in the 5d shell (not for all elements) and the partially filled 4f shell.

In Table 2.1 the rare earths elements are listed together with their symbol, atomic number Z, the electronic configuration for the atomic state, for the trivalent rare earth (RE^{3+}) ion state (oxidation number +3) and their abundances.

Table 2.1: Rare earths elements. [Xe] is the configuration of xenon: $1s^2\,2s^2\,2p^6\,3s^2\,3p^6\,3d^{10}\,4s^2\,4p^6\,4d^{10}\,5s^2\,5p^6$. [1]Data taken from [42]

Name	Symbol	Z	Electronic configuration		Abundances[1]
			0	+3	(ppm)
Lanthanum	La	57	$[Xe]5d^1\,6s^2$	$[Xe]\,4f^0$	30
Cerium	Ce	58	$[Xe]4f^1\,5d^1\,6s^2$	$[Xe]\,4f^1$	60
Praseodymium	Pr	59	$[Xe]4f^3\,6s^2$	$[Xe]\,4f^2$	8.2
Neodymium	Nd	60	$[Xe]4f^4\,6s^2$	$[Xe]\,4f^3$	28
Promethium	Pm	61	$[Xe]4f^5\,6s^2$	$[Xe]\,4f^2$	-
Samarium	Sm	62	$[Xe]4f^6\,6s^2$	$[Xe]\,4f^4$	6
Europium	Eu	63	$[Xe]4f^7\,6s^2$	$[Xe]\,4f^5$	1.2
Gadolinium	Gd	64	$[Xe]4f^7\,5d^1\,6s^2$	$[Xe]\,4f^6$	5.4
Terbium	Tb	65	$[Xe]4f^9\,6s^2$	$[Xe]\,4f^7$	0.9
Dysprosium	Dy	66	$[Xe]4f^{10}\,6s^2$	$[Xe]\,4f^8$	3
Holmium	Ho	67	$[Xe]4f^{11}\,6s^2$	$[Xe]\,4f^9$	1.2
Erbium	Er	68	$[Xe]4f^{12}\,6s^2$	$[Xe]\,4f^{10}$	2.8
Thulium	Tm	69	$[Xe]4f^{13}\,6s^2$	$[Xe]\,4f^{11}$	0.48
Ytterbium	Yb	70	$[Xe]4f^{14}\,6s^2$	$[Xe]\,4f^{12}$	3
Lutetium	Lu	71	$[Xe]4f^{14}\,5d^1\,6s^2$	$[Xe]\,4f^{13}$	0.5

Doping of glasses or crystals with rare earths elements are commonly used due to their unique luminescent properties. When a rare earth element is incorporated as a dopant in a crystalline matrix it loses two electrons in the 6s shell and one electron in the 5d shell, or in case this is not present, one electron is lost from the 4f shell.

It results under the form of RE^{3+}, having the incomplete 4f shell acting as the valence band, surrounded by the filled 5s and 5p shells (see Fig. 2.16). Some ions may assume a bivalent form, like europium, samarium or ytterbium, or a quadrivalent form, like cerium and terbium.

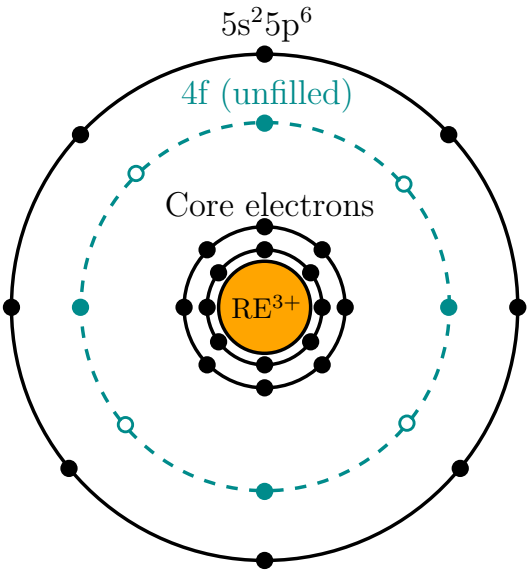

Figure 2.16: Schematic of the electronic configuration of a trivalent rare earth ion. The unfilled 4f valence shell lies between the core electrons and the outer (filled) shell $5s^25p^6$. Each rare earth element is characterised by the different number of electrons populating the 4f shell.

As an example, Fig. 2.17 shows the spatial distribution of the outer shells of a Gd^+ is shown as a result of a Hartree-Fock calculus made by Freeman and Watson [43]. For a RE^{3+} ion the 6s shell is empty and the spatial distribution peaks relating to the 5s and 5p shells would be shifted to longer distances with respect to the 4f shell.

The outer shells surrounding the 4f valence electrons produce a shielding effect, which reduces the strength of external electromagnetic interactions, in particular those of the crystal field which act on the 4f electrons as an external perturbation.

The small entity of the perturbation of the crystal field determines a symmetry breakdown on the system, whose effect is to modify the selection rules regulating the transitions between different quantum states. Specifically, transitions involving electrons belonging to the same shell ($4f \rightarrow$4f), which are generally avoided by the selection rules, are instead possible in this particular case.

The $4f \rightarrow$4f transitions, covering a broad range of spectral region, that goes from vacuum ultraviolet (VUV) to IR, are responsible for the distinctive optical properties of rare earth doped materials. One of the most interesting property is

the ability to act as spectral converter, which is the phenomenon of interest in this thesis.

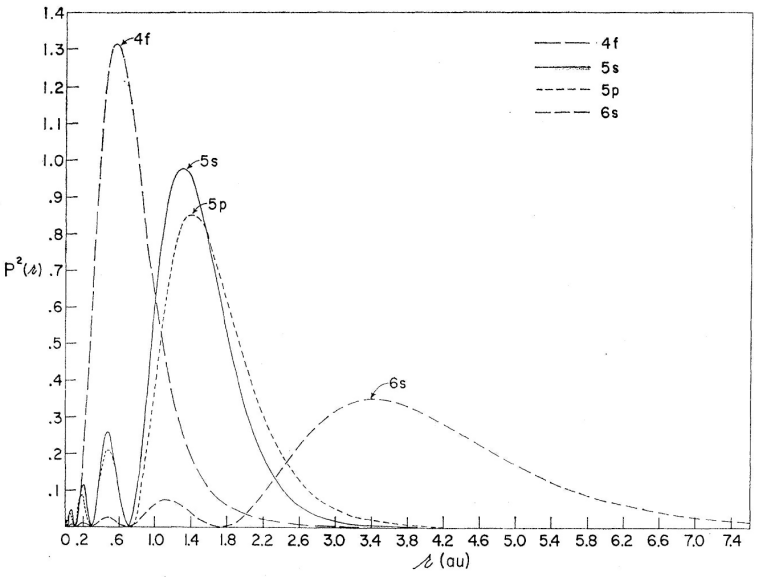

Figure 2.17: Radial distribution function (density vs distance) of 4f, 5s, 5p and 6s shell for a Gd^+ ion. Image taken from [43].

From a spectroscopy point of view, absorption and emission spectra of this class of materials result in well defined narrow lines, and for this reason rare earths are generally referred to have *atomic-like* spectra due to their similarity with those of free atoms or molecules.

2.3.2 Energy Levels of Rare Earth Doped Materials

The theory describing the energy levels of rare earths doped materials, based on quantum calculations, has been developed originally by Judd and Ofelt in their separate works published in 1962 [44, 45].

In this section we are not presenting the full theory, as it is out of the scope of this thesis. Instead, we summarise the fundamentals of the quantum theory explaining the origin of the atomic-like energy levels, and of the energy transfer mechanisms responsible for the spectral conversion properties.

We begin by considering a RE^{3+} ion as an isolated system having no interactions

with the external environment. This the case of the so-called *free-ion model*. The N valence electrons (belonging to the 4f shell) of a free-ion feel each other through the electron-electron coulomb interaction V_{ee} and the electron spin-orbital interaction V_{so}. Moreover, they are attracted by the positive nuclear charge through the nucleus-electron coulomb interaction V_{en}.

The resulting eigenvalue problem, describing the wave function $\Psi(\phi, \chi)$ of the 4f shell is

$$H\Psi(\phi, \chi) = E\Psi(\phi, \chi) \tag{2.17}$$

H is the Hamiltonian describing a system of N electrons and can be written as

$$H = T_e + V_{en} + V_{ee} + V_{so} \tag{2.18}$$

where T_e is the kinetic energy of the N electrons. The explicit form of the Hamiltonian can be written as follow:

$$H = -\frac{\hbar^2}{2m}\sum_{i=1}^{N}\nabla_i^2 - \sum_{i=1}^{N}\frac{Ze^2}{r_i} + \sum_{i<j}^{N}\frac{e^2}{r_{ij}} + \sum_{i=1}^{N}\zeta(r_i)\mathbf{s}_i \cdot \mathbf{l}_i \tag{2.19}$$

where $N = 1, \ldots, 14$ is the corresponding number of valence electron in the 4f shell, e and m are the charge and mass of the electron, r_i is the radial coordinate of the i-th electron, r_{ij} is the distance $|\mathbf{r}_i - \mathbf{r}_j|$ between the i-th and j-th electrons, Z is the nucleus charge, $\mathbf{s}_i$ and $\mathbf{l}_i$ are the spin and angular momentum of the i-th electron, and $\zeta(r_i)$ represents the spin-orbital coupling function defined as:

$$\zeta(r_i) = \frac{\hbar^2}{2m^2c^2r_i}\frac{dU(r_i)}{dr_i} \tag{2.20}$$

with $U(r_i)$ being the potential felt by the i^{th} electron and c is the velocity of

light.

The first two terms of Eq. 2.19 have spherical symmetry, and hence are unable to solve any degeneration. The other two terms, V_{ee} and V_{so}, are instead the one responsible for the level split of the energy levels relative to the 4f electrons. To solve Eq. 2.19 different strategies can be used depending on the particular case of study. Three possibilities can be considered:

- $V_{ee} \gg V_{so}$ (*Russell-Saunders coupling or LS coupling*)
- $V_{ee} \ll V_{so}$ (*j-j coupling*)
- $V_{ee} \sim V_{so}$ (*intermediate coupling*)

The third case, i.e. the *intermediate coupling*, is the one which is valid for a rare earth element. The method to solve this kind of problem is to consider the reduced hamiltonian H_1, in which only the two potentials V_{ee} and V_{so} are taken into account:

$$H_1 = V_{ee} + V_{so}. \tag{2.21}$$

By choosing an appropriate set of functions, called *Russell-Saunders eigenfunctions* it is possible to diagonalise H_1 providing a set of solutions for the configuration of the N electrons in the 4f shell characterised by the quantum number of the angular momentum J.

Those J-states are degenerate states which can be associated to a linear combination of different L (quantum number associated to the orbital angular momentum) and S (quantum number associated to the spin angular momentum).

Coulomb interaction gives rise to terms characterised by S and L. A further splitting is caused by the spin-orbit interaction and leads to the $^{2S+1}L_J$ multiplet.

In principle, when a rare earth ion replaces a site in a crystalline matrix the free-ion model is not valid any more, as the nuclear charges of the host produce the

additional crystal field acting on the system. However, due to the shielding effect of the outer shells it is possible to use the free-ion model considering the crystal field a small external perturbation. Thus, Eq. 2.19 can be solved further using the perturbation theory.

Finally the effect of the crystal field solve another degeneracy giving rise to the Stark levels. The level splitting leading to the formation of the excited levels in rare earths elements is summarised in Fig. 2.18.

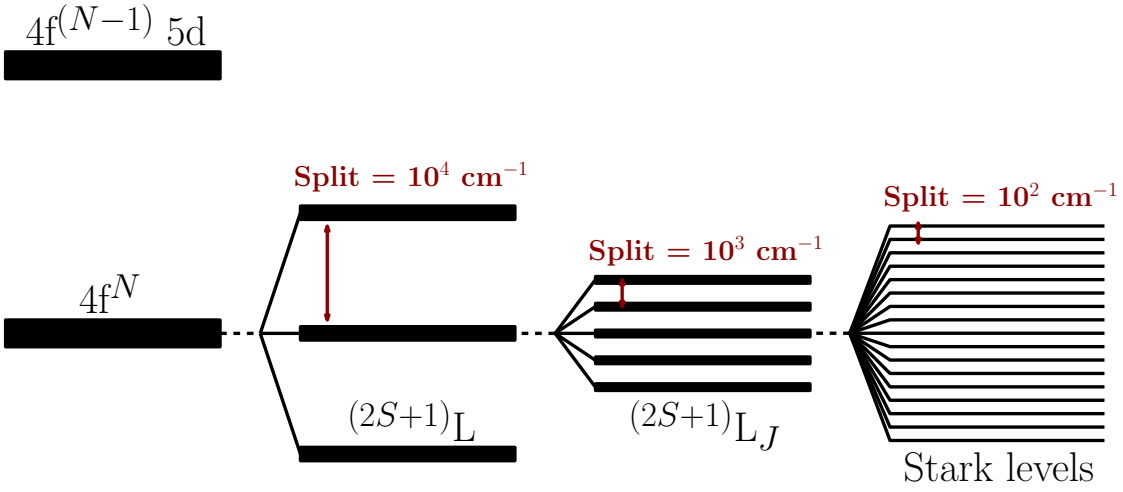

Figure 2.18: Schematic of the atomic interactions causing the 4f manifold splitting.

The Coulomb interaction produces a split of order 10^4 cm^{-1}, while the spin-orbital interaction determines a level split in the order of 10^3 cm^{-1}. Finally, the Stark split caused by the crystal field is of the order of 10^2 cm^{-1}. The energy levels for all different rare earths were measured by Dieke *et al.* considering a doped lanthanum chloride ($LaCl_3$) crystal [46]. They are summarised in Fig. 2.19 in what is generally referred to the *Dieke energy level diagram*.

The energy splitting slightly differs depending on the different host in which the rare earth is incorporated, but the dominant spectral features remain unchanged.

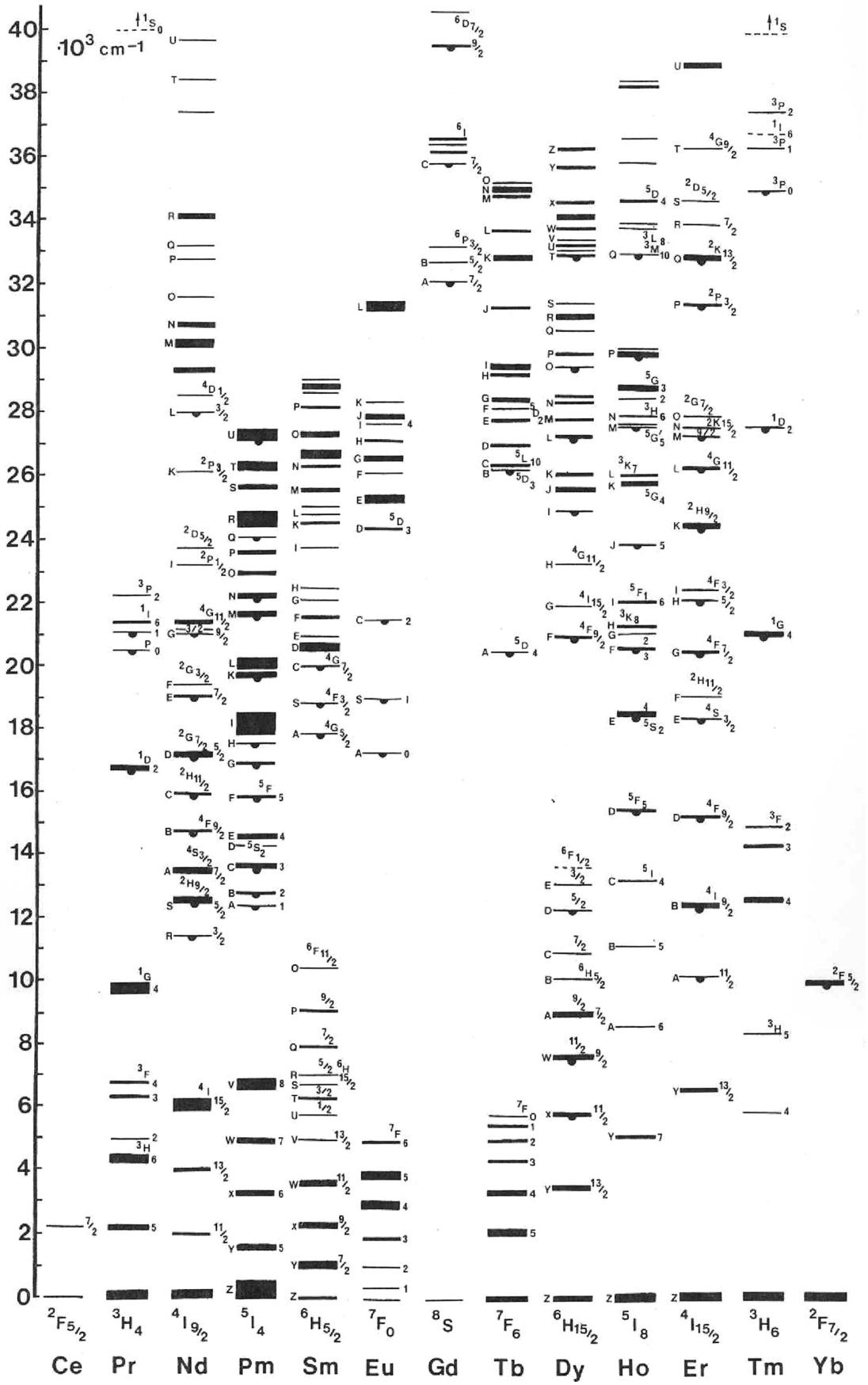

Figure 2.19: Dieke energy level diagram. Image taken from [46]

The more general form to label each level is represented by the following form:

$$^{2S+1}L_J$$

FInally, the Stark splitting is given by the degeneracy $2J + 1$ for integer values of J, or $J + \frac{1}{2}$ for half-integer values of J.

2.3.3 Energy Transfer Processes

In this section we will treat the interactions occurring between different rare earth ions in a host matrix. An ion can absorb energy from external factors like thermal radiation or light interaction. Due to the discrete energy level structure of rare earths, the absorption of an incident photon will occur only if the energy carried by the photon equalise the energy difference of the transition involved. The excited state will last for a limited amount of time, which in rare-earths can be in the order of few ms, before decaying back to the ground state, either emitting one or more photons (*radiative decay*) or without emitting any photon (*non-radiative decay*).

When the released energy is equal or lower than the incident radiation, the process is called *Stokes process*, while the emission of higher energy with respect to the one possessed by the incident photon is called *Anti-Stokes process*. Anti-Stokes processes are commonly observed in nature when the excess of energy above the excitation states is supplied by thermal population by few kT, like the well-known side bands in Raman effect. Anti-Stokes processes involving energy in excess of 10-100 times kT are also possible but require at least two excited ions to be considered. This is the case for rare earths materials, in which two or more excited ions can transfer their energy because of their proximity, easily leading to Anti-Stokes emission under moderate excitation density conditions.

The possible energy transfer mechanisms between rare earths ions have been extensively reviewed by Auzel [47]. We can differentiate between four kinds of

energy transfer:

a) Resonant radiative transfer

b) Resonant non-radiative transfer

c) Phonon-assisted energy transfer

d) Cross-relaxation

Considering a simple case of two ions, one excited, the *donor ion* (D), and one in its ground state, the *acceptor ion* (A), we can describe the four mentioned energy transfer mechanisms as schematised in Fig. 2.20.

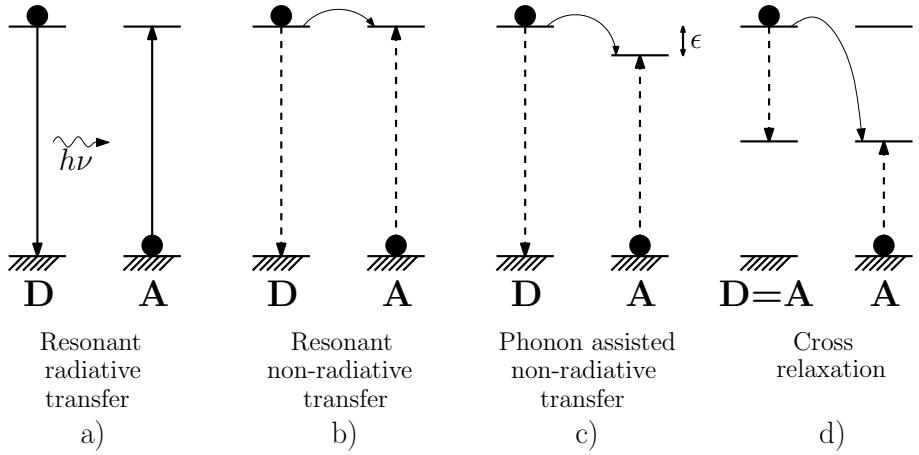

Figure 2.20: Energy transfer mechanisms.

In Fig. 2.20(a) the donor ion decays radiatively to the ground state emitting a photon of energy hν, which is then absorbed by the acceptor ion. Figure 2.20(b) is a similar situation but in this case no emitted photons are involved. The energy transfer occurs within a nearby ion and it is possible because of the resonant condition. The non resonant case (Fig. 2.20(c)) is only possible if the energy mismatch ϵ is provided by exchange of phonon energy. Lastly, Fig. 2.20(d) represents the cross relaxation energy transfer mechanism involving three energy levels, and in which both the donor and acceptor ions result in a final excited intermediate state.

2.3.4 Downconversion and Upconversion Mechanisms

DC via energy transfer is a direct consequence of the cross relaxation mechanism described in Fig. 2.20(d). As shown in Fig. 2.21, an external photon excites the donor ion to the excited level with energy E_2. The cross relaxation produces then a final state with both donor and acceptor ion in the first excited level. Finally, two photons with energy E_1 are emitted from both ions.

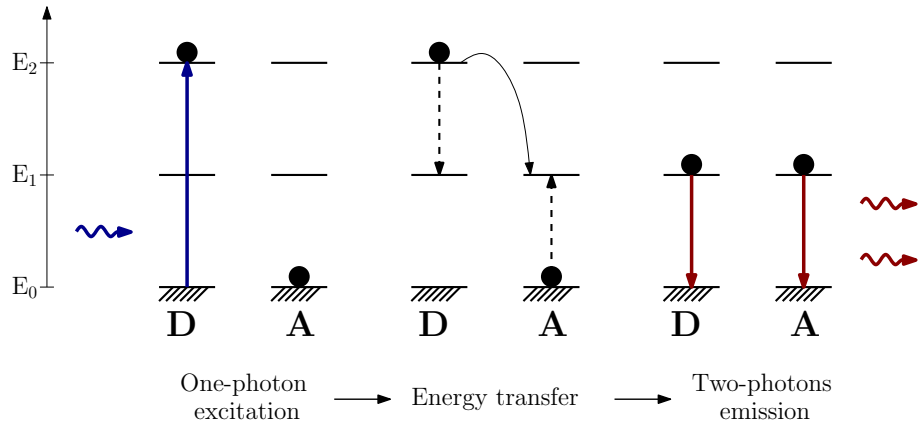

Figure 2.21: Downconversion mechanism via cross-relaxation.

Hence, the DC requires only one ion to be excited for the process to happen. In the case of UC both ions need to be in an excited state. UC requires two photons to be absorbed by the acceptor and donor ions. The following energy transfer from the donor to the acceptor brings the donor at its ground state and the acceptor to a higher excited level. The result is the emission of a single photon of energy higher than the incident one. This process, which is also known as ETU is schematised in Fig. 2.22.

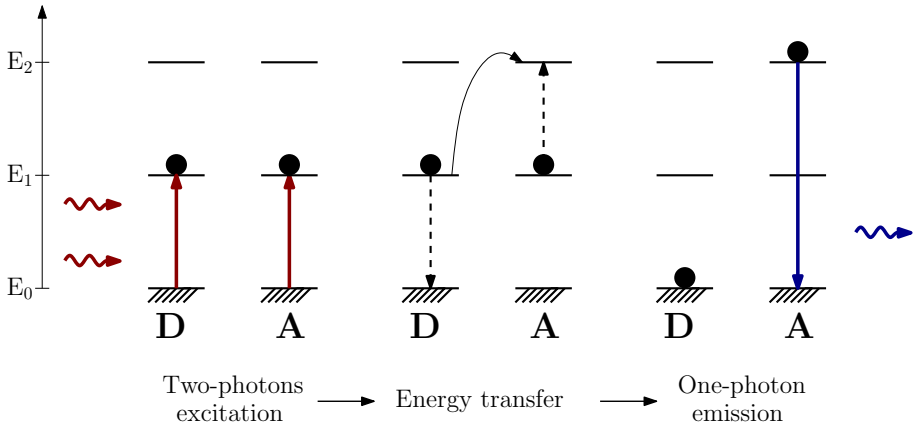

Figure 2.22: Schematic of the upconversion mechanism.

This process requires that the level E_1 and level E_2 are resonant, i.e. $E_1 - E_2 \sim \epsilon$, with ϵ representing the mismatch energy, but phonons within the crystal can assist the transition providing the necessary energy to create the resonance conditions (see section 2.3.5). Both DC and UC can occur also following different mechanism than the one presented. Those mentioned and schematised in Fig.2.21 and Fig. 2.22 are those whose efficiency is higher. Figure 2.23 summarises other two-photon upconversion mechanisms which can happen in a RE^{3+} ion.

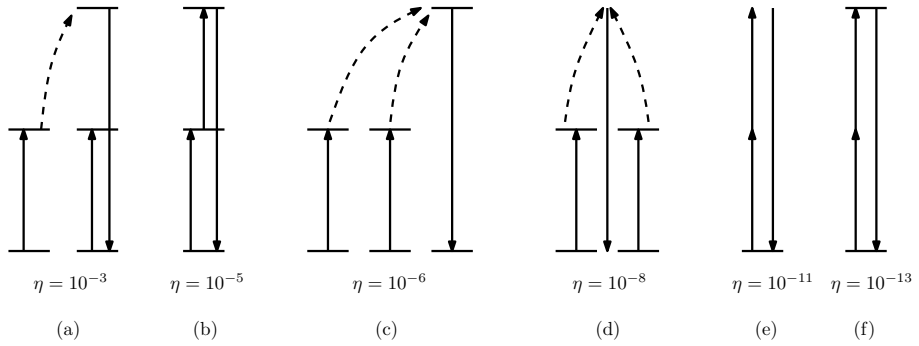

Figure 2.23: Two photons upconversion mechanisms. Two photons upconversion mechanisms: (a) ETU, (b) two-steps absorption, (c) cooperative sensitisation, (d) cooperative luminescence, (e) second harmonic generation, (f) two-photon absorption excitation.

For each case presented in Fig. 2.23, the opposite processes, defines the alternative DC mechanisms. If A and D represent two different types of ions, e.g. in the case of co-doped rare earth material, an energy transfer from one excited A ion to two D ions may occur under resonant condition without the need of an existing intermediate level.

This type of process is known as a second-order downconversion which is part of a more general class of phenomena called CET. [48]

CET also includes a particular UC process named cooperative sensitisation, which is the inverse process in which two donor ions transfer their energy to one acceptor ion resulting an emission of an higher energy photon.

2.3.5 Multiphonon Relaxation

In solid state physics, in presence of a crystalline structure the concept of *phonon* is introduced. A phonon is the quasi-particle associated to the vibrational modes of the crystal. Each vibrational mode corresponds to the collective movement of the atoms or molecules composing the crystalline structure. In-phase movements are named *acoustic phonons*, while out-of-phase movements are named *optical phonons*.

The order of magnitude of the energy carried by a single optical phonon depends on the crystalline matrix but it typically varies between 200-1000 cm^{-1}, i.e. belonging to the infrared electromagnetic spectrum. For this reason a crystal at room temperature is exposed to phonon transitions. In particular, in the case of rare earths doped materials, phonons can help fulfil the resonance conditions required by the energy transfer mechanisms. Another phenomenon in which phonons are involved is the *non-radiative multiphonon relaxation* between two energy levels.

An electron in an excited state can relax to the lower state without emitting a photon if the energy difference ΔE is sufficiently low to be balanced by the energy associated with the phonons in the crystal. The number of phonons which may be involved is temperature dependent, and generally for a room temperature environment there may be up to six phonons involved.

A simplified model to calculate the transition rate of non-radiative multiphonon relaxation is presented. Let us consider a multiphonon relaxation from an excited level involving p_i phonons correspondent to the i^{th} normal mode. Hence all the p_i

phonons possess the same amount of energy. The non-radiative transition rate W_{NR} is temperature dependent, and it is inversely proportional to the lifetime τ of the excited level. It results:

$$W_{NR}(T) = W_0(n_i + 1)^{p_i} \tag{2.22}$$

where n_i is the occupational number of the i^{th} mode and W_0 is the spontaneous transition rate when the temperature is 0 K. Therefore $W_{NR}(T)$ is an increasing function with the temperature, as n_i increases at higher temperature. Moreover, each phonon is associated with an energy $\hbar\omega_i$, where ω_i is the phonon frequency, and if we consider a non-radiative transition between two levels separated by an energy ΔE in which p_i phonons are contributing to it, it follows:

$$\Delta E = p_i \hbar\omega_i. \tag{2.23}$$

Considering for n_i a distribution which follows the Bose-Einstein statistics we obtain:

$$n_i = \frac{1}{e^{\frac{\hbar\omega_i}{kT}} - 1} \tag{2.24}$$

and replacing this in 2.22 we finally obtain the following expression for $W_{NR}(T)$:

$$W_{NR}(T) = W_0 \left(\frac{e^{\frac{\hbar\omega_i}{kT}}}{e^{\frac{\hbar\omega_i}{kT}} - 1} \right)^{p_i}. \tag{2.25}$$

Lastly, we have to consider the fact that the affected levels in the transition in a rare earth ion are the Stark levels which will be populated following a Boltzmann statistics. Taking into account this additional contribution, we can write the expression for $W_{NR}(T)$ as following:

$$W^{NR}(T) = \frac{\sum_i W_i^{NR}(T) g_i e^{-\frac{\Delta_i}{kT}}}{\sum_i g_i e^{-\frac{\Delta_i}{kT}}} \tag{2.26}$$

where $W_i^{NR}(T)$ is the non-radiative decay rate corresponding to the i^{th} level having a degeneration g_i and an energy separation Δ_i from the lower level of the manifold. The resulting trend depending on the temperature and the number of phonons is shown in Fig. 2.24.

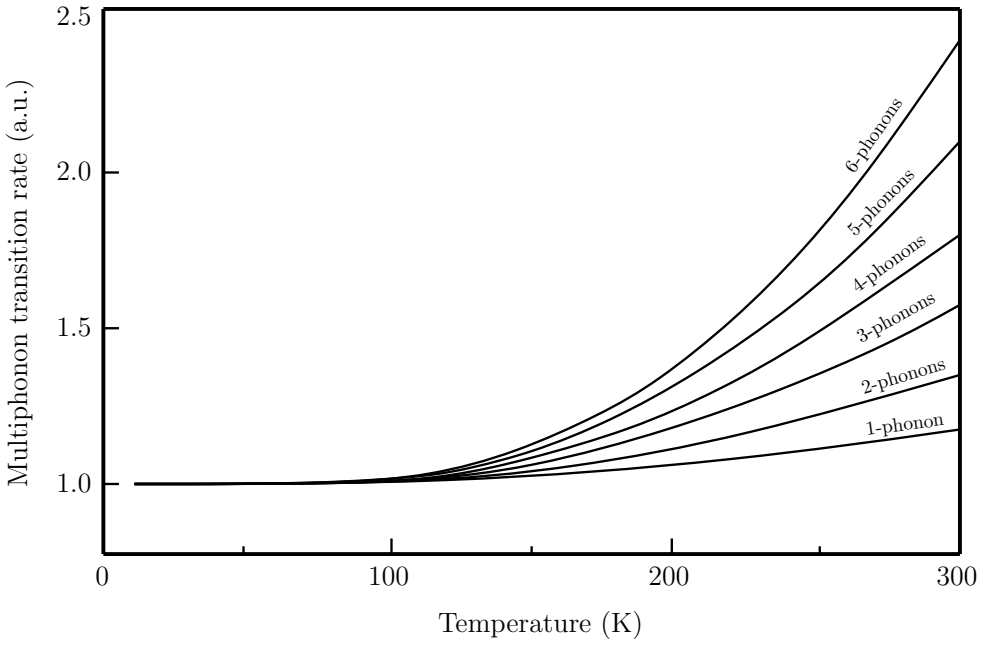

Figure 2.24: Non-radiative multiphonon transition rate dependence on the temperature.

It results that the non-radiative multiphonon relaxation rate is highly dependent on the order of the process, i.e. on the number of phonons involved. Multiphonon relaxation is one cause which decreases the fluorescence intensity. The choice of materials with low phonon energies is required to avoid those losses affecting the luminescence properties and their performances, especially when measurements are taken at room temperature as in our case.

2.4 Beyond the Shockley-Queisser Limit

As described in section 2.2.5, a silicon based single junction PV device could reach an efficiency no higher than 33%. This limitation is mainly due to thermalisation and transparency losses (see Fig. 1.2). One of the methods which could reduce those loss mechanisms is to use spectral converters, like rare earth doped materials, whose luminescent properties have been presented in section 2.3. In this section we show how to harvest the luminescent properties of rare earth to design a spectral conversion enhanced PV device which can, in principle, overcome the limit imposed by Shockley and Queisser.

2.4.1 Downconversion and Upconversion Enhanced PV Devices

Instead of considering the device presented in Fig. 1.5 in which the downconverter and upconverted layers were integrated together with a bifacial solar cell, in literature it is common to consider two separated devices: the upconversion enhanced photovoltaic device (UC-PV) device and the downconversion enhanced photovoltaic device (DC-PV) device. Figure 2.25 shows the two devices, DC-PV device coupled to a silicon solar cell, and the UC-PV coupled to a bifacial silicon solar cell.

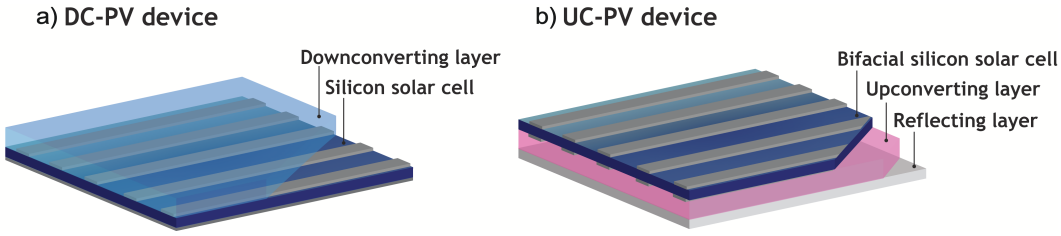

Figure 2.25: Downconversion and Upconversion Enhanced PV Devices.

The upper limits efficiencies presented in the next section will refer to the analysis on the two separated devices.

2.4.1.1 DC-PV device efficiency limit

Trupke *et al.* firstly investigated the theoretical efficiency limit of a DC-PV device considering a downconverter luminescent layer placed on the front or on the rear of a solar cell. The study was based on a detailed principle analysis in accordance to what was done by Shockley and Queisser for the case of a bare solar cell [13].

However, in Trupke's analysis it was assumed that the downconverter only absorbs photons with energy higher than $2E_g$, generating two pairs for each absorption, while the solar cell absorbs only photons between the bandgap E_g and $2E_g$. The last assumption can be used in the case of the geometry with the downconverter on the front, but it does not apply to the case of the downconverter placed on the rear surface, as silicon solar cell absorption at energies higher than $2E_g$ is quite important. For this reason Trupke suggested that the geometry with a downconverter on the rear side can be realised using dye sensitised solar cells [49]. The analysis conducted by Trupke stated that a PV device made of a downconverter layer on the top of a solar cell has an efficiency limit of 38.6%. It also was shown that this efficiency limit can be reached providing the downconverter material and the solar cell have the same refractive index of $n = 3.6$, in order to increase the collection of DC luminescence towards the solar cell.

A more elaborate model in which both cell and downconverter refractive index are considered has been discussed by Badescu *et al.* [50]. In their study, the reflection losses introduced by considering the refractive index lowered the efficiency of the bare silicon solar cell ($n = 3.6$, $E_g = 1.1eV$) to 21%, which is then increased up to 26% if a downconverter layer is placed on top of the solar cell. The case considered by Badescu *et al.* does not take into consideration any possible improvement provided by antireflecting layer or light trapping. This is the reason behind the reduced performances of the DC-PV device analysed in terms of absolute efficiencies.

The effects of those possible improvements were accounted for by De Vos *et al.* [51] who found the effect of light trapping between the DC layer and the solar

cell might increase the limit energy conversion efficiency up to 35%.

A further calculation made by Abrams *et al.* [52] considered a layer of DC nanoparticles placed on top of a solar cell. In their model, the way light by the DC nanoparticles is emitted is controlled by varying a geometrical parameter A, whose value is $A = 0.5$ for isotropic emission and $A = 1$ for directional emission (in that case corresponding to all photons emitted towards the solar cell). In the ideal case of directional emission ($A = 1$) the efficiency limit of the DC-PV device was calculated to be around 34%, while the calculation of the bare solar cell (assumed to have a refractive index equal to 4) was 27.7%. Instead, no net gain resulted for isotropic emission ($A = 0.5$). An additional result from Abrams' analysis [52], which was also treated in Badescu's work [50], was to demonstrate how the strong influence of non-radiative losses on the DC process could remove the benefits of using a DC-PV device.

2.4.1.2 UC-PV device efficiency limit

Also for the case of a UC-PV device the first calculation of an upper efficiency limit was done by Trupke *et al.* [49]. They considered a detailed balance analysis in which the upconverter acts as a light emitting diode absorbing light above two energy bandgaps with lower values than the solar cell bandgap and emitting light above the energy bandgap of the solar cell. The calculated upper limit was 40.2% for the silicon solar cell case and for an AM1.5 solar spectrum.

Badescu [53] reviewed the previous model considering the effect of non radiative recombination in both solar cell and upconverter, plus the effect of their refractive index. He showed that the refractive index has a huge impact on the final efficiency of an UC-PV device, which in some cases can also cancel the beneficial effects of the upconverter.

Atre and Dionne [54] performed a more realistic analysis accounting for non-ideal absorption and radiative recombination in the solar cell and nonradiative relaxation

within the upconverter. Their results indicated that the efficiencies of both conventional PV cells can be substantially improved using upconverting materials, even including non-idealities.

Johnson and Conibeer [55] revised the detailed balance model describing the UC-PV device for the specific case of a c-Si solar cell under the AM1.5G solar spectrum. They found that the limiting efficiency of an ideal solar cell with a band gap of 1.117eV may be increased from approximately 33% to 40% with ideal up-conversion.

Brigggs *et al.* [56] considered a highly realistic narrow-band, non unity quantum yield upconverter, showing that based on existing rare earth-based upconverters, the UC-PV device efficiency will not improve more than 1%. However, their calculations showed that these upconverters can significantly increase cell efficiencies from 28% to over 34% with improved quantum yield, despite their narrow bandwidths.

Finally, Johnson *et al.* [57] expanded their generalised UC enhanced silicon solar cell model to a more specific model in which the upconverter is an erbium doped phosphor. The modifications considered resulted in a maximum relative enhancement of about 7%. It would corresponds to an absolute increase from 28% to 30% in cell efficiency, which is lower than what stated by Briggs *et al.* [56].

2% absolute increase in solar cell efficiency would represents a big achievement in the framework of PV technologies. However, in order to reach that stage much work needs to be done in increasing the photoluminescent quantum yield of the rare-earth based DC and UC materials.

The following chapters will present the experimental work that I have done in order to understand what are the optical losses limiting the performances of this class of materials (Chapter 4 and 5).

Making use of this acquired knowledge, I will show, in Chapter 6, how it was possible to reach one the highest photoluminescence quantum yield ever reported for a specific upconverter material at the time of publication of this thesis.

Chapter 3

Materials and Methods

This chapter is dedicated to the description of the methodology used to synthesise and to optically characterise the upconverter and downconverter materials, whose results are presented in the following chapters. Cerium/ytterbium co-doped borate glasses were investigated as a downconverter material, and an erbium doped BaY_2F_8 crystal has been studied as an upconverter material. The two materials have been grown by two different collaborator groups. The borate glasses were synthesised by our collaborators at the State Key Laboratory of Structural Chemistry, Chinese Academy of Sciences, in Fuzhou, China, while the BaY_2F_8 crystals were made by our collaborators at Physics Department Laboratories, University of Pisa, Italy. Those samples were optically characterised in our laboratory at Heriot-Watt University. The characterisation methods, which will be described in this chapter include absorption, photoluminescence excitation and photoluminescence quantum yield.

3.1 Material Synthesis Methods

As previously mentioned, the rare earth doping process consists of the substitution of one or more sites in the host material, which can be either crystalline or amorphous. The rare earth doping level is defined as the percentage of doped atoms or moles with respect to the total number within the host. In this case we will refer to *atomic* or *molar concentration* indicated by %at or %mol, respectively. Alternatively, the doping level can be expressed as density of ions, i.e. the number of doped ions per unit of volume, consequently the unit of measure is cm^{-3}.

3.1.1 Ce^{3+}/Yb^{3+} Co-Doped Borate Glass

Borate glasses [$70B_2O_3$-7BaO-8CaO-(15-x)La_2O_3] co-doped with Ce^{3+}/Yb^{3+} were prepared using the melt-quenching method. The mixture of pulverised crystalline raw materials is placed in a crucible to be fused into a viscous liquid at a temperature of about 1250 K. The melt is then cooled very slowly and casted into a mold. The glass is usually annealed at a temperature slightly higher than the glass transition, to remove any thermal stress developed during the forming process [58]. This method has the advantage of obtaining materials which are very large in size.

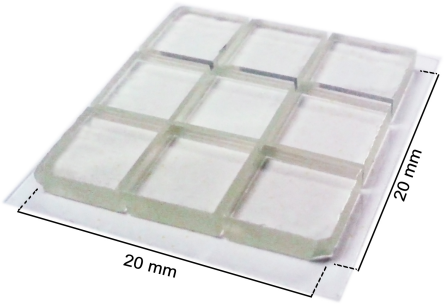

Figure 3.1: Ce^{3+}/Yb^{3+} Co-Doped borate glass.

The Ce^{3+} concentration was fixed to 0.5 %mol, while different Yb^{3+} concentrations 1%, 2%, 5%, and 10% were prepared, as described in [59]. An un-doped borate glass sample was also fabricated to be used as a reference sample. The glass samples were polished down to dimensions of 20 mm x 20 mm x 2.2 mm. Seven

smaller samples (6 mm x 6 mm) were cut from the 0.5%Ce^{3+}/1%Yb^{3+} glass sample (see Fig. 3.1 and each one was optically polished to different thicknesses (refer to Section 3.1.3) ranging from 0.29 mm to 2.18 mm.

3.1.2 Er^{3+} Doped BaY_2F_8 Single Crystal

Er^{3+} doped BaY_2F_8 single crystal samples were grown by the Czochralski method (see fig. 3.2) in a concentration of 10at%, 20at% and 30at% using a self-made furnace developed by the Physics Department Laboratories in Pisa. This growing technique, also called *crystal pulling*, has the advantage of producing crystals with a low level of defects [60]. The principal steps involved in the Czochralski process, schematised in Fig. 3.2, are the following:

(a) The raw materials (usually in the form of powders) are placed in a crucible

(b) The crucible is heated up via an induction coil, driven by a radiofrequency field placed around it, until the melting temperature is reached.

(c) A suitable *seed*, which is a small undoped crystal identical to the one to be grown, is lowered to the surface of the melt forming a solid-liquid interface. A gradient of temperature is established such that, at the height of the seed, corresponds a temperature low enough to start the nucleation of a crystalline structure.

(d) The seed, which is connected to a rotating rod, is successively slowly pulled up allowing the melt below to solidify and growing as a single crystal.

Growth powders [BaF_2-$2YF_3$] with 99.999% purity level were used in order to avoid contamination affecting the optical quality of the crystals. Vacuum condition of 10^{-7} mBar and high-purity (99.999%) argon atmosphere were established before and during the growth process. A temperature of 972 °C, pulling rate 0.5 mm/h, rotation rate 5 rpm were used as growth parameters. After the growth, X-ray

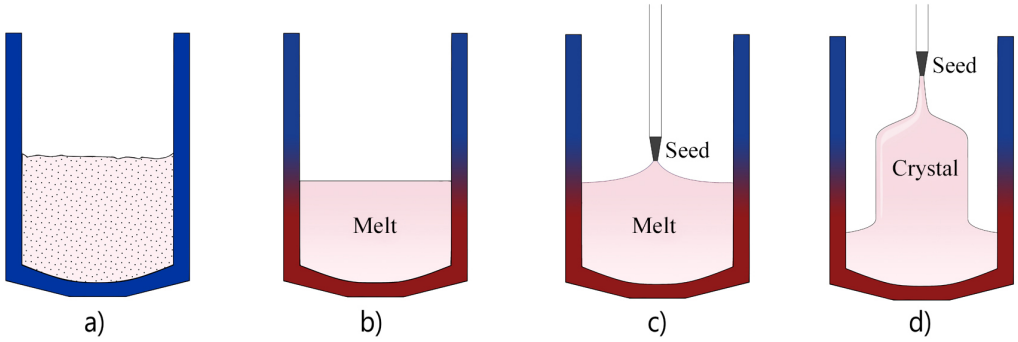

Figure 3.2: Czochralski method.

backscattering Laue diffractometry has been performed to check the crystallinity. The resulting boule is shown in Fig. 3.3.

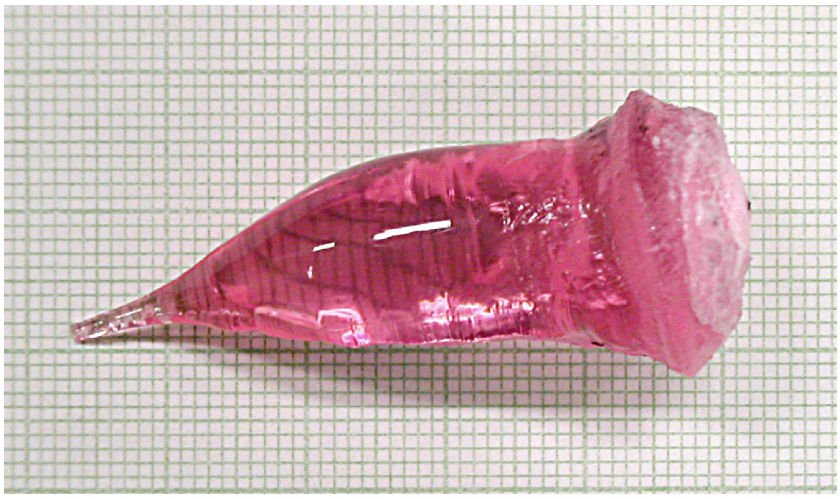

Figure 3.3: Boule of BaY_2F_8 single crystal.

Finally, the resulting crystals were cut and optically polished to produce samples of 5 mm x 5 mm dimensions, as displayed in Fig. 3.4.

3.1.3 Polishing Techniques

A *LaboPol-1* polishing machine from *Struers* (see Fig. 3.5) was used for grinding and polishing our samples.

The polishing machine has a 200 mm plate rotating at fixed speed of 250 rpm. The plate can be exchanged depending on the different preparation needed, from grinding to final polishing. Our machine did not include an automated sample holder, therefore a self-made one has been design suitable for our purpose. It consists

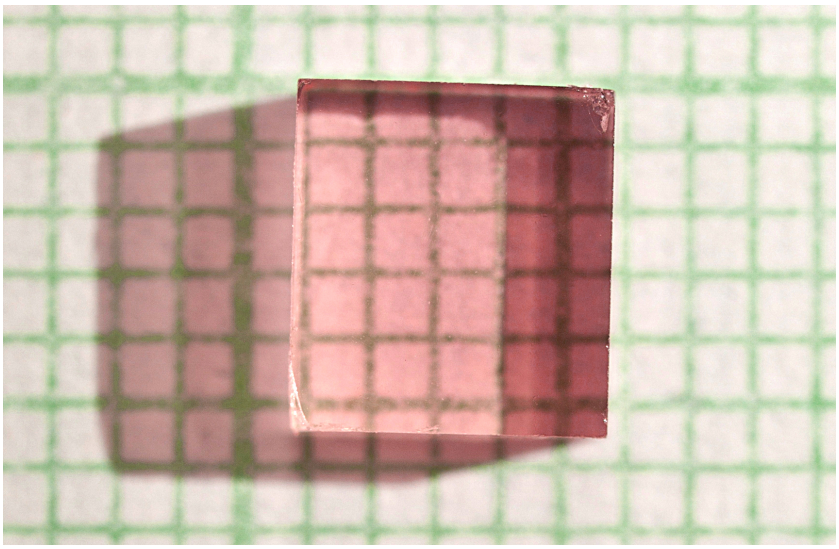

Figure 3.4: BaY_2F_8 sample cut and polished.

in a mobile arm with a treated rod at its far end to which the sample holder is attached. Because our study consisted of producing a set of samples having different thicknesses, the sample holder, as shown in Fig. 3.6, has been designed so that up to 4 samples can be glued on top of a metal support, whose height can be adjusted via a micrometer screw.

After the grinding process (Fig. 3.7), the samples are gradually polished diminishing the grade of the sandpaper and finished using a colloidal alumina (Al_2O_3) slurry consisting in 1 μm particles suspended in deionized water.

3.2 Material Characterisation Methods

3.2.1 Absorption Measurements

Suppose that a monochromatic light beam with an intensity $I_{in}(\lambda)$ traverses an absorbing medium having thickness L, as shown in Fig. 3.8.

Due to absorption, the transmitted beam intensity outside the medium $I_{out}(\lambda)$ decreases with respect to $I_{in}(\lambda)$. The two intensities are related by the formula

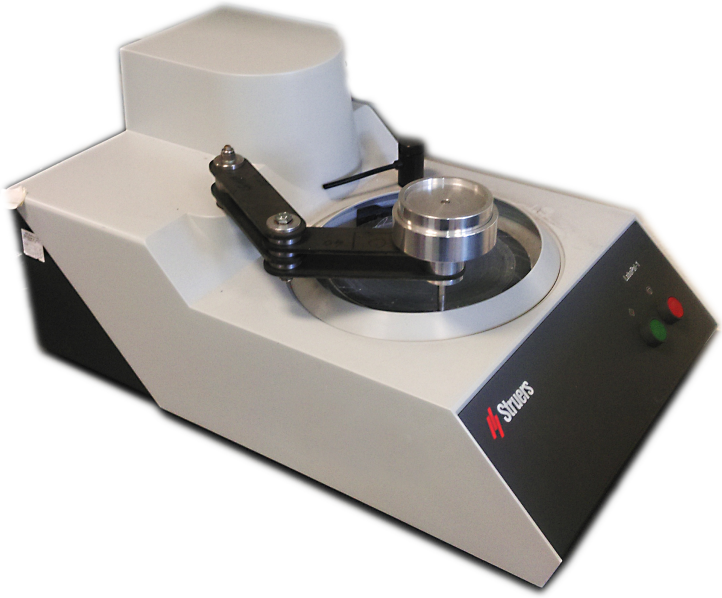

Figure 3.5: LaboPol-1 polishing machine from Struers integrating a self-made sample holder.

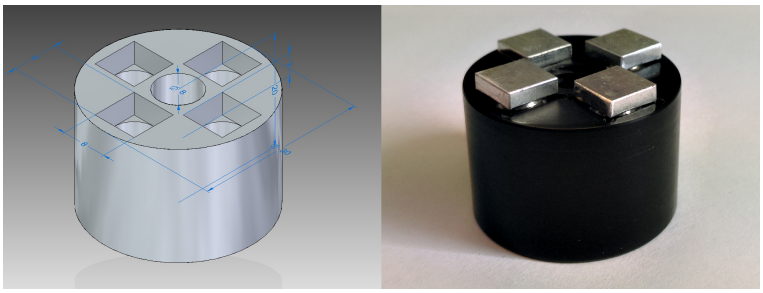

Figure 3.6: Sample holder.

$$\frac{I_{out}(\lambda)}{I_{in}(\lambda)} = e^{-\alpha(\lambda)L} \tag{3.1}$$

where the constant $\alpha(\lambda)$ is called the *absorption coefficient*, which is assumed constant within the whole length. In case the absorption coefficient is not constant, Eq. 3.1 has the more general formula

$$\frac{I_{out}(\lambda)}{I_{in}(\lambda)} = \exp\left(-\int_0^L \alpha(\lambda, \mathbf{r})dl\right) \tag{3.2}$$

Equation 3.1 is often called *Beer's law* [61]. The absorption coefficient is defined as the ability of a material to attenuate light of a given wavelength per unit length, and its unit of measure is typically given in cm^{-1}. The ratio $\frac{I_{out}(\lambda)}{I_{in}(\lambda)}$ defines the

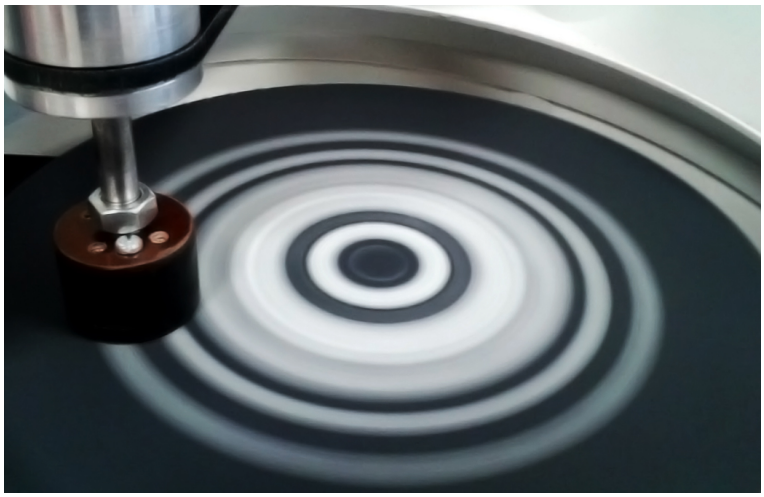

Figure 3.7: Grinding process.

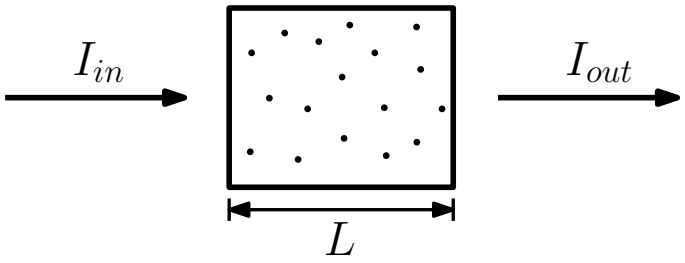

Figure 3.8: Absorption in a medium of thickness L.

transmissivity $T(\lambda)$ of the material, which is linked to the absorbance $A(\lambda)$ by the *Beer-Lambert law*:

$$A(\lambda) = -log_{10}T(\lambda) \tag{3.3}$$

Thus, known the absorbance $A(\lambda)$, the absorption coefficient $\alpha(\lambda)$ can be calculated as a function of the thickness L:

$$\alpha(\lambda) = \frac{A(\lambda)\ln(10)}{L} \tag{3.4}$$

In a rare earth doped material absorption and emission processes occur through a number of energy levels, whose origin has been explained in Section 2.3. The discrete structure of those levels allow absorption and emission only if the energy of the photons $h\nu$ is equal to the energy difference of the transitions involved. Let us consider a basic two-level quantum system having energies E_1 (level 1) and E_2

(level 2), with $E_2 > E_1$ as displayed in Fig. 3.9.

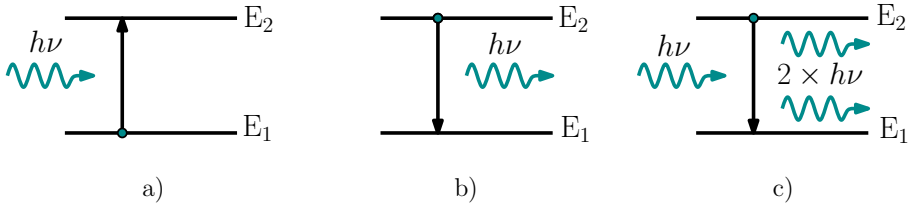

Figure 3.9: Absorption and emission processes in a two-level quantum system. a) Ground state absorption/Excited state absorption, b) spontaneous emission, c) stimulated emission.

Three fundamental mechanisms can be distinguished:

- ***Ground state absorption (GSA) or excited state absorption (ESA)*** This is the basic photon absorption process in which electrons belonging to level 1 are excited to level 2 providing that $h\nu = E_2 - E_1$. When level 1 represents the ground state, the process is called GSA; when instead level 1 represents an excited state, the process is called ESA. Given the atomic number density N_{at} of rare earth dopant ions, the electron population densities N_i associated to each level and an incident photon flux Φ_{inc}, the population density dynamics of level 1 is described by:

$$\left(\frac{dN_1}{dt}\right)_{abs} = -\sigma_{12}\Phi_{inc}N_1, \tag{3.5}$$

with σ_{12} being the *absorption cross section* from level 1 to level 2 defined as

$$\sigma_{12}(\lambda) = \frac{\alpha(\lambda)}{N_{at}} \tag{3.6}$$

- ***Spontaneous emission*** This is the process in which an electron populating level 2 decays back to the lower energy level 1 and a photon with energy $h\nu = E_2 - E_1$ is emitted. In this case the variation of population density N_2 due to spontaneous emission $\left(\frac{dN_2}{dT}\right)_{sp}$ changes according to:

$$\left(\frac{dN_2}{dt}\right)_{sp} = -\frac{N_2}{\tau_{21}}, \tag{3.7}$$

where τ_{21} is the time taken to decay spontaneously from level 2 to level 1.

- ***Stimulated emission*** A photon with energy $h\nu = E_2 - E_1$ can also stimulate, without being absorbed, the radiative decay of an electron belonging to level 2. The additional photon resulting from the stimulated emission has the same direction, frequency, phase and polarisation of the incident one. For this case the population density of level 2 is described by:

$$\left(\frac{dN_2}{dt}\right)_{st} = -\sigma_{21}\Phi_{inc}N_2, \tag{3.8}$$

where σ_{21} is the *emission cross section*. σ_{21} is equal to σ_{12} have the same value if the degeneracy of the two levels is the same. Otherwise the following expression is valid

$$g_1\sigma_{12} = g_2\sigma_{21} \tag{3.9}$$

with g_1 and g_2 being the degeneracy of level 1 and 2, respectively.

Absorption spectra of our samples were measured using a double beam, double monochromator, ratio recording spectrophotometer *Perkin-Elmer Lambda 950*, operating in a wavelength range of 175-3300 nm (see Fig. 3.10).

Figure 3.10: Spectrophotometer *Perkin-Elmer Lambda 950*.

The spectrophotometer directly measures the absorbance $A(\lambda)$, from which it is possible to calculate, knowing the sample thickness L, the absorption coefficient $\alpha(\lambda)$ using Eq. 3.4. The schematic of the optical system provided by the spectrophotometer is represented in Fig. 3.11.

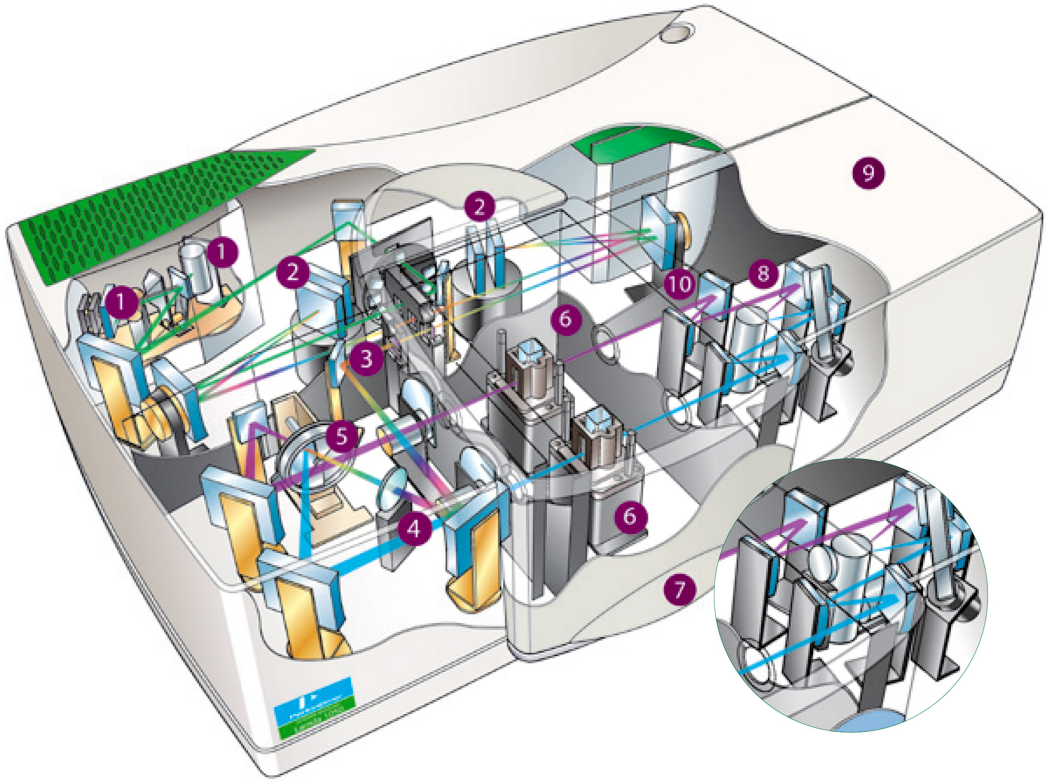

Figure 3.11: Schematic of the optical system of Perkin Elmer Lambda 950 spectrophotometer. 1) Light sources, 2) double holographic grating monochromators, 3) common beam mask, 4) common beam depolarizer, 5) chopper beam splitter, 6) beam attenuators, 7) sample compartment, 8) detectors 9) second sampling area (for integrating sphere module), 10) Additional detectors (not present in the Lambda 950 model). Image adapted from [62].

The light sources are a deuterium lamp and a tungsten-halogen lamps, which cover the working wavelength range of the spectrophotometer. The light is appropriately pre-filtered and collimated before reaching the entrance slit of the first monochromator. In the monochromator the light is dispersed by a holographic grating (1440 lines/mm in the UV and 360 lines/mm in the NIR) and directed towards the entrance slit of the second monochromator. At the output slit a monochromatic beam with high spectral purity is formed. The double monochromator allows the instrument to reach a resolution of 0.05 nm in the UV/VIS range and 0.20 nm in the NIR range.

The monochromatic beam passes through a chopper, made of a mirrored segment, a window and two dark segments. The chopper acts as a beam splitter. In fact, when the radiation strikes on the mirror segment this creates the so called *sample beam* while passing through the window segment the beam is redirected by

other mirrors to form a second beam called the *reference beam*. When the beam passes through the dark segment no radiation is detected, and this is used to record the *dark signal* of the detector. Finally, a scan over a selected wavelength range is performed and the intensity ratio of the two beams is detected by a photomulitplier R6872 for the UV/VIS range, or by a peltier cooled lead sulfide (PbS) detector for the NIR range.

To correct for the influence of external factors, such as the temperature and air humidity, a measure in absence of the sample has to be performed before every set of measurements. This is the so called *autozero* or *baseline* measurement. The software will then use this correction for the actual measurements performed with the sample to test in place.

Moreover, for rare earth doped materials we have to consider the absorption due to the host. Its contribution is significant especially in the UV region. However, the absorption lines typical of rare earths can be easily distinguished. To perform a more accurate measurement the baseline scan is carried out with an undoped sample situated along the reference beam path.

In some cases it is required to perform a polarised measurement. To do so, two polariser filters can be placed in the sample compartment. Sometimes, especially for laser applications, we are interested in measuring the absorption spectra for incident radiation with parallel or perpendicular polarisation with respect to the crystalline axis. For photovoltaic applications, this is not required as the sunlight is non-polarised except for a small portion of diffuse light. All absorption spectra reported in the following chapters have been measured at room temperature (300 K).

3.2.2 Photoluminescence Measurements

Photoluminescence is the process of exciting a medium via absorption of photons followed by the emission of further photons, which can have same or different energies with respect to the incident ones.

Luminescence can also be induced by electron flow, like the case of electroluminescence in semiconductors, where an external voltage provides the necessary energy to populate the conduction band, from which electron-hole recombination causes photon emission. This is, for example, the case of a light emitting diode (LED). In this work we will perform experiments which involve photoluminescence only.

A spectrofluorometer is an instrument used to characterise the photoluminescence properties of materials. For our experiments we made use of an *Edinburgh Instrument FLS920* spectrofluorometer (see Fig. 3.12).

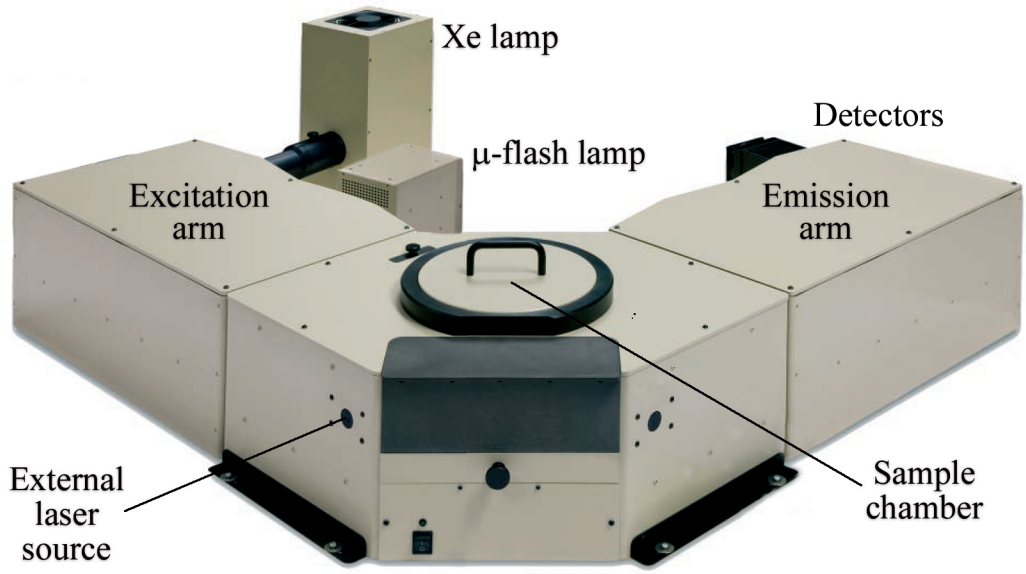

Figure 3.12: Edinburgh Instrument FLS920 spectrofluorometer. Image adapted from [63].

The instrument is fitted with different light sources, which can be spectrally filtered in the excitation arm. An additional external laser source attached to a secondary port of the sample chamber was also used. The sample chamber is provided with a 50 mm focal length lens used to focus the incoming light on the sample and

a 50 mm focal length lens to collect the emitted light, which is further filtered in the emission arm. Finally two different detectors, one for the UV/VIS (Extended red photomultiplier tube (PMT)), and one for the NIR region (NIR PMT), are employed to cover a total wavelength range of 200-1400 nm. A more detailed scheme of the spectrofluorometer is represented in Fig. 3.13.

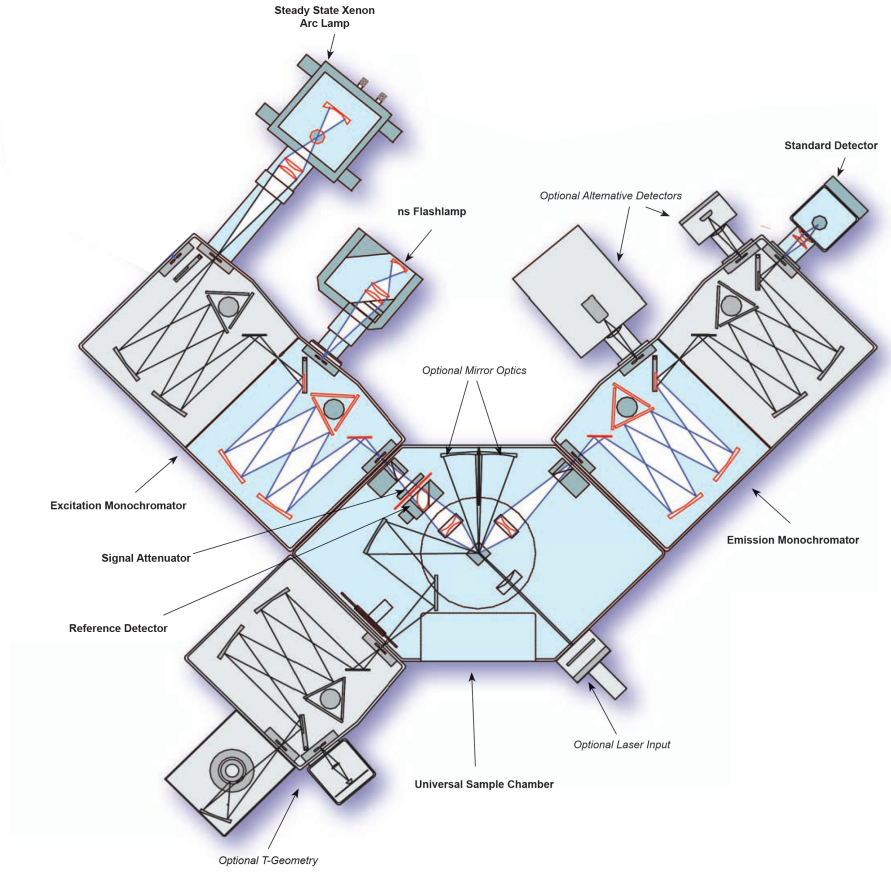

Figure 3.13: Internal schematic of the spectrofluorometer Edinburgh Instrument FLS920. Image adapted from [63].

Both excitation and emission arms are composed by a double CzernyTurner monochromator [64] with holographic diffraction gratings having variable groove density. The monochromators have computer controlled entrance slits (excitation) and exit slits (emission).

The different gratings are optimised for a specific wavelength, called the *blaze wavelength*. The spectrofluorometer is fitted with three different gratings with blaze wavelengths of 500 nm, 750 nm and 1200 nm. Their spectral optical response when used in combination with the two detectors is represented in Fig. 3.14.

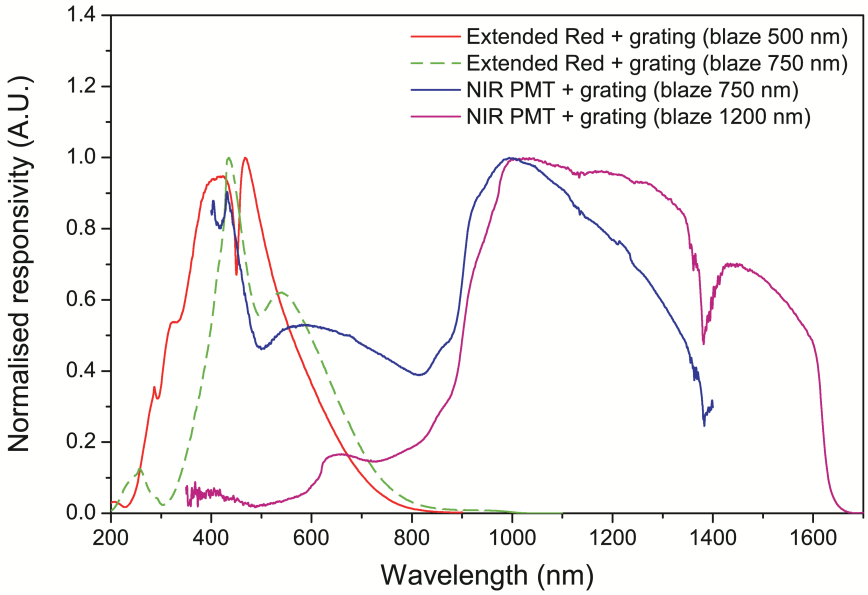

Figure 3.14: Gratings response

The sample to measure is mounted in a sample holder placed at the centre of the sample chamber (see Fig. 3.15).

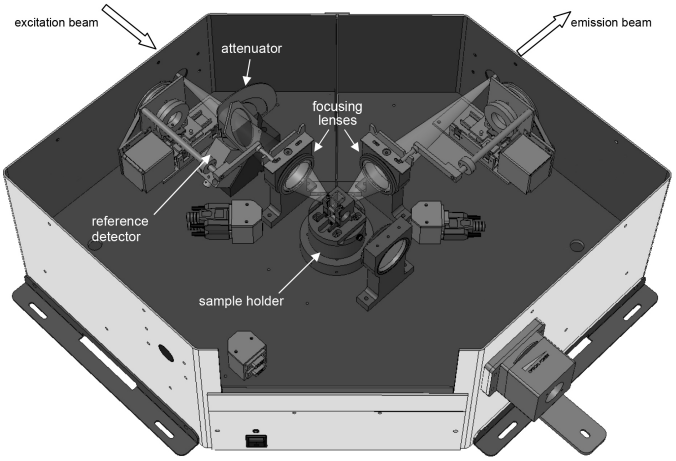

Figure 3.15: Sample chamber of the spectrofluorometer Edinburgh Instrument FLS920. Image adapted from [63].

The sample holder can be chosen accordingly to the type of sample which has to be measured. Sample holders suitable for either liquid or solid samples are available. Additionally, the sample chamber can be fitted with an 150 mm integrating sphere for quantum yield measurements, which can be mounted in place of the standard sample holder.

3.2.3 Light Sources

Three different light sources were used. For the downconverter material characterisation (presented in Chapter 4) in the UV/VIS a Xenon arc lamp was used due to its broad emission spectrum covering UV/VIS and NIR.

For the characterisation of the upconverter material (presented in Chapter 6) a tunable laser emitting in the region of 1500 nm was used. The tunability, in the range 1450-1590, was required to investigate the upconverter's behaviour along the wide absorption band of interest.

Finally, a micro-pulsed light source was used to measure the decay time of the upconverter.

All details for each light sources are presented below:

- **Xe900 450W Xenon arc lamp.** The Xe900 is a 450 W ozone free xenon arc lamp that emits continuous radiation from 230 nm to 2600 nm. The lamp is fully adjustable in two orthogonal planes for alignment optimisation. The emission spectrum of the lamp is displayed in Fig. 3.16.

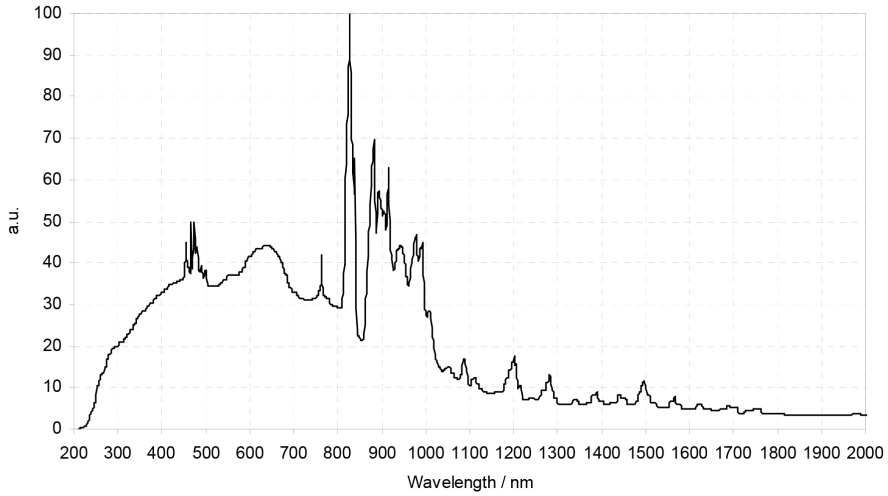

Figure 3.16: Xe900 450 W Xenon arc lamp emission spectrum.

- **HP-Agilent 8168F tunable laser.** This is a Fabri-Pérot InGaAsP tunable laser, with a tunability range of 1450-1590 nm. The output of the laser

was coupled into an single mode optical fibre (Thorlabs, P3-1550A-FC-1) and collimated with a lens of numerical aperture (NA) 0.15 (Thorlabs, F280APC-1550).

Figure 3.17: HP-Agilent 8168F tunable laser.

- **μF900 microsecond pulsed flashlamp.** The μF900 is a pulsed xenon microsecond flashlamp producing short, typically a few μs pulses. The lamp is triggered by the spectrofluorometer controller and the optical pulses can reach repetition rates up to 100 Hz. This is employed for time-resolved photoluminescence lifetime measurements in the range from microseconds to seconds. The emission spectrum of the lamp is displayed in Fig. 3.18.

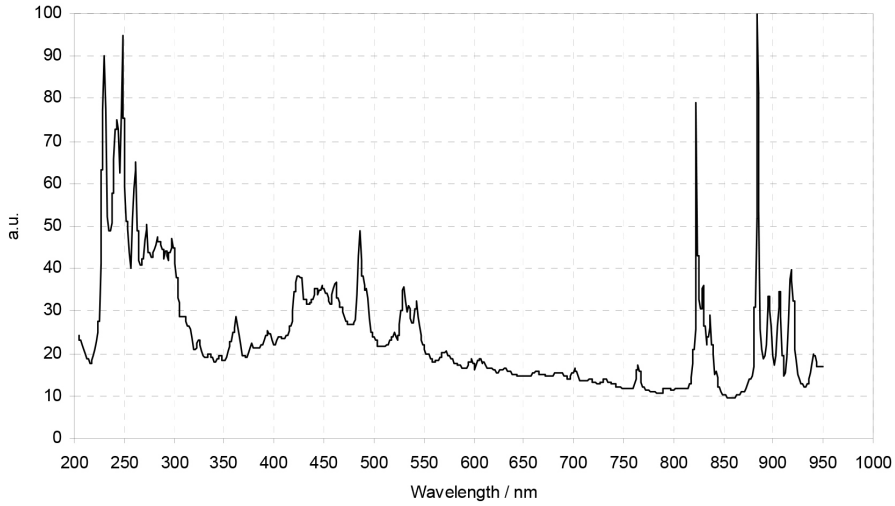

Figure 3.18: μF900 microsencond pulsed flashlamp emission spectrum.

3.2.4 Detectors

Two photomultiplier tube detectors were used in this work that cover a very wide spectral range from 200 nm to 1700 nm. Both were fitted to the emission arm of the spectrofluorometer described previously. The details of the two Hamamatsu detectors are:

- **Hamamatsu R928 extended red PMT.** This is the UV/VIS detector featuring a Hamamatsu R928P PMT air cooled operating at a temperature of -20 °C. The response spectral range is 200-870 nm with a dark count rate of 100 cps.
- **Hamamatsu R5509-72 NIR PMT.** This is the NIR detector featuring a Hamamatsu R5509-72 PMT operating in a nitrogen flow cooled housing at -80 °C. The detector spectral range is 300-1700 nm with a dark count rate of 200000 cps.

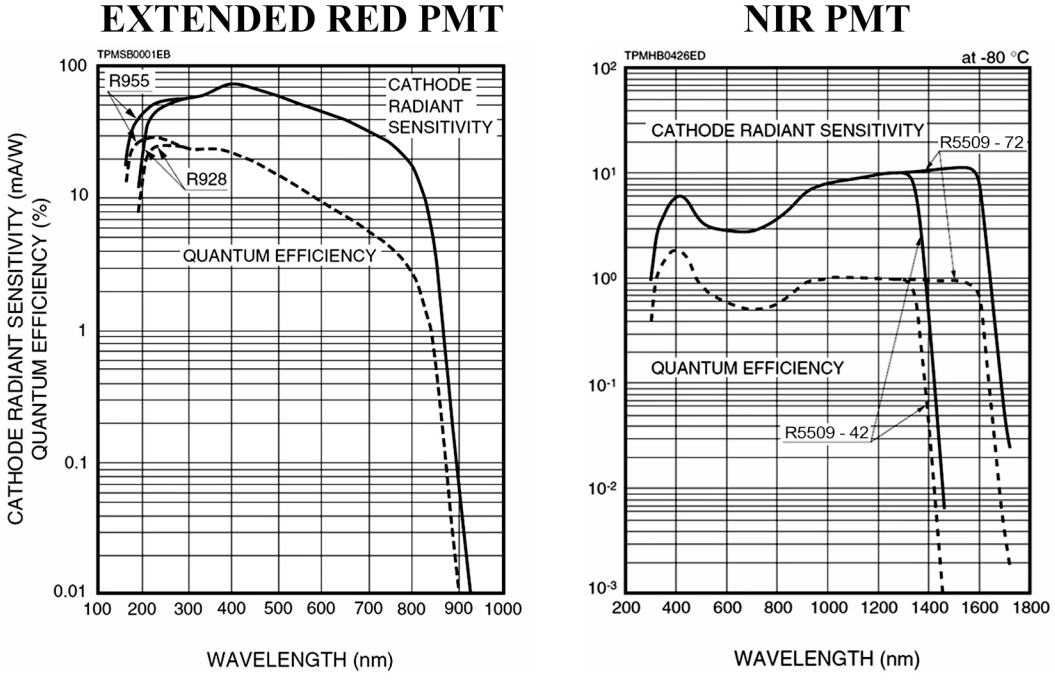

Figure 3.19: Extended Red and NIR PMT detector's spectral response.

3.2.5 Determination of Absolute Photoluminescence Quantum Yields

By using the calibrated system made of spectrofluorometer and integrating sphere, it is possible to compare absolute photoluminesce intensity within different samples.

The determination of the PLQY is an important parameter used to evaluate the optical performance of different classes of materials. In this thesis this technique is used to evaluate the spectral conversion performances of rare earth doped materials.

The spectral conversion (either DC or UC) is a process made of two steps; the absorption of photons at a certain wavelength λ_{abs}, and the emission of photons at a different wavelength λ_{em}. Therefore, in the following definitions, we will refer to *absorbed/incident photons*, having wavelength λ_{abs}, or to *emitted photons*, having wavelength λ_{em}.

Two different types of PLQY can be defined:

- The iPLQY, i.e. the ratio between emitted photons over the incident photons.

$$iPLQY = \frac{\text{total flux of emittted photons}}{\text{total flux of incident photons}}$$

- The ePLQY, i.e. the ratio between emitted photons over the absorbed photons.

$$ePLQY = \frac{\text{total flux of emittted photons}}{\text{total flux of absorbed photons}}$$

In our analysis we only dealt with monochromatic excitation, resulting in a well defined narrow pump wavelength λ_{abs}. Instead, the upconverted or downconverted emission usually results in a broad spectrum. Thus, the determination of the total flux of the emitted photons is done via integrating the emission spectrum over the whole range wavelengths.

Another crucial part is the calculation of the total absorbed photons, which for broadband excitation, or scattering samples, or the combination of both, require to

use a detailed characterisation technique (for review see [65]). Instead, in our case, the use of transparent and scattering-free materials in combination with monochromatic excitation, does not require to perform additional spectroscopic techniques in order to evaluate both iPLQY and ePLQY.

3.2.6 Integrating Sphere

The integrating sphere was used for both iPLQY and ePLQY measurements. The internal surface of the sphere, supplied by Jobin-Yvon, is covered with Spectralon, an extremely high reflective material produced by Labsphere, having a reflectivity greater than 98% over the range 275-1800 nm (see Figure 3.20).

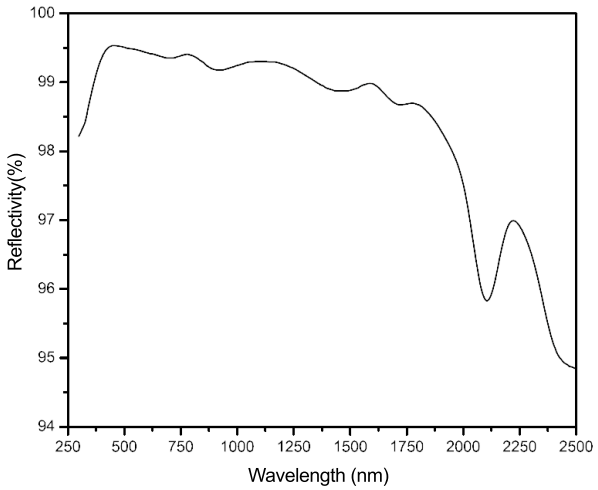

Figure 3.20: Spectralon reflectivity. Image adapted from [66].

As schematised in Figure 3.21, the sample holder is placed in the centre of the sphere. Two circular ports of 20 mm diameter are present, serving as the entrance of the excitation pump and the exit for the fluorescence emission. Finally, a circular baffle (made of Spectralon) is placed in front of the exit port to avoid the collection of the direct emission from the sample. This is to ensure that all detected light outside the sphere has made at least one reflection from the Spectralon surface.

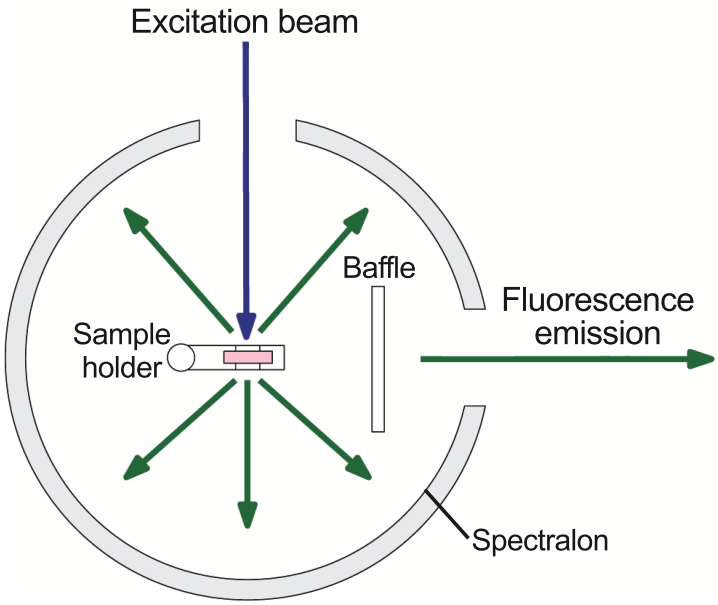

Figure 3.21: Integrating sphere scheme.

Chapter 4

Ce^{3+}/Yb^{3+} Co-Doped Downcovnerting Borate Glasses: Effect of Self-Absorption

This chapter reviews the current state of the art of DC studies for PV applications. It also reports the luminescent properties of a downconverting Ce^{3+}/Yb^{3+} borate glass. Following the discussion of the results, an analytical model is presented to determine the constrains imparted by self-absorption loss mechanism on the luminescence emitted from the DC material. The model is then validated via the analysis of photoluminescence emission spectra measured for different sample thicknesses. This defines a new limit for the optical efficiency of a DC material.

This chapter expands on material from the following publications:

Boccolini A., Marques-Hueso J., Chen D., Wang Y., and Richards B. S. "Physical performance limitations of luminescent down-conversion layers for photovoltaic applications."
Solar Energy Materials and Solar Cells, Vol. 122, (2014).

Boccolini A., Marques-Hueso J., Chen D., Wang Y., and Richards B. S. "Optimization of thickness in luminescent down-conversion layers for photovoltaic applications."

OSA meeting on Renewable Energy and the Environment, Optical Nanostructures and Advanced Materials for Photovoltaics, Tucson, Arizona, USA, (2013).

4.1 Downconversion for Solar Cells

Due to the promise of improved performance for the mainstay PV technology, DC research has attracted much attention over the last decade. The majority of publications have been mainly focused on materials chemistry studies of promising materials (for reviews see [67] and [68]) and, to date, no practical demonstration of DC-enhanced solar cell performance have been achieved. A similar strategy has been already implemented in PV by using luminescent down-shifting materials [69] (similar to DC but with maximum iPLQY of unity) with up to 9% enhancements being reported on CdTe thin film PV modules [70].

DC has been employed in lighting technology, such as mercury-free fluorescent tubes, as well as plasma displays [71]. Materials based on RE^{3+} ions have been studied and high values of iPLQY approaching 190% were measured for systems based on Gd^{3+} and Eu^{3+} [72–74]. Despite the high iPLQY values, the DC mechanism for this particular system is based on conversion of VUV photons ($\lambda < 200$ nm) into VIS photons. This process is not relevant for either space- or terrestrial-based PV applications where the solar spectrum begins at λ=200 nm or 300 nm, respectively. It is also important to highlight that the ePLQY of this system is only 32%, firstly due to the weak absorption of the ^6G_J level of the Gd^{3+} ion, and secondly due to the strong parasitic absorption in the $LiGdF_4$ host [75].

4.1.1 Downconverters Based on Yb^{3+} Co-Doped Materials

A more promising way to apply DC to PV devices are UV/VIS to NIR DC materials, typically based on co-doped system RE^{3+}-Yb^{3+}. The UV/VIS light is absorbed by a RE^{3+} sensitizer ion, which then transfers its energy to two neighbouring Yb^{3+} acceptor ions and exciting them from the $^2F_{7/2}$ ground state to the excited level

$^2F_{5/2}$ (∼1.2 eV). The resulting NIR (λ= 980 nm) emission from the latter level corresponds to photon energies close to the bandgap of a silicon solar cell.

The advantage of the Yb^{3+} ion originates from the absence of intermediate levels between the $^2F_{5/2}$ level and the ground state, which increases the probability of radiative emission. Moreover, the UV/VIS light could be transmitted for energies higher than 1.2 eV due to the absence of higher energy levels. The DC process involved within these materials may be different depending on the type of RE^{3+} which is present. In Section 2.3.4, two types of DC have been identified; first-order DC based on cross-relaxation energy transfer, and a second-order DC via CET.

First-order DC have been demonstrated for systems in which the rare earth element has one energy level at around 20000 cm^{-1} and one at half the energy (around 10000 cm^{-1}) being resonant with the $^2F_{5/2}$ level of the Yb^{3+} ion. This is the case of co-doped system based on Pr^{3+}-Yb^{3+} and Er^{3+}-Yb^{3+} [76–79].

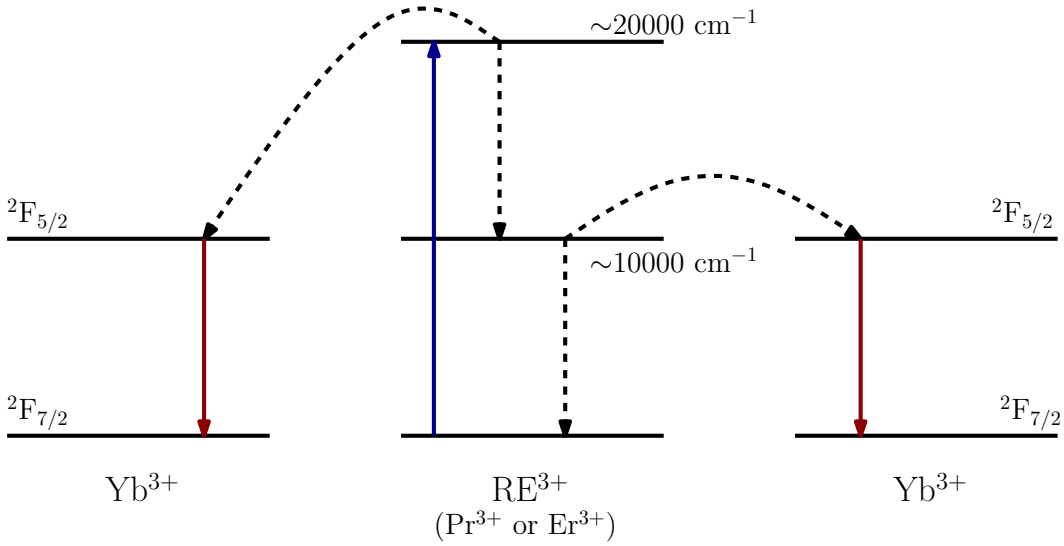

Figure 4.1: First-order downcoversion.

For second-order DC via CET the intermediate level at around 10000 cm^{-1} is not required and the transfer happens directly from the excited level of the RE^{3+} ion to two Yb^{3+} ions. This is the case of co-doped systems based on Tb^{3+}-Yb^{3+}, Tm^{3+}-Yb^{3+} and Ce^{3+}/Yb^{3+} [59, 74, 80].

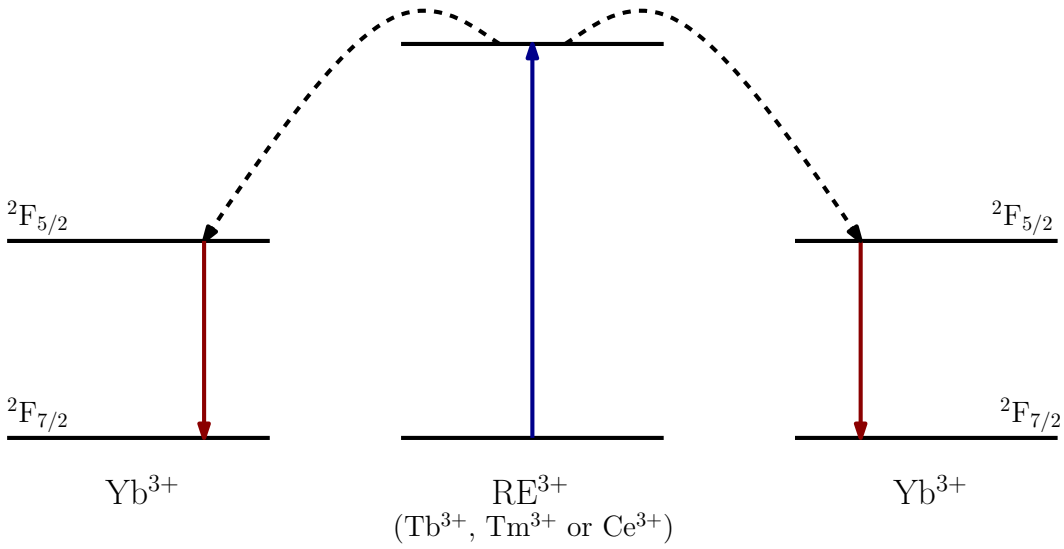

Figure 4.2: Second-order downcoversion via CET.

Being a second-order process, DC via CET will be less efficient than via cross-relaxation. However, the first-order DC is subjected to multiphonon relaxation, which causes a decreasing of the DC efficiency due to non-radiative losses [81]. In order to reduce, or ideally avoid multiphonon relaxation, hosts with low phononic energies should be utilised. The second-order DC is less subjected to this type of loss mechanism. Indeed, for the systems based on Tb^{3+}-Yb^{3+}, Tm^{3+}-Yb^{3+} and Ce^{3+}/Yb^{3+} the levels involved with the DC are very well separated and no multi-phonon relaxation phenomena competes with the DC process.

Another problem connected with both the DC mechanisms is the narrow band of absorption of the UV/VIS excitation level. For second-order DC this issue seems to be overcome adding a third dopant, as Gd^{3+}, which is characterized by a broader absorption in the UV region [82].

Of the previous systems, the Ce^{3+}/Yb^{3+} couple is the one which satisfies most of the required characteristics. Broadband UV absorption and high absorption cross section (around 10^{-18} cm^2 [59]), due to the 5d shell, make this system a promising DC material.

In a Ce^{3+}/Yb^{3+} system (see Fig. 4.3), the UV pump excites the Ce^{3+} ion into the

$5d$ manifold, which is subjected to a Stokes shift into the $4f$ manifold, allowing the DC to occur via CET to the Yb^{3+} ions [59]. CET in borate glasses is a non-resonant energy transfer assisted by phonons with a maximum phonon energy in the range of 1310-1380 cm^{-1} [83].

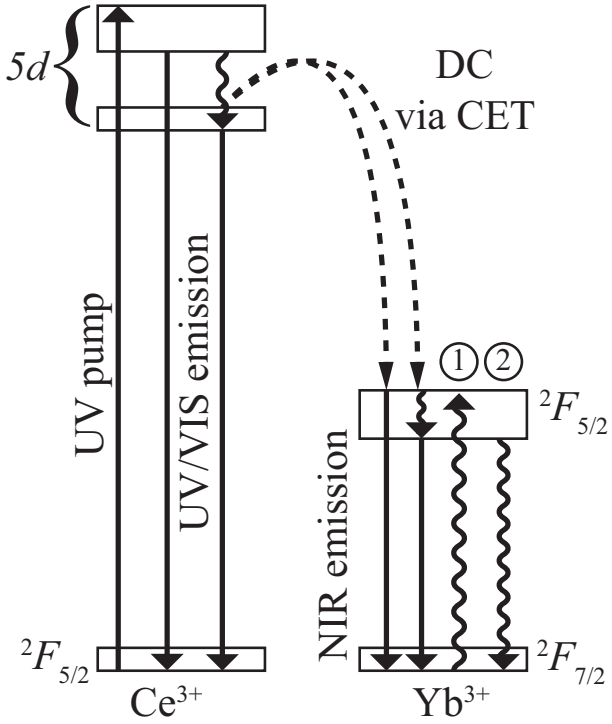

Figure 4.3: Schematic of DC via CET in Ce^{3+}/Yb^{3+} system. The NIR emission from the Yb^{3+} ions is decreased by self-absorption (1) and non-radiative relaxation (2).

This ion pair is interesting because the rare earth metal ion Ce^{3+} exhibits a strong broad absorption band at the UV rather than the weaker and discrete bands obtained from other RE^{3+} ions. However, the second-order DC via CET is mostly non-resonant, which means that phonons are needed to match the resonances conditions, lowering the energy transfer efficiency (ETE). Despite of this, using materials based on co-doping of Ce^{3+}/Yb^{3+} represents a way to study others type of losses connected with the Yb^{3+} emission, like the quenching of the emission or the self-absorption of the emitted radiation.

The performance of RE^{3+}-Yb^{3+} co-doped materials have been investigated through the theoretical evaluation of the ETE from RE^{3+} ions to Yb^{3+} ions via time-dependent photoluminescence measurements [67]. This evaluation method, pro-

posed by Vergeer *et al.* [84], consists in measuring the decrease of the decay lifetime of the excited level of the RE^{3+} ions with the increasing concentration of Yb^{3+} ions. The ratio of the measured lifetime (corresponding to a specific concentration value) compared to the natural lifetime (measured in a Yb-free sample) allows the theoretical ETE of the process, relative to each Yb^{3+} concentration, to be estimated. From the literature, the theoretical ETE estimations are very close to the maximum theoretical of 200% [84–87].

However, achieving such ETE values typically require Yb^{3+} concentrations greater than 20 %mol, which also promotes other losses mechanisms such as quenching of the emitted radiation. This is a non-radiative relaxation phenomena that, firstly decreases the intensity of the fluorescence, and secondly results in self-absorption of the emitted radiation due to the overlapping absorption and emission spectra. These two loss mechanisms represent the main reasons that DC materials have not yet demonstrated the desired performance enhancement for PV devices [77]. Self-absorption of Yb^{3+} have been modeled through a rate equation model to describe its impact on lifetime measurements [88].

Our approach will instead focus on studying the effect of self-absorption on the ePLQY considering an optical model based on Beer-Lambert law. Therefore, this study aims to quantify the losses due to the self-absorbed radiation in order to facilitate the design of future DC-PV devices. An optical model has been developed and an analytical formula has been derived to demonstrate that an optimal thickness exists for the DC layer, which can minimize the fraction of emission lost to self-absorption. The model has been validated by performing spectroscopic measurements for different Yb^{3+} doping levels and different thickness on a specific DC system based on a transparent glass system, comprised of borate glasses co-doped with Ce^{3+} and Yb^{3+} ions.

4.1.2 Absorption Measurements

Absorption spectra were measured with a spectrophotometer (Perkin-Elmer, Lambda 950) with a resolution of 1 nm over 250-1200 nm wavelength range. Any effects from the host matrix were accounted for via the undoped reference sample. All the measurements on the samples have been performed at room temperature (25 °C).

The absorption spectra of the borate glass samples co-doped with 0.5%mol Ce^{3+} and different Yb^{3+} doping concentration is plotted in Fig. 4.4.

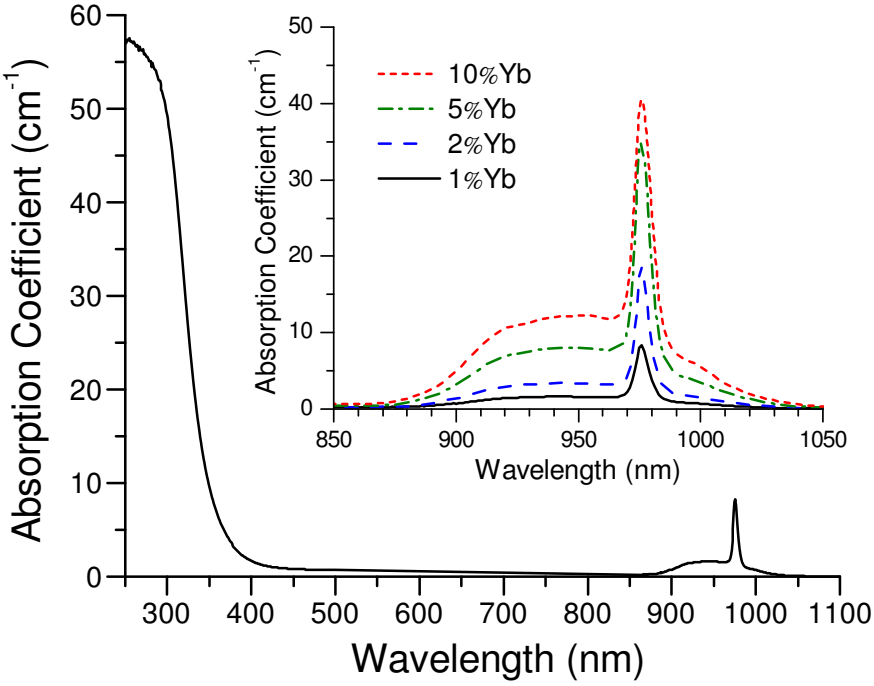

Figure 4.4: UV/VIS/NIR absorption spectrum for the sample Ce0.5%-Yb1%. The inset graph shows the NIR absorption for four different Yb^{3+} molar concentrations.

Two main absorption regions in the spectra were observed; one in the UV band, due to the $4f \rightarrow 5d$ transition of the Ce^{3+} ions, and the other in the NIR region, due to the transition $^2F_{7/2} \rightarrow ^2F_{5/2}$ within the Yb^{3+} ions. The sample is transparent in the VIS range in order not to interfere with the spectral regions where the solar cell already operates relatively efficiently [89]. As shown in the inset graph in Fig. 4.4 the measured absorption coefficient is proportional to the concentration of the Yb^{3+} ions. In particular, the peak at 978 nm reached different values going from 8.4 cm^{-1} for the 1%Yb^{3+} sample to about 41 cm^{-1} for the 10%Yb^{3+} sample. The UV region

of the absorption spectra remains the same for all samples because it only depends on the concentration of Ce^{3+} ions, as no absorption in that region (see Figure 2.19).

4.1.3 Photoluminescence Spectra

Fluorescence spectra were obtained using the calibrated spectrofluorometer (Edinburgh Instruments, FLS920) equipped with xenon lamp excitation source and a liquid nitrogen cooled NIR PMT (Hamamatsu, R5509-72). The uncertainty for the calibrated data is ± 3%.

The photoluminescence spectra were measured using excitation at 305 nm (full width at half maximum (FWHM) = 12 nm). The corresponding NIR emission, as shown in Fig. 4.5, is characterized by a sharp peak centered at 978 nm and a broader one at 1010 nm.

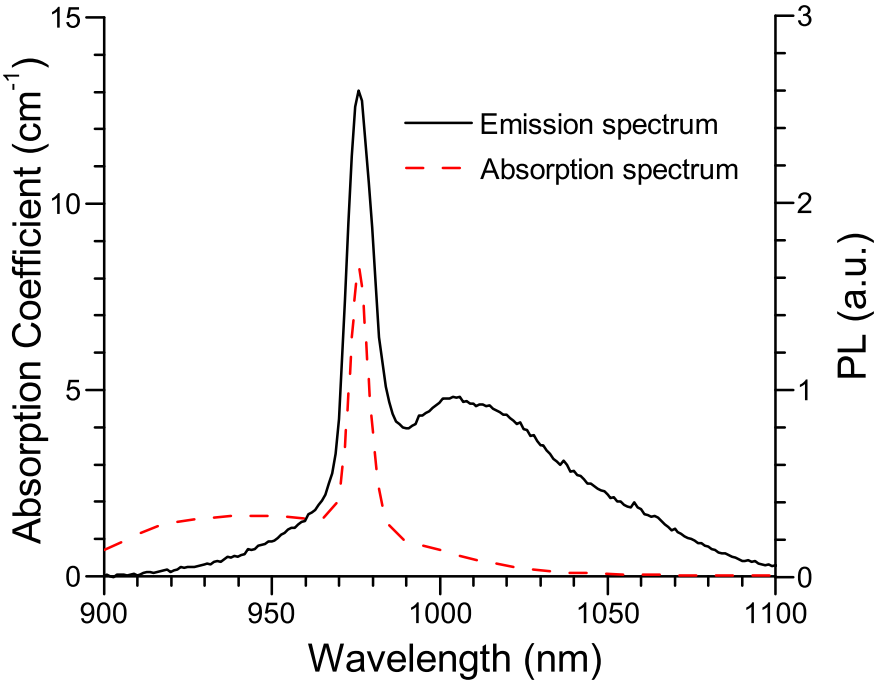

Figure 4.5: Overlapping of absorption and emission spectrum in the NIR region for the sample Ce0.5%-Yb1%.

Figure 4.5 also displays the overlap between the absorption and emission spectra in the NIR region, which is particularly pronounced at the 978 nm peak.

4.1.4 Photoluminescence Spectra Dependence on Yb^{3+} Concentration

The photoluminescence spectra measured for all different Yb^{3+} concentrations were normalized such that the total area is equal to unity and a multipeak fit performed in order to evaluate the branching ratio of the 978 nm emission with respect to the total. The results are presented in Fig. 4.6.

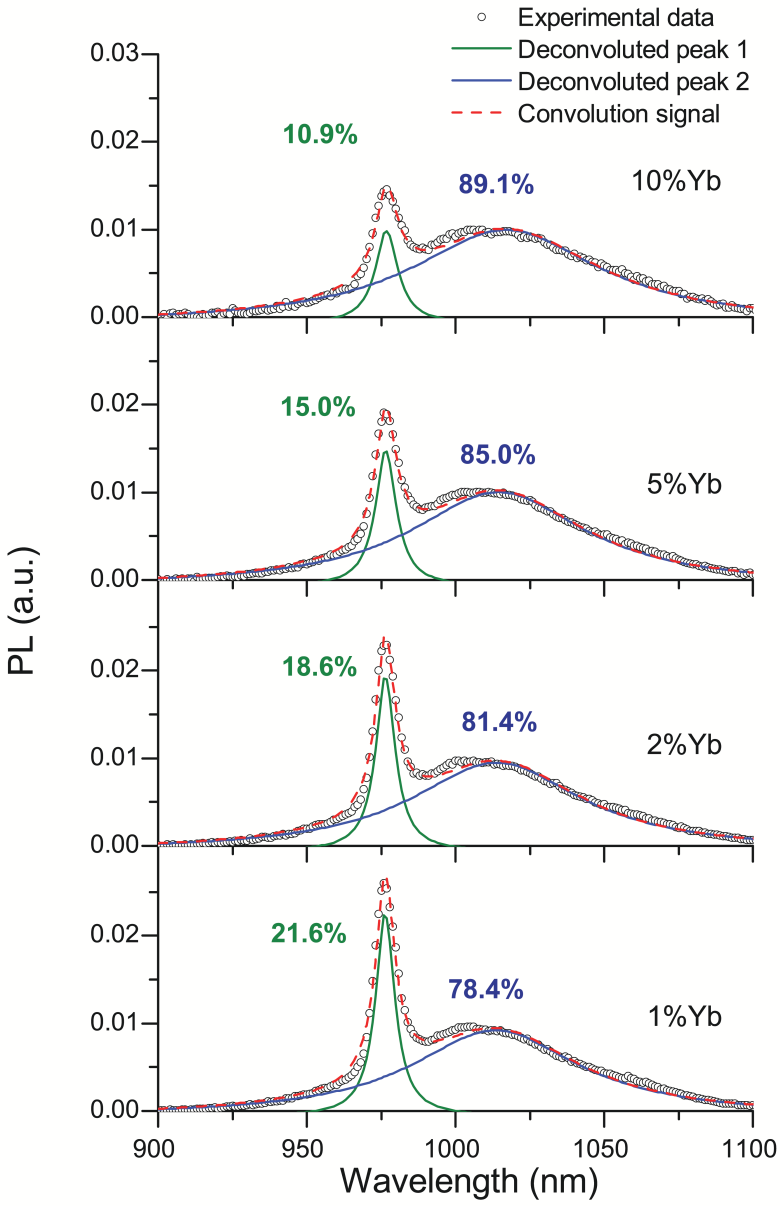

Figure 4.6: Emission spectra for different Yb^{3+} doping level concentration and relative emission branching ratio. Open circles represent the measured spectra, blue solid lines are the single peak function and red dashed-lines are the convolution of the two peaks.

They indicate that the branching ratio of the 978 nm emission decreases from 21.6% to 10.9% as the Yb^{3+} doping level increases from 1%mol to 10%mol doping concentration.

There are two possible mechanisms to explain this trend. Firstly, this could be caused by non-radiative relaxation from the higher states of the $^2F_{5/2}$ manifold to its lower state causing the red-shift of the emission [90]. This phenomenon becomes increasingly important as the Yb^{3+} ions concentration increase. Secondly, the considerable decrease of the peak intensity at 978 nm may be attributed to the self-absorption of the emitted radiation within the Yb^{3+} ions themselves. However, the losses due to self-absorption could not be extrapolated from Fig. 4.6 and another experiment has to be set up to quantify which loss mechanism is dominant. The experiment consists of measuring, using an integrating sphere, the photoluminesce spectra of samples with fixed doping levels of Ce^{3+} and Yb^{3+} while varying the thickness. This is presented in Section 4.3. Before proceeding we would like to theoretically analyse what the effect of self-absorption would be on the photoluminescence measurements using a simple optical model.

4.2 Modelling Self-Absorption Losses

A 1D optical model has been developed by the author of this thesis in order to describe the self-absorption of the emitted down-converted radiation. Consider a DC layer of length L divided into N slabs (see Fig. 4.7), where α and β are the absorption coefficients relative to the wavelengths of the pump and the emitted radiation, respectively. It is assumed that all the incident photons, which are absorbed by the donor ions, transfer their energy to two acceptors ions with an efficiency η_{ET}.

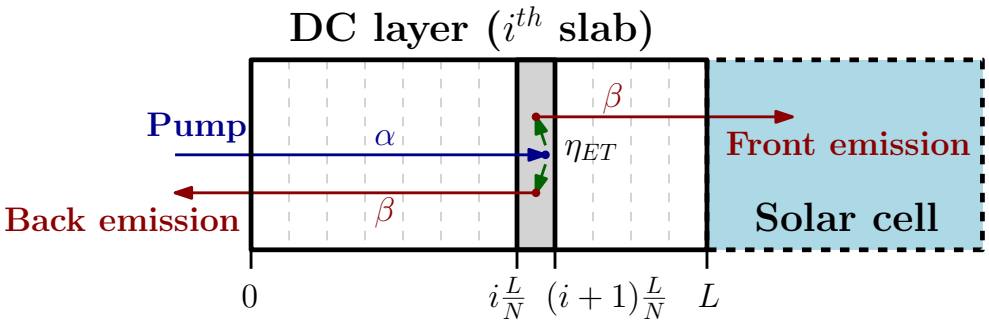

Figure 4.7: Schematic diagram of the 1D DC model scheme, showing an incident pump beam on the top surface. The solar cell is placed at length L, such that the DC layer is over-lying. α and β represent the absorption coefficient at pump and emission wavelength, respectively.

The emission is considered to be isotropic, thus statistically the emitted photons will be equally distributed between the front and back side. The probability for the emitted photons to exit from the material is then taken into account and depends on the number of slabs that the emitted photons have to pass through. The probability for an incident photon to be absorbed in the i^{th} slab is:

$$p_a^i(\alpha, L, N) = e^{-\alpha i \frac{L}{N}} - e^{-\alpha(i+1)\frac{L}{N}} = e^{-\alpha i \frac{L}{N}} \left(1 - e^{-\alpha \frac{L}{N}}\right) \tag{4.1}$$

The probability for an emitted photon (from the ith slab) to be transmitted outside the sample, such that it is not reabsorbed, in the case of front-emission is:

$$p_t^i(\beta, L, N) = e^{-\beta\left[L - \left(i+\frac{1}{2}\right)\frac{L}{N}\right]} = e^{-\beta L} e^{\beta\left(i+\frac{1}{2}\right)\frac{L}{N}} \tag{4.2}$$

The joint probability that a donor ion absorbs a photon in the ith slab, transferring its energy with an efficiency $\eta_{ET}(\alpha, \beta)$ to two acceptor ions in the same slab, and consequently emitting photons which have been transmitted outside the sample is then:

$$p_{TOT}^i(\alpha, \beta, L, N) = p_a^i(\alpha, L, N) \times \eta_{ET}(\alpha, \beta) \times p_t^i(\beta, L, N). \tag{4.3}$$

Finally, considering the contribution of all N slabs, the total probability for the emitted photons to be transmitted outside the sample has been calculated summing over the N slabs and taking the limit for $N \to \infty$:

$$\begin{aligned} p_{TOT}(\alpha, \beta, L, N) = \lim_{n\to\infty} \sum_{i=o}^{N-1} p_{TOT}^{i}(\alpha\beta, L, N) = \\ = \eta_{ET}(\alpha, \beta) \times e^{-\beta L} \times \lim_{n\to\infty} \left[\left(1 - e^{-\alpha \frac{L}{N}}\right) \times e^{-\frac{\beta L}{2N}} \times \sum_{i=o}^{N-1} e^{-(\alpha-\beta)\frac{L}{N} i} \right] \end{aligned} \tag{4.4}$$

Using the properties of geometric series and calculating the limit from De l'Hopital Rule, the following analytical formula is found:

$$p_{TOT-front}(\alpha, \beta, L) = \eta_{ET}(\alpha, \beta) \times e^{-\beta L} \times \left(1 - e^{-(\alpha-\beta)L}\right) \times \frac{\alpha}{\alpha - \beta} \tag{4.5}$$

and the special case where $\alpha = \beta$ yields the following particular solution:

$$p_{TOT-front}(\alpha, L) = \eta_{ET}(\alpha) \times \alpha L \times e^{-\alpha L}. \tag{4.6}$$

Thus, Eq. 4.6 represents the total probability for an incident photon to convert its energy with an efficiency $\eta_{ET}(\alpha, \beta)$ and escaping from the opposite side of the material of length L.

For the case of back-emission the formula changes to:

$$p_{TOT-back}(\alpha, \beta, L) = \eta_{ET}(\alpha, \beta) \times \left(1 - e^{-(\alpha-\beta)L}\right) \times \frac{\alpha}{\alpha + \beta}. \tag{4.7}$$

Finally, the two contributions can be combined to yield the total probability in the isotropic case, where $p_{TOT} = \frac{1}{2} p_{TOT-front} + \frac{1}{2} p_{TOT-back}$

$$p_{TOT}(\alpha,\beta,L) = \eta_{ET}(\alpha,\beta) \times \frac{\alpha}{2} \times \left[\frac{e^{-\beta L}\left(1 - e^{-(\alpha-\beta)L}\right)}{\alpha-\beta} + \frac{1 - e^{-(\alpha+\beta)L}}{\alpha+\beta} \right] \quad (4.8)$$

The probability $p_{TOT}(\alpha,\beta,L)$ could be related to the ePLQY of the process. Indeed, the incident photon flux ϕ_{inc} and the emitted photon flux ϕ_{em} are related to the probability $p_{TOT}(\alpha,\beta,L)$

$$\varphi_{inc} \times p_{TOT}(\alpha,\beta,L) = \varphi_{em} \quad (4.9)$$

while the ePLQY is defined as:

$$ePLQY = \frac{\varphi_{em}}{\varphi_{inc}}. \quad (4.10)$$

It follows that, in this case:

$$ePLQY = p_{TOT}(\alpha,\beta,L) \quad (4.11)$$

Thus, the optimal thickness ($L_{TOT-opt}$) of a DC layer that maximizes the total emission (front+rear) can be calculated setting the derivative of Eq. 4.8 equal to zero:

$$\frac{e^{-\beta L}\left(1 - e^{-(\alpha-\beta)L}\right)}{\alpha-\beta} + \frac{1 - e^{-(\alpha+\beta)L}}{\alpha+\beta} = 0 \quad (4.12)$$

Although this equation does not have an analytical solution, the optimal thickness ($L_{TOT-opt}$) can be readily obtained by plotting the function once the experimental absorption coefficients (α,β) have been substituted. The thickness that maximizes the emission at the front of the DC layer ($L_{front-opt}$) - the expression

most relevant for PV systems - can then be calculated as follows:

$$0 = \frac{\partial}{\partial L} p_{TOT-front}(\alpha, \beta, L) = constant \times e^{-\beta L} \times \left(\alpha e^{-(\alpha-\beta)L} + \beta\right) \tag{4.13}$$

Whose solution could be easily derived as:

$$L_{front-opt} = \frac{\ln\left(\frac{\alpha}{\beta}\right)}{\alpha - \beta} \tag{4.14}$$

For the special case with $\alpha = \beta$, the optimal thickness could be derived from the derivative of Eq. 4.8:

$$L_{front-opt} = \frac{1}{\alpha} \tag{4.15}$$

This result could be used to evaluate the thickness of the sample in order to minimize the losses due to self-absorption in the case of DC-PV device application. It has also to be considered that we have not taken into account that portion of back-emitted radiation that it is reflected due to the total internal reflection, as it happens for a real case.

Figure 4.8 plots Eq. 4.5, Eq. 4.7 and Eq. 4.8 for a specific case with η_{ET}=100% and both α and β fixed to two specific values, that have been chosen from experimental data measured on the samples used in Section 4.1.2.

According to Fig. 4.8, the ePLQY calculated from the back emission (dashed line) saturates to a limit of 83.5%, corresponding to $\alpha(\alpha + \beta)^{-1}$, as the thickness increases. On the other hand it can be observed that in the case of the front emission (dash-dotline), that an optimal thickness exists that maximizes the ePLQY to 67%, and this will obviously affect also the trend of the total emission (solid line), whose maximum ePLQY reaches 143.2%. It is remarkable that the optimal thickness

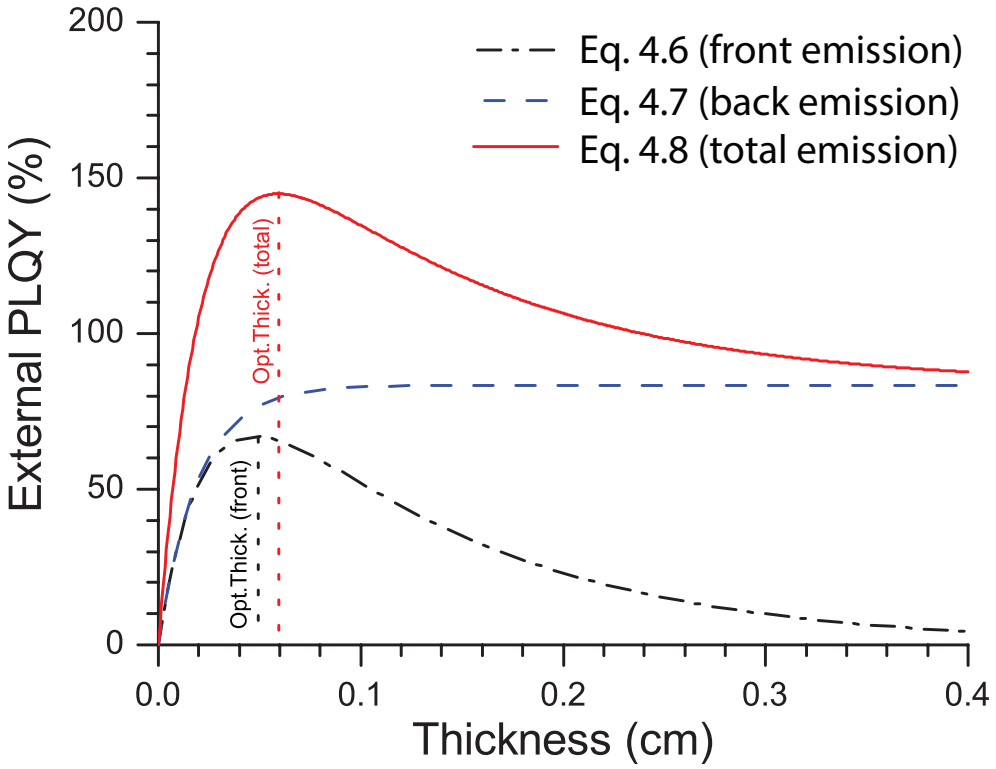

Figure 4.8: ePLQY calculated for a specific case with α=42.4 cm^{-1} and β=8.4 cm^{-1} for front emission (dash-dotline), back emission (dashed line) and the total contribution (solid line).

that maximizes the ePLQY is smaller for the front emission than for the total emission, which has to be considered depending on the application. The predicted values have been calculated considering an ideal case of η_{ET}=100%, which should correspond to an ePLQY of 200%. The value of 143.2% is instead much lower with respect to the ideal 200% value. This means that the self-absorption of the emitted radiation is an effect that should be taken into account when we discuss measured photoluminescence spectra.

4.3 Experimental Validation Using Ce^{3+}/Yb^{3+} Borate Glasses

In order to isolate the contribution from self-absorption, samples of varying thicknesses were prepared for a fixed concentration of Ce^{3+} (1%mol) and Yb^{3+} (1%mol) ions. The photoluminescence spectra were measured exciting at 305 nm (FWHM=12 nm) using the calibrated integrating sphere, in order to be able to compare the absolute values of the measured photoluminescence intensity.

From Fig. 4.9, it is observed that as the thickness decreases the absolute emission peak at 978 nm increases in intensity. Moreover, the total integrated emission shows that an optimal thickness exists that maximize the emitted fluorescence, i.e. the total counts, and it was measured to be 0.84±0.01 mm.

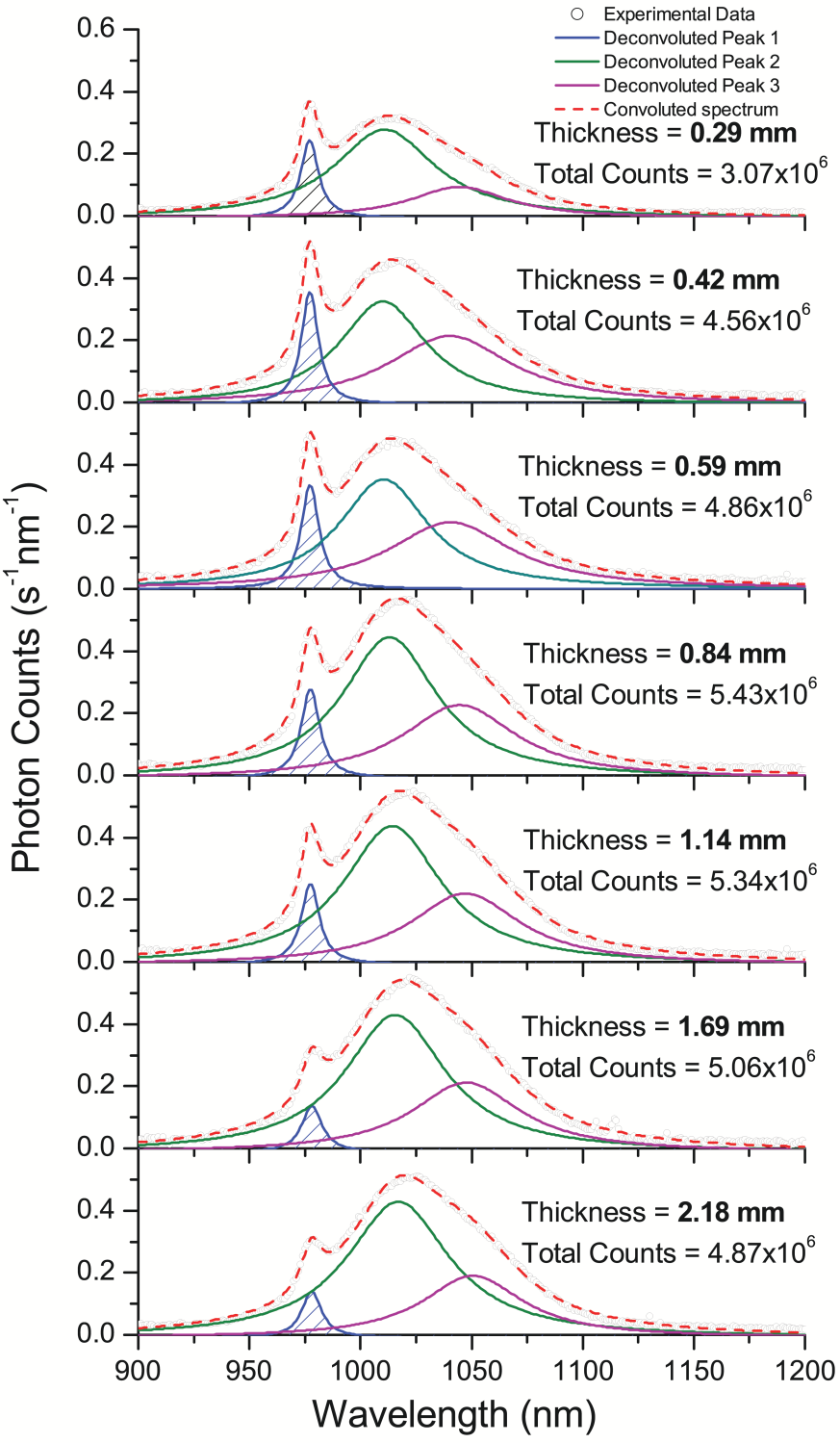

Figure 4.9: Emission spectra for Ce^{3+} 0.5 %mol -Yb^{3+} 1%mol at varying thicknesses. The total photon counts are displayed for each case and the emission peak at 978 nm is highlighted through the shaded area.

A multipeak fit on the measurements were performed in order extrapolate the emission peak intensity at 978 nm. The data, as shown in Fig. 4.9, were then fitted using Eq. 4.8, since the integrating sphere collects both the radiation coming from the front and back side of the sample. The fit was initialized fixing β=8.44 cm^{-1} (measured absorption coefficient at 978 nm), and we compared the estimated parameter absorption coefficient at 305 nm with the measured one. The parameter α has been estimated to a value of 46±10 cm^{-1} which is the same (within the margin of error) to the measured value of 42.4 cm^{-1} affording strong evidence that the measured samples are affected by the self-absorption of emitted radiation.

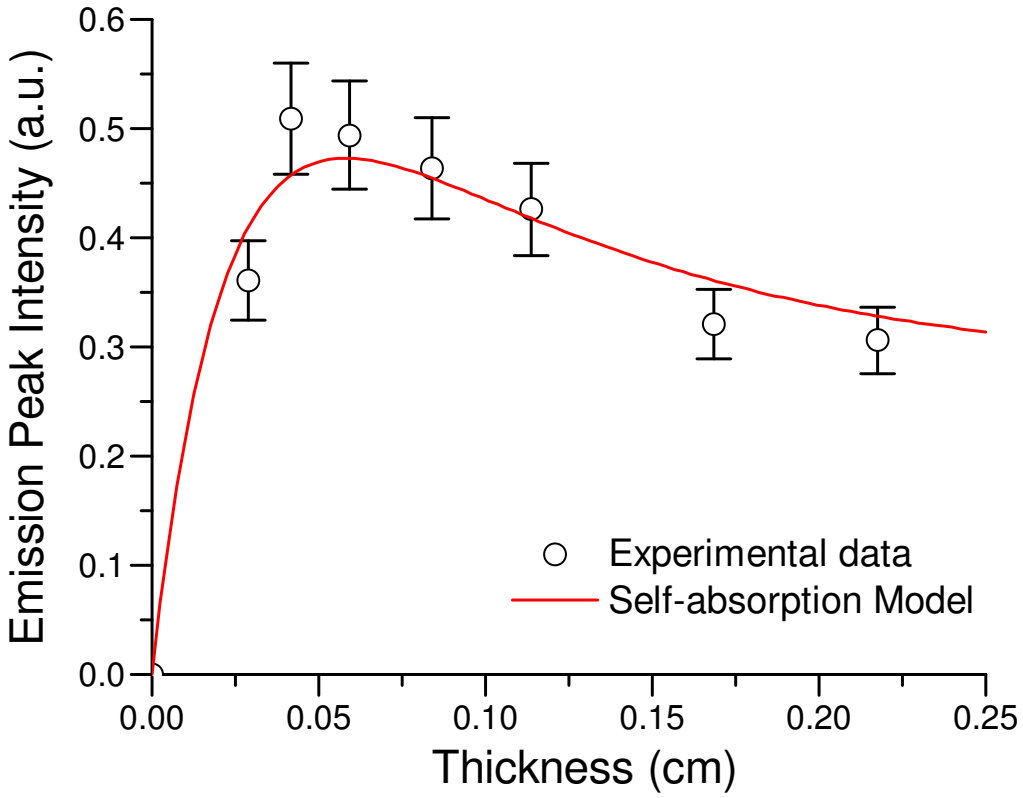

Figure 4.10: Integrated fluorescence relative to the peak at 978nm fitted by Eq. (8) calculated from the self-absorption model.

4.4 Conclusions

In summary, we have presented a study with the aim of minimise the losses within luminescent materials coming from self-absorption of the emitted radiation. Application of DC materials to solar cells represents a challenging area. The inability to demonstrate a DC-PV device is due to the fact that the intrinsic losses happening in a DC material compete against the DC process itself. In this work the losses coming from the self-absorption of the emitted radiation were analysed using a specifically-developed 1D optical model.

The experimental results showed that an optimal thickness and an optimal doping concentration of the ions participating in the DC process exist in order to minimize the self-absorption and enhance the PLQY of the material. The validation through experimental measurements on DC borate glasses co-doped with Ce^{3+}/Yb^{3+} demonstrates the consistency of this model, which could be also applied to other spectral conversion systems, such as those based on luminescent downshifting and upconverting materials, but also for other technologies involving luminescent materials containing high absorbers dopant such as Yb^{3+} ions.

In conclusion, I have provided a method to reduce the self-absorption loss mechanism, which can be applied to a wider class of luminescent materials. The equations given by the model presented in this Chapter will be analysed in Chapter 5, and the model will be adapted also for a upconverter system.

Finally, in chapter 6 we will use those results to optimise an upconverter material made of BaY_2F_8 doped with Er^{3+} ions.

Chapter 5

Role of Self-absorption on Downconversion and Upconversion Enhanced PV devices

This chapter discusses the impact of self-absorption on absolute photoluminescence quantum yield analysis and on DC and UC enhanced PV devices. Specifically, this chapter shows how the self-absorption loss mechanism depends strongly on the experimental conditions used to measure the photoluminescence properties.

This chapter expands on material from the following publications:

Boccolini A., Marques-Hueso J., Chen D., Wang Y., and Richards B. S. "Physical performance limitations of luminescent down-conversion layers for photovoltaic applications."
Solar Energy Materials and Solar Cells, Vol. 122, (2014).

Boccolini A., Marques-Hueso J., and Richards B. S. "Self-absorption in upconverter luminescent layers: impact on quantum yield measurements and on designing optimized photovoltaic devices."
Optics Letters, Vol. 39, Issue 10 (2014).

5.1 Impact of Self-Absorption Losses on DC-PV Devices

The self-absorption model presented in the previous chapter allow us to extend the analysis by determining the limitations of a DC-PV device due to sole contribution of this optical loss mechanism. Eq. 4.8, representing the total emission escaping from the sample, is subjected to a thickness optimisation which determines a maximum ePLQY.

The maximum ePLQY value is strictly connected with the values of both α (absorption coefficient at excitation wavelength) and β (absorption coefficient at emission wavelength), which are also related to the concentration of the donor and acceptor ions in the DC material, respectively. By varying those parameters, together with the energy transfer efficiency η_{ET} we can determine the upper limit of the DC-PV device due to the self-absorption loss mechanism.

Fig. 5.1(a)(c) displays, for an ideal case of a fixed η_{ET}=100% (corresponding to an iPLQY of 200%), the maximum achievable ePLQY by varying parameters α and β and the dependence of the ePLQY with the thickness and β for α=42.4 cm^{-1} shows that in order to increase the probability of the DC process we should decrease β as low as possible and increase α. The optimal thickness which yields an ePLQY of 199.9% is found around 1.61 mm, corresponding to absorption at the pump wavelength of 99.999%, or an optical density (OD) of 5.

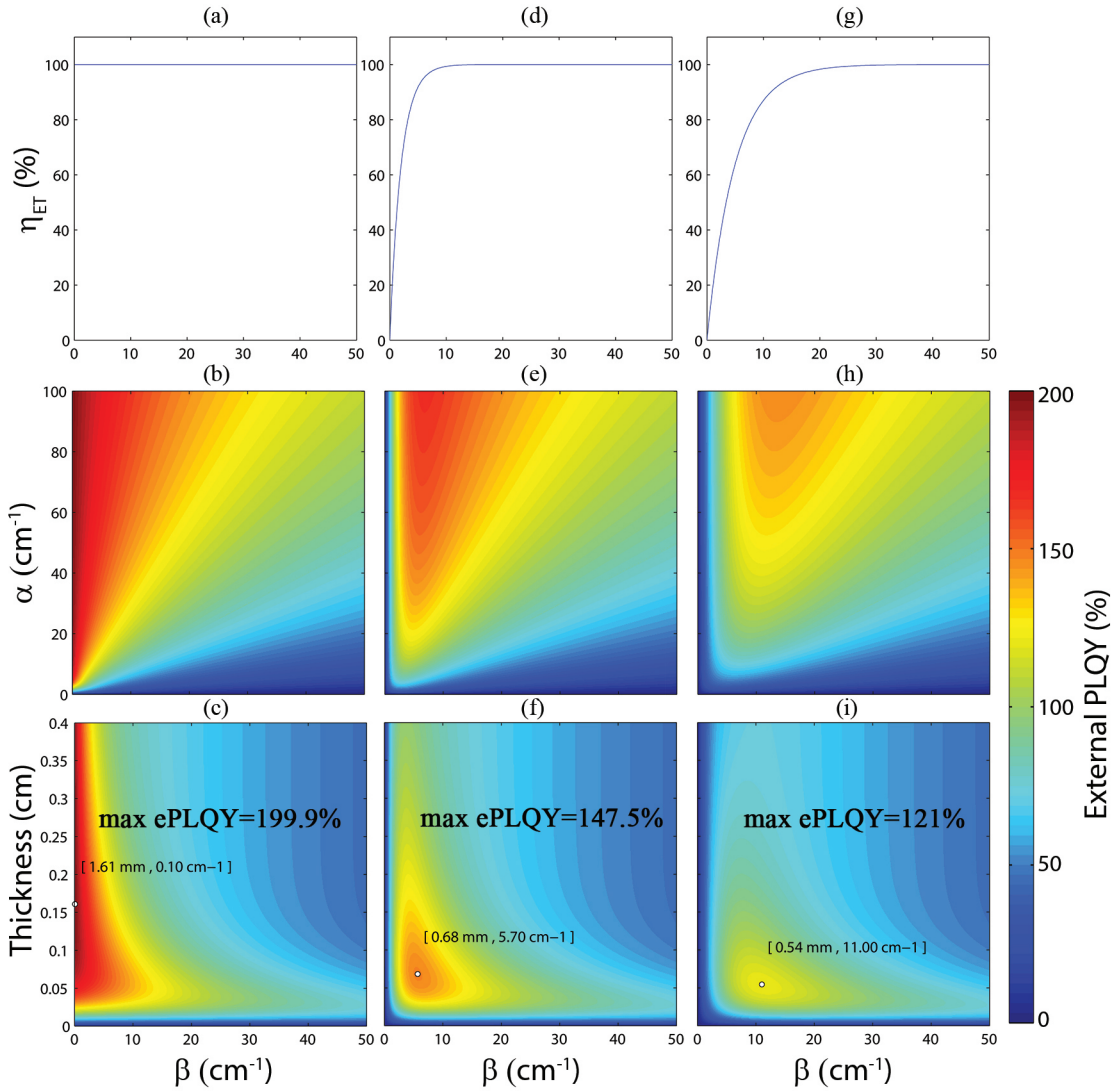

Figure 5.1: ePLQY dependence on thickness and doping concentration. Graphs (a), (d) and (g) represent three different η_{ET} dependence curves on β. Graph (b), (e) and (h) show the ePLQY vs. α and β. Graphs (c), (f) and (i) displays the ePLQY vs. Thickness and β with α fixed to 42.4 cm^1 together with the optimal point corresponding to the max ePLQY.

In reality, these two requirements could not be satisfied because a low value for β corresponds to a low Yb^{3+} concentration, which in turn decreases the probability of energy transfer and subsequently results in a poor probability of DC taking place. Indeed, if we consider a more reliable case of η_{ET} reaching 100% gradually only after a certain amount of Yb^{3+} (see both Figs. 5.1(g) and 5.1(h)), the plotted solutions of Eq. 4.8 yield more interesting results. Graph (d) in Fig. 5.1 confirms that greater ePLQY corresponds to greater α values, but in this case an optimal β exists that maximizes the performance of the DC material. Indeed, graphs 5.1(e) and

5.1(f) shows that an optimal thickness of 0.68 mm (corresponding to about 94.4% of absorption or OD=1.25 at pump wavelength) and an optimal β=5.70 cm^{-1} leads to a maximum ePLQY of 147.5%.

The behaviour described in Fig. 5.1(g)-(i) is quite similar to the previous case. In this scenario, the η_{ET} increases slower with β than previously and the optimal β results in a range of higher values (because of the lower efficiency of the transfer). For α=42.4 cm^{-1} the optimal thickness is 0.54 mm (89.9% of absorption of incident photons, or OD=0.99) and β=11 cm^{-1}, while the maximum ePLQY is 121%.

The maximum ePLQY presented so far could also be lowered by the other quenching phenomena, such as radiation trapping or cross-relaxation. Therefore, the limit values represent an ideal case in which the self-absorption is the competitive mechanism which decreases the luminescence intensity.

5.2 Impact of Self-Absorption Losses on UC-PV Devices

An UC-PV device consists of coupling an UC layer to the rear side of a bifacial solar cell, so that the UC layer absorbs the transmitted sunlight and emits photons back into the overlying solar cell with energy greater or equal to the semiconductor bandgap E_{gap} [11, 56].

The effective gain that could be obtained from a UC-PV device is dependent on the optical quantum yield of the UC layer. The experimental evaluation of the quantum yield through photoluminescence measurements is of primary importance to estimate the potential applicability of the UC materials [91].

By definition, the maximum theoretical achievable iPLQY for an UC process is 50%, which is difficult to achieve experimentally. The short-fall between the theoretical limit and the measured values is caused by several factors including non-radiative losses like multiphonon relaxation, concentration quenching and self-absorption [81, 92, 93]. Additionally, the ePLQY is also constrained by the ab-

sorbance of the UC material, whose optical performances may be considerably lowered if a weak absorption cross section at the pump wavelength is present. Losses caused by concentration quenching and multiphonon relaxation can be minimized by optimizing the presence of dopant ions and choosing low phonon energy hosts, such as fluorides, bromides and chlorides [94]. Losses caused by self-absorption instead have been only marginally investigated.

Occurrence of self-absorption is associated with the overlapping of emission and absorption spectra of the RE^{3+} ions involved. The overlap can be quite large in RE^{3+} ions due to their atomic-like spectra. Recently, a self-absorption loss mechanism has been reported in erbium(Er^{3+})-doped barium yttrium fluoride (BaY_2F_8) where it has been minimized by experimentally optimizing the thickness of the sample [95]. Moreover, an optical model describing how the self-absorption affects PLQY measurements in a downconverter (DC) luminescent material has been demonstrated in [93].

Here we develop an optical model for UC where the self-absorption losses and the non-linear power dependence of the UC process are considered. In this way, the optimal thickness of an UC layer, which reduces the effect of the self-absorption and maximizes the ePLQY, can be calculated for a determined incident power and dopant concentration. Moreover, we demonstrate that the ePLQY of an UC layer, measurable through an integrating sphere, may be underestimated with respect to the actual ePLQY while performing in a UC-PV device configuration. Finally, we will show that the optimal thickness is inversely proportional to the molar concentration of the Er^{3+} ions, and that this is equivalent to a condition of having a fixed number of ions within the material that minimize the self-absorption.

A similar methodology implemented by the authors to model the self-absorption in a down-conversion (DC) layer [93] has been used here. It consists of dividing the considered sample in N slabs along the thickness L. For each slab, the probability of absorbing the incident pump (p_a^i), the energy transfer efficiency (η_{ET}) of the process along L, and the probability of the emitted radiation to escape out through the front

and back sides of the sample (p_t^i), have been combined in order to obtain the total ePLQY of the layer as a sum of the contributions of the N slabs. In a DC system, there is a linear dependence on DC emission with incident pump power, hence it was possible in [93] to analytically solve the relevant equation to predict the ePLQY.

In the UC system considered, since a non-linear relationship between the excitation power (P) and UC luminescence exists [96], and because of the exponential decrease of the pump beam intensity along L, the probability for an UC photon to be emitted from each slab varies along the sample thickness. This probability is related to the measurable iPLQY of the sample. Therefore, in the equations used for the modelling, the η_{ET} has been replaced with experimental iPLQY data from literature and the total contribution has been numerically computed.

$$ePLQY = \sum_{i=1}^{N} \left[p_a^{(i)}(L) \cdot iPLQY(P,i) \cdot p_t^{(i)}(L) \right] \tag{5.1}$$

Since the focus of this work is to compare the relative optical performance of two different experimental situations, the effect of scattering - which can also affect the self-absorption - has not been accounted for within this model. Therefore the propagating beams inside the sample have been considered scattering-free.

The iPLQY power dependent measurements have been taken from [97], where hexagonal sodium yttrium fluoride (β-$NaYF_4$) micro-phosphors embedded with 55.6 w/w% in a perfluorocyclobutane host matrix at seven different Er^{3+} doping concentrations (10 mol.%, 15 mol.%, 20 mol.%, 25 mol.%, 35 mol.%, 50 mol.% and 75 mol.%) have been analysed. This particular polymeric host matches the refractive index of β-$NaYF_4$ so that scattering effects within the samples were minimized.

A semi-empirical function, representing the iPLQY power dependence, has been fitted to the experimental data in order to obtain a continuous set of data for each power density:

$$iPLQY = \frac{A \cdot P_{in}}{1 + B \cdot P_{in}}, \tag{5.2}$$

A and B are parameters estimated from the fit. Eq.5.2 originates from experimental

observations. In fact, the iPLQY, defined by the ratio of the power dependent UC emission intensity ($I_{UC}(P)$) by the absorbed power P, results in a power dependence proportional to P^{m-1} with $m-1$ taking values from 1 (low power regime) to 0 (high power regime). This is due to the fact that experimentally $I_{UC}(P)$ is proportional to P^m (with m=2 in the ideal case of 2-photon UC), while a linear dependence is established in the high power regime [98].

The fit of Eq.5.2 to the experimental data is given in Fig.5.2a for power densities between 0 and 10^3 Wm^{-2} (relative to an incident radiation of wavelength 1523 nm), and demonstrates excellent agreement.

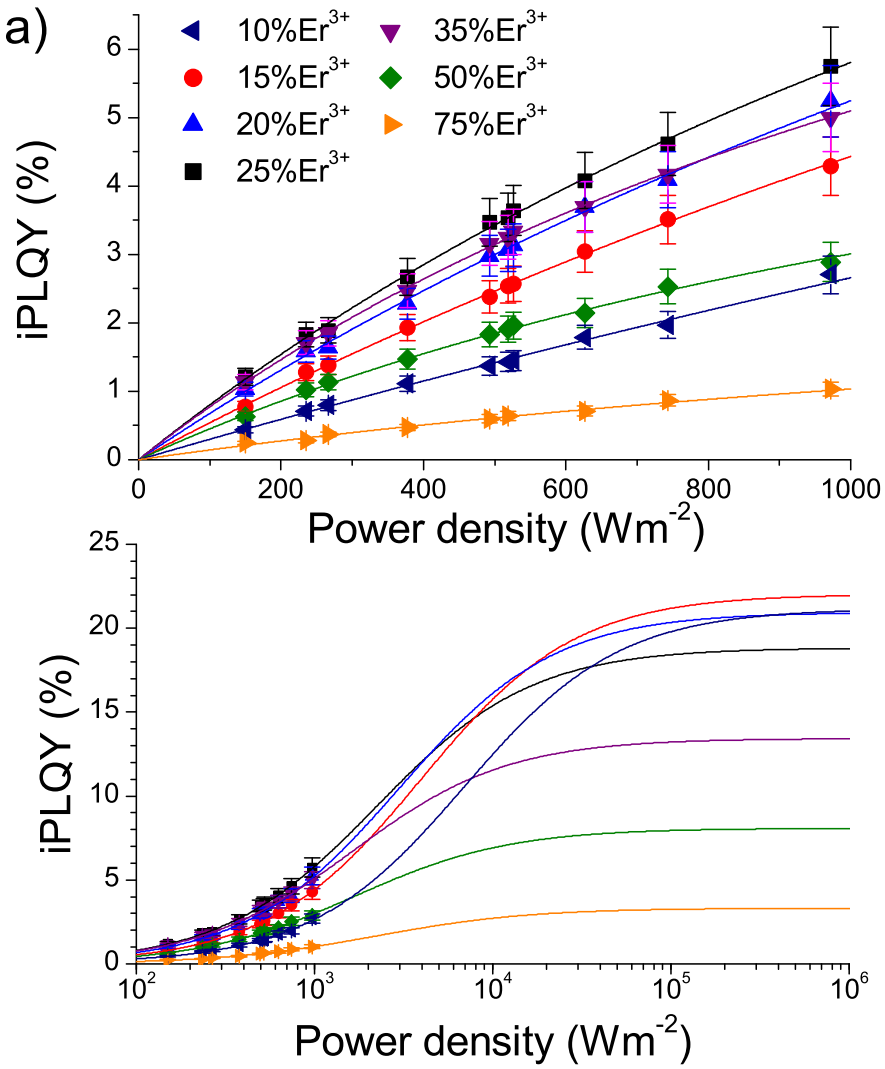

Figure 5.2: iPLQY data taken from [97] plotted together with the fitted curves defined by Eq.5.2 for each Er^{3+} molar concentration: (a) shows the accuracy of the fit for pump power densities up to 10^3 Wm^{-2}, while (b) shows the extrapolated values up to 10^6 Wm^{-2}.

Table 5.1: Fitted parameters A and B from data in [97] and iPLQY values with their corresponding log-log slope at different power densities (150 Wm^{-2}, 970 Wm^{-2} and 10^6 Wm^{-2}) for different Er^{3+} doping levels.

Er^{3+} (mol.%)	A (cm^2W^{-1})	B (cm^2W^{-1})	iPLQY at 150 Wm^{-2}	iPLQY at 970 Wm^{-2}	Slope (*m-1*) at 150 Wm^{-2}	Slope (*m-1*) at 970 Wm^{-2}	iPLQY at 10^6 Wm^{-2}
10	0.30±0.01	1.4±0.4	(0.4±0.2)%	(2.6±0.9)%	1.0±0.3	0.9±0.3	(21±7)%
15	0.56±0.01	2.5±0.3	(0.8±0.1)%	(4.4±0.7)%	1.0±0.1	0.8±0.1	(22±3)%
20	0.70±0.01	3.3±0.5	(1.0±0.2)%	(5.1±0.9)%	1.0±0.2	0.8±0.1	(21±4)%
25	0.84±0.02	4.5±0.5	(1.2±0.2)%	(5.7±0.8)%	0.9±0.1	0.7±0.1	(19±3)%
30	0.82±0.01	6.1±0.3	(1.1±0.1)%	(5.0±0.3)%	0.9±0.1	0.6±0.1	(13±1)%
50	0.48±0.01	5.9±0.6	(0.7±0.1)%	(3.0±0.4)%	0.9±0.1	0.6±0.1	(8±1)%
75	0.15±0.01	4.5±1.7	(0.2±0.1)%	(1.0±0.5)%	0.9±0.4	0.7±0.3	(3±2)%

Moreover, the fitted curves have been extrapolated to higher power regimes, as shown in Fig.5.2b, where the iPLQY for each case reach asymptotically its limit. The parameters A and B, the corresponding slope in a log-log plot for two different power density and the resulting iPLQY values for each Er^{3+} doping level are summarized in Table 5.1. The obtained log-log slopes are in the range of 0.9-1.0 at 150 Wm^{-2} and 0.6-0.9 at 950 Wm^{-2}, which confirm the transition described in Eq.5.2 from low to high power regime dependence.

The integrated irradiance of the air-mass direct solar spectrum in correspondence of Er^{3+} absorption band in β-$NaYF_4$ (1480-1560 nm) has been calculated to be 23 Wm^{-2}. It follows that values of 10^4 Wm^{-2} correspond to a concentration factor of about 400-500x, that could be reached in a real system with a concentrating PV (CPV) technology [99]. Instead power densities up to 10^6 Wm^{-2} (100x increase respect to CPV) might be achievable if other technologies based on nanophotonic and plasmonic enhancement are considered [100].

Interestingly, the extrapolated data coming from the fit of Eq.5.2 - which does not predict a decrease in quantum yield as expected in a real situation [96]- shows that the highest value obtained (around 22%) is far below the theoretical 50%. This shows how challenging it is achieving high quantum yield values with UC materials.

Based on previous analysis, two different cases have been simulated. One case relates to the ePLQY that would be measured with an integrating sphere, while the other scenario is likened to the effective ePLQY of the UC material when coupled to a solar cell in a UC-PV device (see Fig.5.3). In the latter case, due to the reflector, the power density in each slab is given by the superposition of direct and reflected

pump beams.

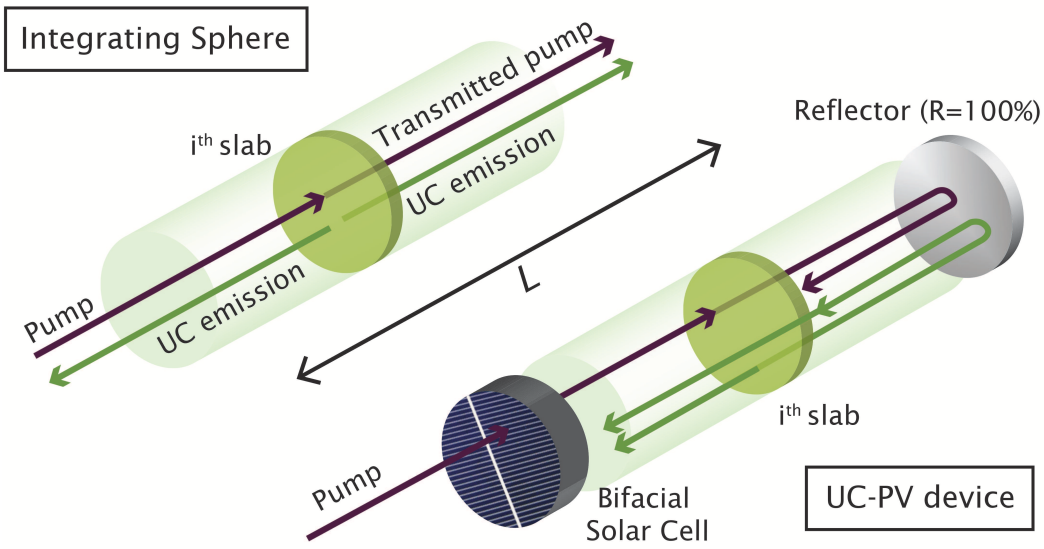

Figure 5.3: UC emission in two different experimental situations. In the first case, the UC sample is excited by a collimated pump beam inside an integrating sphere (not shown for clarity) which collects the UC luminescence coming out from both front and back side. In the second case, the emission is considered when attached on the back side of a bifacial solar cell and a 100% reflector covering the other side of the UC layer.

The graph in Fig.5.4 shows the calculated ePLQY in the two different configurations and for three different power regimes (10^3, 10^4 and 10^5 Wm^{-2} of 1523nm light) relative to the 25% Er^{3+} sample, which is among the highest iPLQY values reported in Fig.5.2. In both configurations, the ePLQY is maximum for a certain optimal thickness, whose value differs from case to case. This is due to the presence of the reflector in the UC-PV device, which allows recycling the transmitted pump. Consequently, the optimal thickness is reduced and at the same time a higher power density within the sample is established. This explains why in Fig.5.4 the maximum ePLQY that could be achieved in a UC-PV device is higher than an ePLQY that could be measured with an integrating sphere. Furthermore it follows that, for samples thicker than the optimal values, the ePLQY in a UC-PV device could be lower with respect to the integrating sphere scenario.

In fact, for the device case, the recycled UC emission due to the reflector suffers a longer pathlength before reaching the back side of the solar cell, and thus the probability to be reabsorbed increases.

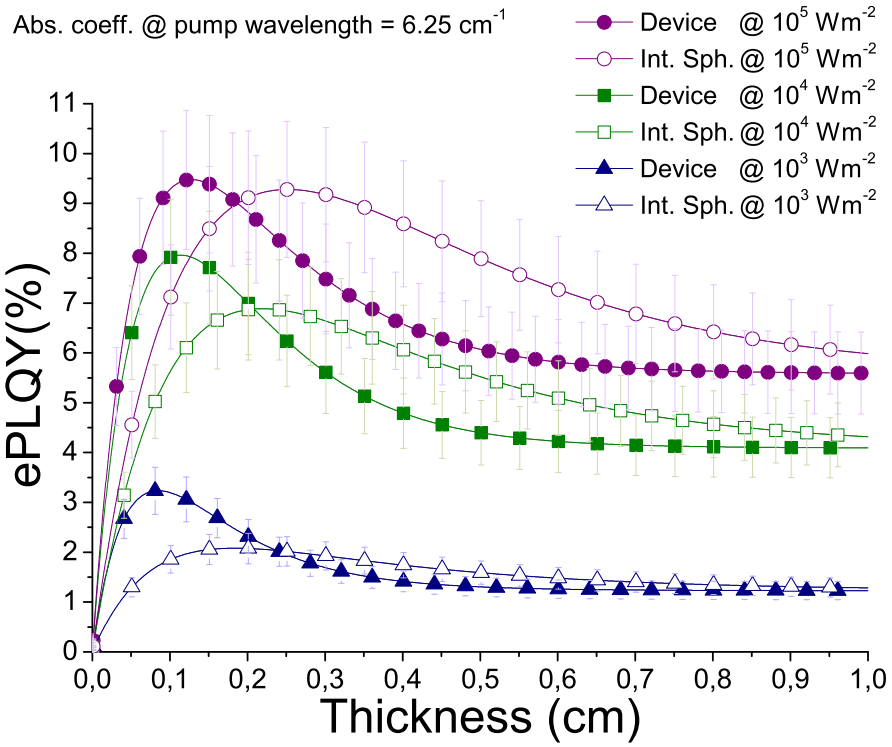

Figure 5.4: Simulated ePLQY using Eq.5.1 for the $NaYF_4$:Er^{3+}(25%) as a function of thickness, for three different pump power densities in the two configurations described in Fig.5.3.

For all the different Er^{3+} concentrations the maximum ePLQY value achievable in both configurations and its corresponding optimal thickness have been extrapolated. The data are reported in the graphs of Fig.5.5 and they are relative to a fixed power density of 10^3 Wm^{-2}.

In Fig.5.5a the concentration dependence of maximum ePLQY confirms that for this specific pump regime the optimal concentration of Er^{3+} is equal to 25% and that the performance of the UC material within the UC-PV device could be higher by a factor of 1.5. The graph displaying the concentration dependence of the optimal thickness has been fit, for both configurations, with a function of the type: $y = k \cdot x^{-1}$, where k is a constant. The k values calculated from the fit are $2.0{\cdot}10^{-4}$ mol cm^{-2} and $4.5{\cdot}10^{-4}$ mol cm^{-2} for the UC-PV device case and integrating sphere setup, respectively. Assuming a beam size $S = 10.5{\cdot}10^{-4}$ cm^2 [97], the product $S \cdot k$ represents the volume of the pump beam per mol of Er^{3+} ions excited.

Finally, then multiplying Avogadro's number N_A, the number of Er^{3+} ions present within the excitation volume is obtained. Values of $1.3{\cdot}10^{17}$ ions for the UC-

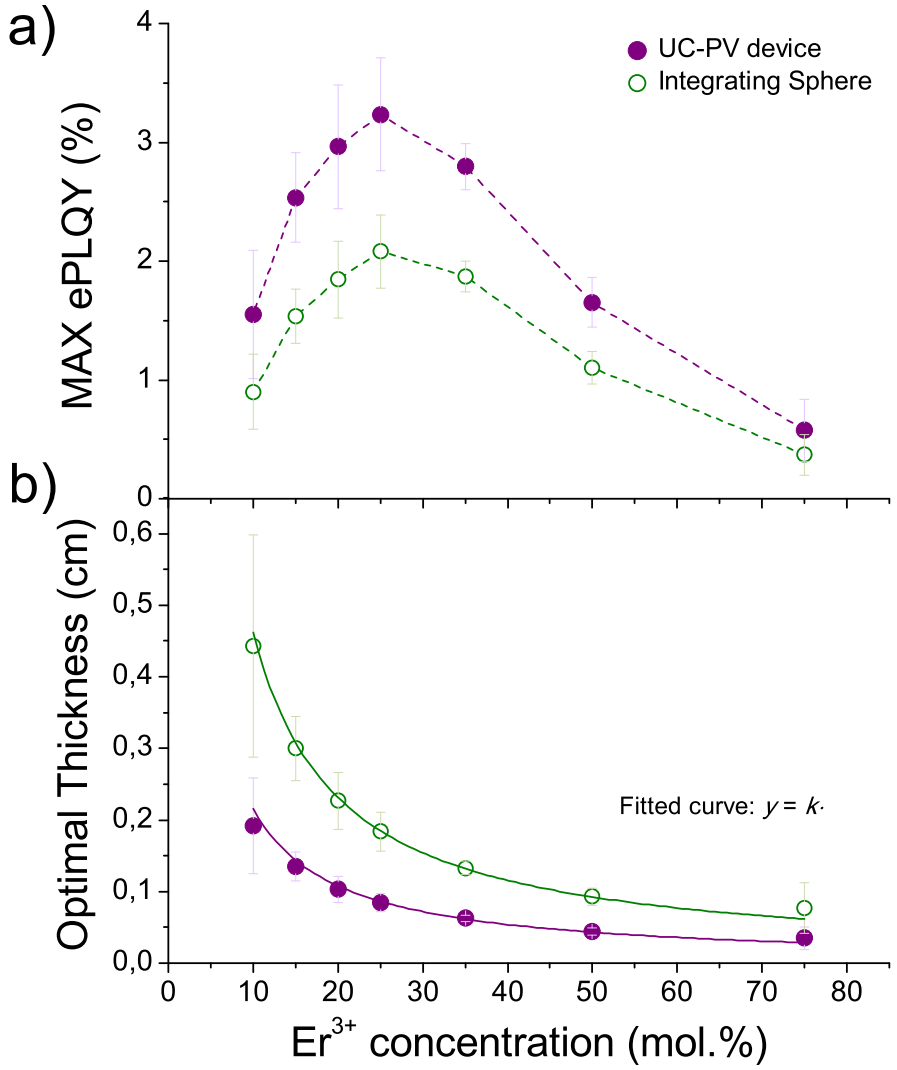

Figure 5.5: Maximum ePLQY achievable (a) and its corresponding optimal thickness (b) dependence with Er^{3+} molar concentration referring to 10^3 Wm^{-2} pump power density in the two different configurations.

PV device configuration and $2.9{\cdot}10^{17}$ ions for the integrating sphere setup. Therefore, the condition to minimize the impact of self-absorption is actually translating in finding a specific amount of Er^{3+} ions present in the excited volume within the sample. In our compared analysis the number of Er^{3+} ions needed to minimize the self-absorption is lower in the case of a UC-PV because of its optimized design.

5.3 Conclusions

To summarize, in the case of DC-PV device analyisis, by minimizing the losses coming from the self-absorption, the ePLQY value could be maximized by selecting

the right values of the three parameters α, β and thickness. The choice of the thickness is very crucial because we have to choose a thickness that would appear at first to be counter-intuitive, as it corresponds to a non-optimal absorption of the pump (less than 100%).

In the case fo UC-PV device, we have quantified the impact of self-absorption on the ePLQY for an UC system. The results showed that an optimal sample thickness is required to maximize the ePLQY. Two different cases have been compared; the first in which the ePLQY of the material is measured in a integrating sphere and the second in which the effective ePLQY of a UC layer attached to the back side of a bifacial solar cell is considered. From the comparison it follows that, under optimal operating conditions, the ePLQY measured through an integrating sphere may result in an underestimation with respect to the performance that the UC material could achieve in a UC-PV device.

Moreover it has been found that the optimal thickness and the ions' molar concentration are inversely proportional, suggesting that the condition on the optimal working condition can be translated to an optimal number of Er^{3+} ions present within the volume excited by the incident pump beam. Finally, self-absorption is not only restricted to RE^{3+}-based materials. UC systems using organic molecules and non-PV applications based on spectral conversion may also be affected by this loss mechanism [101, 102].

Chapter 6

Highly Efficient Upconversion in Er^{3+} Doped BaY_2F_8 Crystals

This chapter presents a study of the upconversion (UC) in barium yttrium fluoride (BaY_2F_8) single crystal doped with trivalent erbium ions (Er^{3+}) under excitation of the $^4I_{13/2}$ level at three different wavelengths: 1493 nm, 1524 nm and 1556 nm. The resulting UC emission at around 980 nm has been investigated and it has been found that a thickness optimization is required to reach high quantum yield values, otherwise limited by self-absorption losses. The iPLQY and ePLQY values reported in this chapter are among the highest achieved for monochromatic excitation. Finally, the losses due to self-absorption were estimated in order to evaluate the maximum iPLQY achievable by the upconverter material.

This chapter expands on material from the following publications:

Boccolini A., Favilla E., Tonelli M., Richards B. S, and Thomson R. R.. "Highly efficient upconversion in Er^{3+} doped BaY_2F_8 single crystals: dependence of quantum yield on excitation wavelength and thickness."

Optics Express, Vol. 23, Issue 15 (2015).

6.1 Upconverters Based on Erbium Doped Materials

6.1.1 State of the Art

Photon UC in trivalent erbium (Er^{3+}) ion-doped materials is a striking feature for a number of technological applications, such as solid state lasers [103], optical amplifiers [104], light-emitting displays [105], biolabels [106] and PV [107]. This wide range of applications originates from the UC property of absorbing two photons and emitting one higher energy photon due to energy transfer between the excited Er^{3+} ions [47, 108].

Figure 6.1 shows the typical design of a Er^{3+}-based UC-PV device in which IR sub-bandgap photons with wavelength at around 1500 nm (∼0.8 eV) are absorbed and converted by an UC layer underneath a bifacial solar cell. The UC process populates the $^4I_{9/2}$ level, which relaxes to the lower $^4I_{11/2}$ level. Due to the transition $^4I_{11/2} \rightarrow {}^4I_{15/2}$, the resulting emission at around 980 nm (∼1.2 eV) is finally absorbed and converted into electricity by the silicon solar cell (bandgap energy ∼1.1 eV).

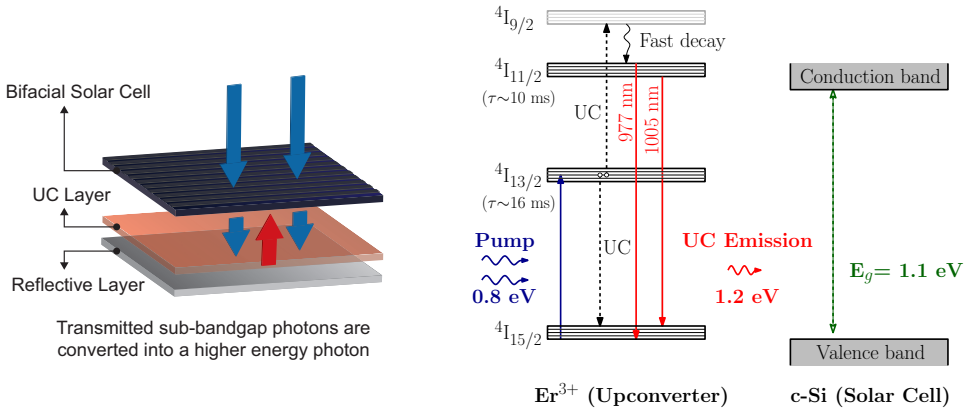

Figure 6.1: Two sub-bandgap photons are converted into a higher energy photon by an UC layer placed underneath a bifacial solar cell. The pump energy scheme within Er^{3+} ions of the $^4I_{13/2}$ level shows how the UC process populates the $^4I_{9/2}$ level and consequently to the lower $^4I_{11/2}$ due to fast decay. The radiative decay to the ground state from this level leads to an emission characterized by two main peaks centered at 977 nm and 1005 nm, corresponding to photon energies just above the silicon bandgap E_g. The lifetimes values reported have been measured in our lab.

The idea to utilize UC for PV applications was initially given, in 1996, by Gibart

et al. testing in the IR region (≃1.39 eV) a device made of a GaAs solar cell (E_{gap}=1.43 eV) with a co-doped Yb^{3+}-Er^{3+} vitroceramic [109]. Shalav *et al.* first proposed the use of $NaYF_4$:20%Er^{3+} upconverting phosphor coupled with a silicon solar cell, measuring an EQE of 2.5% under monochromatic excitation at 1523 nm [110]. Later, authors from the same group, tested the same material using a better optical coupling, and an EQE of 3.4% was reached under 2.4 Wcm^{-2} illumination at 1523 nm [111]. In 2010 others EQE measurements involving c-Si solar cell were performed with NaY_4F doped with Er^{3+} by Fischer *et al.* obtaining EQE values of 0.34% (under 1880 Wm^{-2} at 1523 nm) [112]. In 2011 Pellè *et al.* using CaF_2-YF_3 found an EQE of 2.4% under 100 Wcm^{-2}) with excitation at 1540 nm [113].

As mentioned in Section 2.4.1.2 theoretical studies based on a detailed-balance approach have predicted that an ideal Er^{3+}-based UC-PV device could reach up to 7% relative increase with respect to the efficiency of a silicon solar cell, which in terms of absolute efficiency corresponds to an increase from 25.95% to 27.88% under non concentrated sunlight and from 36.61 % to 39.43 % at aconcentration of 46200 suns [57]. The concept of ideal UC refers to a system which totally absorbs the exciting radiation and converts exactly two photons into one higher energy photon. Therefore an ideal UC corresponds to a system absorbing 100% of the incident radiation and having an internal photoluminescence quantum yield (iPLQY) of 50%, or equivalently to a system showing an external photoluminescence quantum yield (ePLQY) of 50%. Where ePLQY and iPLQY are defined as the ratio of incident (or absorbed) photons over the emitted ones, respectively.

Experimentally, the highest iPLQY of 12±1 % (ePLQY∼5.5%) was reported by Martin-Rodriguez *et al.* in a gadolinium oxysulfide host (Gd_2O_2S:10%Er^{3+}) under monochromatic excitation at 1500 nm with an irradiance of 0.07 Wcm^{-2} [114]. Fischer *et al.* reached the highest ePLQY value of 9.5±0.7 (iPLQY= 10.1±1.6 %) for monochromatic excitation at 1520 nm with an irradiance of 0.47±0.25 Wcm^{-2} employing a BaY_2F_8:30% Er^{3+} doped upconverter [115]. Under broadband excitation the highest iPLQY of 16.2±0.5 % (ePLQY = 3.4±0.1 %) was reported by

MacDougall *et al.* in a sodium yttrium fluoride (β-$NaYF_4$: 10% Er^{3+}) UC material centered at 1523 nm, 80 nm bandwidth and irradiance of 227±10 Wcm^{-2} [91], even though it was later noted to be over-estimated [65]

Although recent progress has shown overall increase of both iPLQY and ePLQY, those values are still far from demonstrating a substantial benefit of UC when applied to silicon PV devices. The above mentioned results also show a significant difference between ePLQY and iPLQY values among Gd_2O_2S and β-$NaYF_4$. The two hosts are in fact affected by a considerable amount of scattering which reduces the absorption of the incoming light. Consequently, it is common to achieve high iPLQY values which corresponds to low ePLQY values, and the other way around [116]. However in the BaY_2F_8 sample scattering does not represent a limiting factor due to the possibility of synthesizing it in bulk crystalline form, as demonstrated by the small difference between ePLQY and iPLQY reported in [115].

The Er^{3+} concentration in the host plays a key role. A higher concentration decreases the average distance between the Er^{3+} ions which leads to higher probability of ET among these ions, but at the same time this enhances the probability of non-radiative cross-relaxation mechanisms [117]. Ways of limiting these losses have been extensively studied in literature and have been mainly focused on the search of low phonon energy hosts, synthesis of UC nanoparticles and optimization of the Er^{3+} ion doping level [97, 116, 118].

The aim of our experimental study is to analyze the UC luminescent properties of BaY_2F_8 samples under different monochromatic excitation wavelengths as a function of Er^{3+} concentrations and thicknesses. In particular we will show how the ePLQY and iPLQY can be optimized via minimization of self-absorption, a loss mechanism whose effect on a UC-PV device has been only theorized by the author of this thesis [93], and which is now experimentally demonstrated for the first time in a UC material.

6.2 Methodology

Er^{3+} doped BaY_2F_8 single crystal samples were grown by the Czochralski method in a concentration of 10at%, 20at% and 30at% using a self-made furnace developed by Physics Department Laboratories in Pisa. Growth powders with 99.999% purity level were used in order to avoid contamination affecting the optical quality of the crystals. Vacuum condition of 10^{-7} mBar and high-purity (99.999%) argon atmosphere were established before and during the growth process. A temperature of 972 °C, pulling rate 0.5 mm/h, rotation rate 5 rpm were used as growth parameters. After the growth, X-ray backscattering Laue diffractometry has been performed to check the crystallinity. Finally, the resulting crystals were cut and optically polished using a colloidal alumina (Al_2O_3) slurry consisting in 1 μm particles suspended in deionized water.

The samples prepared were: three samples of 10%Er:BaY_2F_8 with thickness (1.05±0.01) mm, (1.41±0.01) mm and (2.00±0.01) mm, three samples of 20%Er:BaY_2F_8 with thickness (0.49±0.01) mm, (1.25±0.01) mm and (2.05±0.01) mm and two samples of 30%Er:BaY_2F_8 with thickness (1.76±0.01) mm and (2.33±0.01) mm.

All spectroscopic measurements were carried out at room temperature (296 K). Absorption spectra in the NIR range of 950-1650 nm were measured with a spectrophotometer (Perkin-Elmer, Lambda 950) using a resolution of 0.5 nm. Fluorescence spectra were obtained using a calibrated spectrofluorometer (Edinburgh Instruments, FLS920) equipped with a NIR tunable laser (HP-Agilent, 8168-F) and a liquid nitrogen cooled NIR photo-multiplier tube (Hamamatsu, R5509-72). The laser tunability covers the range 1450-1590 nm. The laser beam was coupled into a optical fiber, collimated and then focused to the sample through a 50 mm focal length lens.

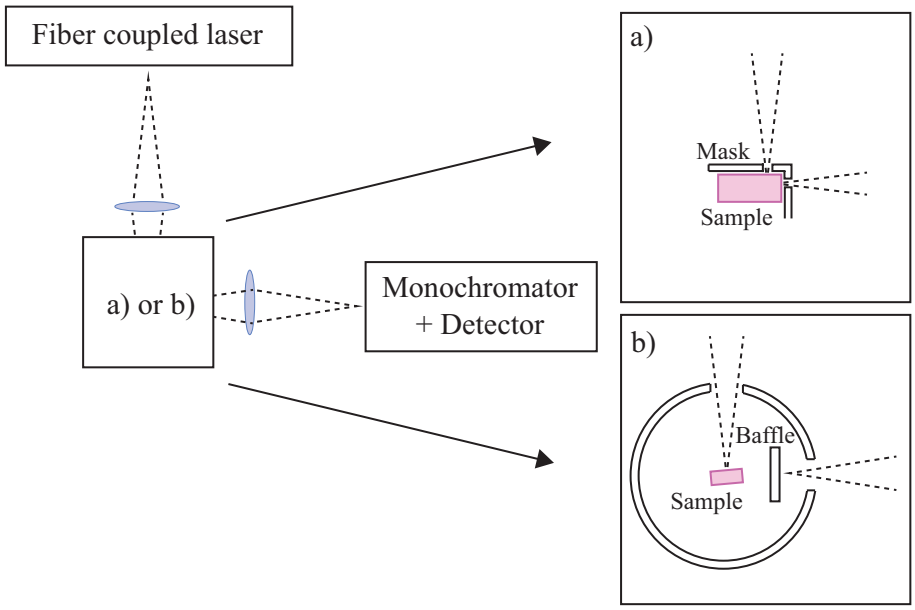

Figure 6.2: Experimental setups used for photoluminescence measurements, with (a) and without (b) integrating sphere.

As shown in Fig.6.2, ePLQY and iPLQY measurements were performed with the upconverting samples placed in a holder at the center of an integrating sphere (Jobin-Yvon). The sample holder had one hole of 3 mm diameter to allow the incident pump to enter and another one on the opposite side to allow the luminescence to exit. The uncertainty for the calibrated data is $\pm 3\%$ and the measurement accuracy on the ePLQY and iPLQY measurements is $\pm 5\%$ [65].

6.3 Results and Discussion

6.3.1 Absorption Measurements

The absorption spectra of the Er^{3+} doped BaY_2F_8 crystal measured for three different Er^{3+} doping levels (10%, 20% and 30%) are shown in Fig. 6.3. The spectra, corresponding to the excitation of the $^4I_{13/2}$ level from the ground state level $^4I_{15/2}$, extend over the range 1400-1650 nm. All three Er^{3+} doping levels present a similar distribution: the highest peak centered at 1493 nm, more peaks with a lower absorption coefficient distributed between 1520-1540 nm and an absorption tail extending up to 1650 nm.

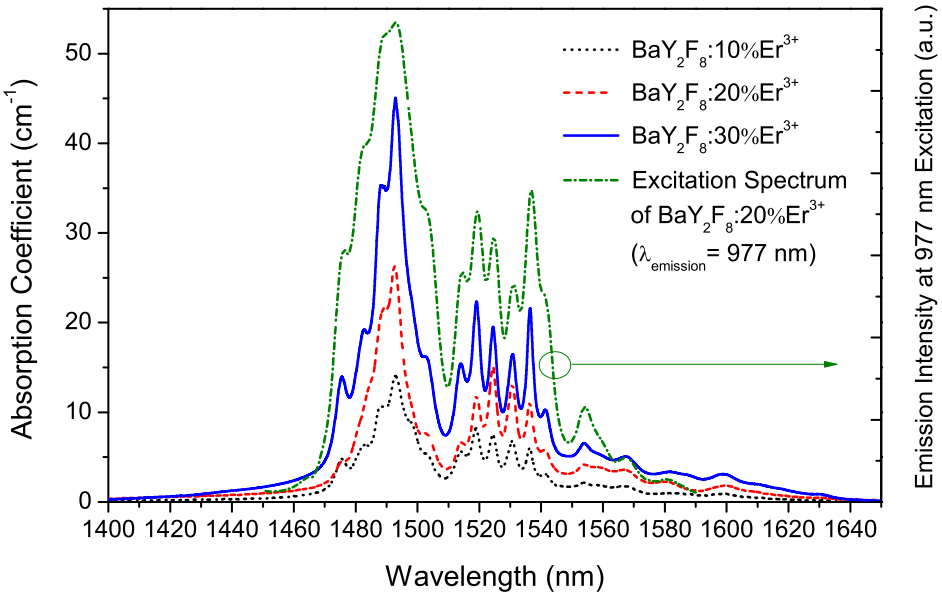

Figure 6.3: Absorption coefficient spectra in the range 1400-1650 nm of the investigated Er^{3+} doped BaY_2F_8 crystals for doping levels of 10%, 20% and 30%. The green dot-dashed curve represents the $^4I_{11/2} \rightarrow {}^4I_{15/2}$ excitation spectrum in the range 1450-1590 nm ($\lambda_{emission}$ = 977 nm) relative to a BaY_2F_8:20% Er^{3+} sample. All spectra have been measured at room temperature (296K).

The Er^{3+} absorption in BaY_2F_8 host is much stronger compared to β-$NaYF_4$ host. A 20% Er^{3+} doped β-$NaYF_4$ has its highest absorption peak at around 1523 nm with a value of 5.5 cm^{-1} [119], whereas a BaY_2F_8 with the same doping level

(20% Er^{3+}) has an absorption coefficient of 14.5 cm^{-1} at 1524 nm and it reaches 25 cm^{-1} at 1493 nm. As discussed previously, this difference is attributed to the negligible scattering by BaY_2F_8 crystal. Even if there are no records in literature of absorption coefficients values relative to Gd_2O_2S host, we suppose that also in this case the amount of scattering due to its microcrystalline nature reduces the absorption to lower levels with respect to BaY_2F_8. The absorption coefficient values for different Er^{3+} doping levels in BaY_2F_8 and at three different wavelengths (1493 nm, 1524 nm and 1556 nm) have been reported in Table 6.1. The selected wavelengths correspond to the excitations used in this work for the ePLQY and iPLQY determination presented in Section 6.3.2 and we will refer to those values later in the discussion.

Table 6.1: Absorption coefficients relative to three different Er^{3+} concentration and at different wavelengths.

Sample	@1556 nm	@1524 nm	@1493 nm
BaY_2F_8:10%Er^{3+}	2.0 cm^{-1}	7.3 cm^{-1}	14.0 cm^{-1}
BaY_2F_8:20%Er^{3+}	3.9 cm^{-1}	14.5 cm^{-1}	25.0 cm^{-1}
BaY_2F_8:30%Er^{3+}	5.8 cm^{-1}	18.5 cm^{-1}	46.0 cm^{-1}

Figure 6.3 also displays the excitation spectrum relative to a BaY_2F_8:20%Er^{3+} sample, which has been carried out tuning the laser excitation wavelength within the interval 1450-1590 nm (the maximum allowed by the tunable laser) and providing a constant power of 2.00±0.06 mW at each achievable wavelength. Its value is proportional to the emission intensity at 977 nm associated with the transition $^4I_{11/2} \rightarrow {}^4I_{15/2}$.

The highest peak of the excitation spectrum coincides with the highest absorption peak centered at 1493 nm, however in the excitation spectrum the peak results in a much wider profile. This effect can be ascribed to saturation caused by the high absorbance of the sample. It is important to stress the fact that the UC is a non-linear process which strongly depends on the energy density of the exciting radiation. The radiation provided by the Sun in the NIR range would not be sufficient

to enhance the UC process unless it is concentrated. This means that a UC-PV device would require to work in combination with a concentrating PV system. Thus, the available solar radiation for such a technology corresponds to the standard solar spectrum called air mass coefficient 1.5 direct (AM1.5D), which corresponds to the average direct component of the solar irradiance at mid-latitudes at a zenith angle of 48.2 degrees.

In Fig. 6.4 we compare the solar spectrum AM1.5D and the optical density of a 30% Er^{3+} doped BaY_2F_8 crystal extending in the wavelength interval of 1400-1650 nm.

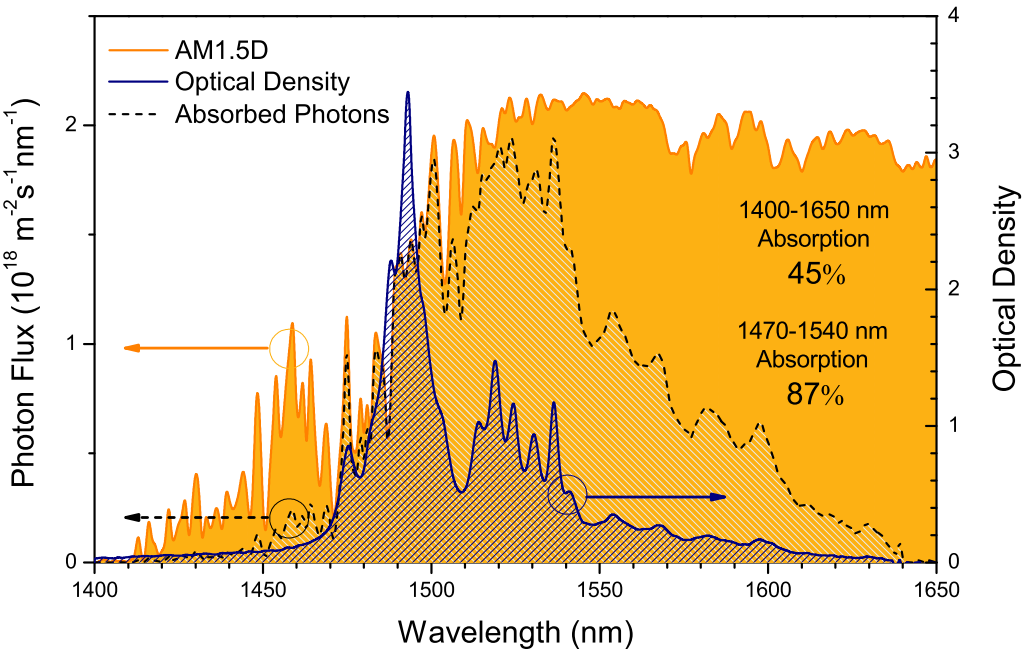

Figure 6.4: Comparison of solar spectrum AM1.5D (yellow area) and a 1.73 mm thickness BaY_2F_8:30%Er^{3+} optical density (blue patterned area) in the range 1400-1650 nm. The dotted black line represents the total solar photons absorbed by the sample.

According to Fig. 6.4, although NIR photons are provided by the Sun through the whole absorption window of the UC material, their distribution over this region results non-uniform. The amount of solar flux at sea level is reasonably constant only in the region between 1500 and 1650 nm with a value around $2{\cdot}10^{18}$ $m^{-2}s^{-1}nm^{-1}$. However, below 1500 nm the solar flux drops distinctly due to water vapor absorption

in the atmosphere [120]. As a consequence, the highest absorption peak around 1493 nm corresponds to an amount of solar flux which is 25% less with respect to the average value at longer wavelengths.

Due to the non optimal matching between the UC material absorption and the solar spectrum an UC-PV device would require a thick UC layer (order of mm) to absorb most of the NIR radiation. In the next section we will show instead that reducing the samples' thickness considerably reduce losses due to self-absorption and provide higher PLQYs. The absorbed solar photons by the sample achieving the best performances in terms of ePLQY (BaY_2F_8:30%Er^{3+} 1.76 mm thick) has been calculated using the absorbance and the AM1.5D spectrum. The UC sample would absorb only 45% of the total solar flux when considering the wavelength interval 1400-1650 nm. The percentage of absorbed solar photons would increase up to 87 % if the integration is reduced to the interval 1470-1540 nm.

6.3.2 Photoluminescence Quantum Yield Measurements

The NIR photoluminescence of Er^{3+} doped BaY_2F_8 was measured according to the pumping scheme of Fig. 6.1. The emission spectra of all samples were recorded under two different experimental situations, namely with and without integrating sphere (see Fig. 6.2). The measurement without the integrating sphere was set up such that the excitation beam was focused near the edge of the sample and the emission was collected perpendicularly from the adjacent side. This was done by using a mask with an entrance hole for the pump and another one for the collection. The mask also avoided the collection of photons emitted from other parts of the sample. By doing so, the length covered inside the sample by the detected photons was reduced, and consequently the probability of incurring a self-absorption loss was minimized. For this reason we assume that the photoluminescence spectra measured without using the integrating sphere are not affected by self-absorption.

The obtained photoluminescence spectrum without using the integrating sphere

measured under 1493 nm excitation of BaY_2F_8:20%Er^{3+} , relative to the transition $^4I_{11/2} \rightarrow ^4I_{15/2}$, and the ground state absorption spectrum of the same material, corresponding to the opposite process ($^4I_{15/2} \rightarrow ^4I_{11/2}$), are compared in Fig. 6.5.

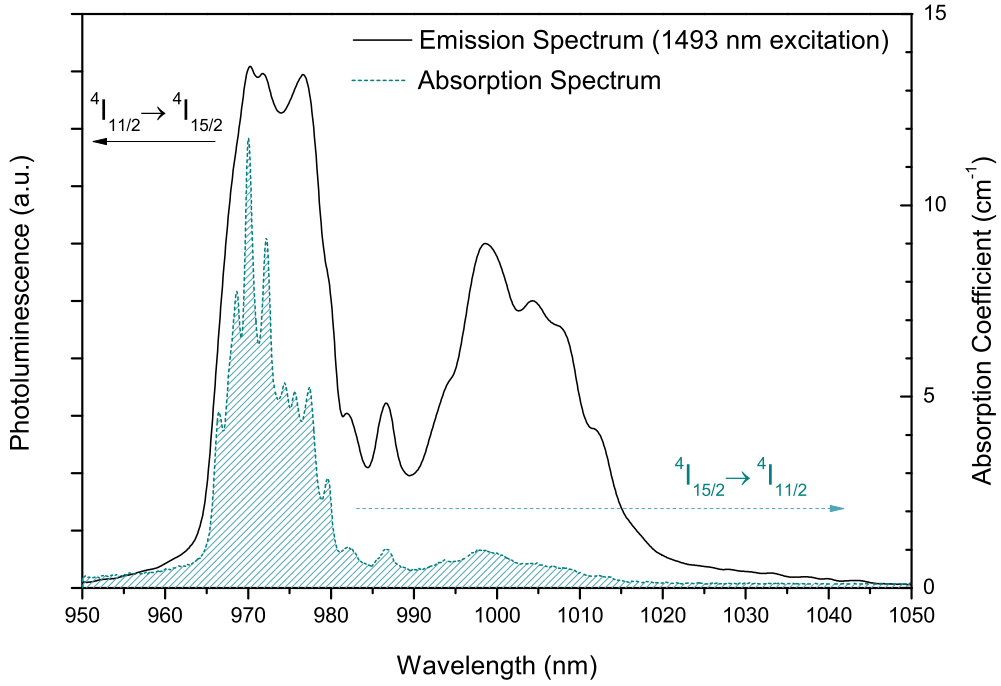

Figure 6.5: Comparison of emission spectrum (measured without integrating sphere) relative to the transition $^4I_{11/2} \rightarrow ^4I_{15/2}$ measured under 1493 nm excitation of BaY_2F_8:20%Er^{3+} (black solid line) and ground state absorption spectrum of the same material (blue patterned area) in the range 950-1050 nm.

The photoluminescence presented Fig. 6.5 is characterized by an emission distributed over two separated regions, one between 965-985 nm and the other in the interval 985-1020 nm. The region of shorter wavelengths originates from the radiative decay of electrons populating the lower levels of the $^4I_{11/2}$ manifold to the ground state, while the region of longer wavelengths is due to the radiative decay of electrons populating the highest levels of the same manifold, as represented in Fig. 6.1.

The ground state absorption spectra strongly overlap the emission spectrum in the interval 965-985 nm. At longer wavelengths there is still a weak absorption by Er^{3+} ions as the measurements were performed at room temperature. Hence, some of higher states at the top band of the manifold $^4I_{15/2}$ are populated by thermal

excitation ($kT \simeq 205$ cm^{-1} when $T = 296$K) increasing the probability of absorption not only from the exact ground state but from the whole manifold $^4I_{15/2}$.

Another key point emerging from Fig. 6.5 is that the emission at 977 nm reaches a peak intensity 1.5 times higher than the one centered around 1000 nm. In the following discussion we will show that, when the samples are measured using an integrating sphere, the emission peak intensities will change drastically due to the self-absorption affecting mainly the region around 977 nm.

The ePLQY and iPLQY measurements were performed on Er^{3+} doped BaY_2F_8 crystals using the integrating sphere setup as described in Chapter 3. All samples have been tested under the same excitation conditions. The focused beam size was measured using the 20/80 knife-edge scan technique [121, 122], resulting for each excitation wavelength in a spot diameter of (0.30±0.01) mm and a beam area of (7.1±0.5)·10^{-4} cm^2. A maximum power of 5.0±0.2 mW was achievable at each of the chosen wavelengths from the tunable laser, corresponding to a maximum irradiance of 7.0±0.7 Wcm^{-2}.

Figure 6.6 shows the NIR photoluminescence spectra measured for 3 different excitation wavelengths, 1556 nm, 1524 nm and 1493 nm, corresponding to increasing absorption coefficients (see Table 6.1 for their values). Each subplot (Figs. 6.6(a)–6.6(i)) corresponds to a particular excitation wavelength and a specific Er^{3+} doping level, and it contains the photoluminescence spectra measured for all different thicknesses available.

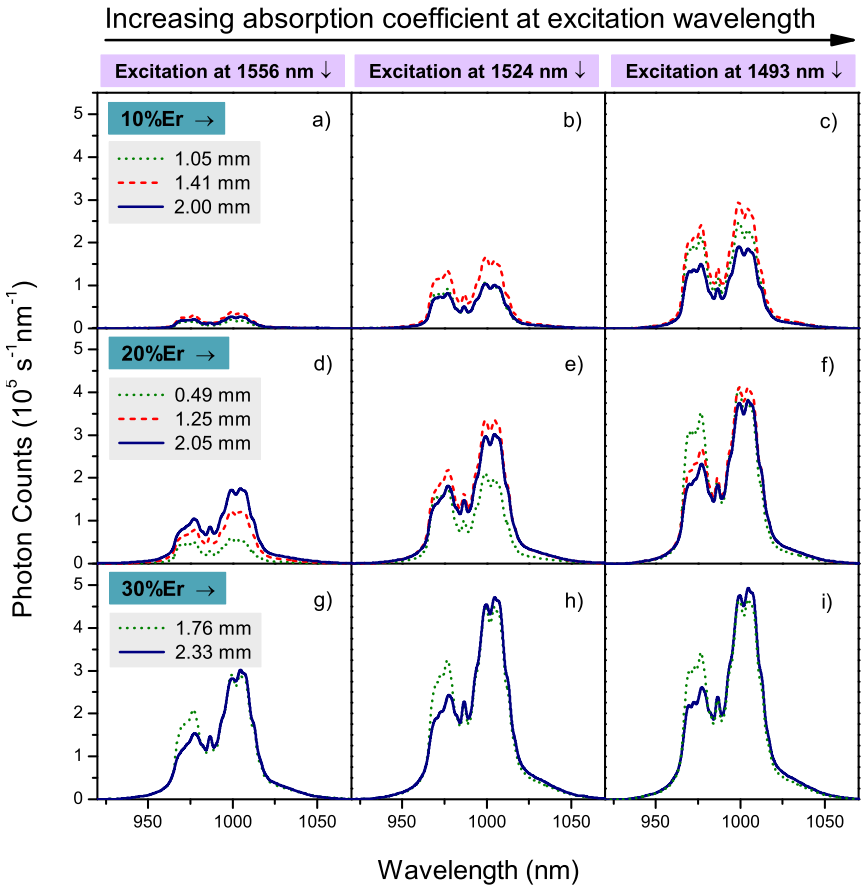

Figure 6.6: NIR photoluminescence spectra measured for 3 different excitations wavelengths: 1556 nm, 1524 nm and 1493 nm. Each subplot corresponds to a particular excitation wavelength and Er^{3+} doping level, and each one contains the emission spectra measured for different thicknesses (green-dotted for the thinnest sample, blue-solid for the thicker, and red-dashed for the middle thickness, when present). All spectra have been measured using the integrating sphere setup.

The area underneath each spectrum represents the overall flux of emitted photons with wavelength between 900 nm and 1100 nm which is directly proportional to the ePLQY of the samples, whose values are reported in Table 6.2. As previously anticipated, a common feature to all spectra reported in Fig. 6.6 is the substantial difference in the peak distribution with respect to the emission spectrum measured without integrating sphere presented in Fig. 6.5. For each spectrum the highest peak is now centered around 1005 nm, while the peak centered at 977 nm is affected by a drastic reduction in intensity, which is the peak where the overlap between absorption and emission spectra is stronger.

From a closer look to Figs. 6.6(d)–6.6(f) (spectra relative to BaY_2F_8:20%Er^{3+}

samples), an interesting effect is also observed. The ePLQY changes drastically within different thicknesses and different excitation wavelengths. It can be noticed that for 1556 nm excitation the thicker sample (2.05 mm) gives the highest ePLQY. Exciting at 1524 nm the same sample is now the second best, while at 1493 nm excitation is the lowest.

The existence of an optimal thickness depending on the excitation pump together with the drastic reduction of the emission around 977 nm suggest that self-absorption has a huge impact on the ePLQY of the UC material. The optimal thickness variation with different excitations is related to the fact that the absorption coefficient varies depending on the pump wavelength and Er^{3+} concentration. A higher absorption coefficient is equivalent to a high attenuation of the pump beam, meaning that most of the UC luminescence is originating from the ions present in the first hundreds of μm. In the case of 1493 nm excitation in a 20%Er^{3+} sample the absorption coefficient is 25 cm^{-1}, which means that at least 63% of the radiation is absorbed after 0.40 mm. Therefore, samples thicker than this value will increase the absorption but also the probability of incurring in self-absorption. In the case of 1556 nm excitation where the absorption coefficient results 3.9 cm^{-1}, the same amount of pump absorption is reached after 2.56 mm. This explain why the 20%Er^{3+} sample of thickness 2.05 mm had the highest ePLQY at 1556 nm but the lowest at 1493 nm. An analytical model which describes more in detail how self-absorption and optimal thickness are related was presented in the case of a downconverter material in [123].

Table 6.2: ePLQY and iPLQY (in brackets) values measured for all investigated samples and corresponding to 3 different excitation wavelenghts: 1556 nm, 1524 nm and 1493 nm. All measures are affected by an error of ±5%. The highest ePLQY and iPLQY values are highlighted in bold.

Sample	Ex. at 1556 nm	Ex. at 1524 nm	Ex. at 1493 nm
10%Er 1.05 mm	0.5 % (2.9 %)	2.7 % (5.3 %)	6.1 % (8.2 %)
10%Er 1.41 mm	0.9 % (3.9 %)	4.1 % (6.6 %)	7.2 % (8.6 %)
10%Er 2.00 mm	0.7 % (2.3 %)	2.6 % (3.6 %)	4.8 % (5.2 %)
20%Er 0.49 mm	1.5 % (10.1%)	5.3 % (10.9%)	10.1% **(14.6%)**
20%Er 1.25 mm	3.0 % (8.3 %)	8.4 % (10.3 %)	10.2% (10.9%)
20%Er 2.05 mm	4.4 % (8.4 %)	7.6 % (8.2 %)	9.5 % (9.7 %)
30%Er 1.76 mm	7.6 % (12.3%)	11.7% (12.5%)	**12.1%** (12.4%)
30%Er 2.33 mm	6.3 % (10.1%)	11.6% (12.1%)	12.1% (12.4%)

A similar behavior can be observed also for the 10%Er^{3+} samples (see Figs. 6.6(a)–6.6(c)), while for the 30%Er^{3+} samples (Figs. 6.6(g)–6.6(i)) the only appreciable effect is the increased emission at shorter wavelengths for the thinnest sample, sugesting that probably we were too far from finding an optimal thickness in this case. However, the BaY_2F_8:30%Er^{3+} samples (1.76 mm thick) reached the highest ePLQY of 12.1±1.2 % for excitation at 1493 nm, corresponding to a iPLQY value of 12.4%, which instead is not the highest overall.

The absolute highest iPLQY value has been observed in the BaY_2F_8:20%Er^{3+} of thickness 0.49 mm reaching the value of 14.6±1.5 %, which correspond to a ePLQY of 10.1±1.0 %. We suppose that highest iPLQY values are achievable using thinner BaY_2F_8:30%Er^{3+} samples, compared to the ones used in this work, but this was not possible to investigate due to unavailability of material.

6.3.3 Estimation of Self-Absorption Losses

An experimental method to quantitatively estimate the amount of losses due to self-absorption is presented in this section. In order to do so, each spectrum measured at a given excitation and given Er^{3+} concentration has been normalized so as to equalize the emission value at 1020 nm. This specific wavelength was chosen by referring to Fig. 6.5. The wavelength 1020 nm correspond to a spectral region in which the absorption coefficient is nearly absent (less than 0.1 cm^{-1} for each concentration) but a considerable amount of emission is still present. Therefore, all the emitted photons at 1020 nm and longer than this value are in a "self-absorption free" spectral region and its shape will not be affected by this loss mechanism.

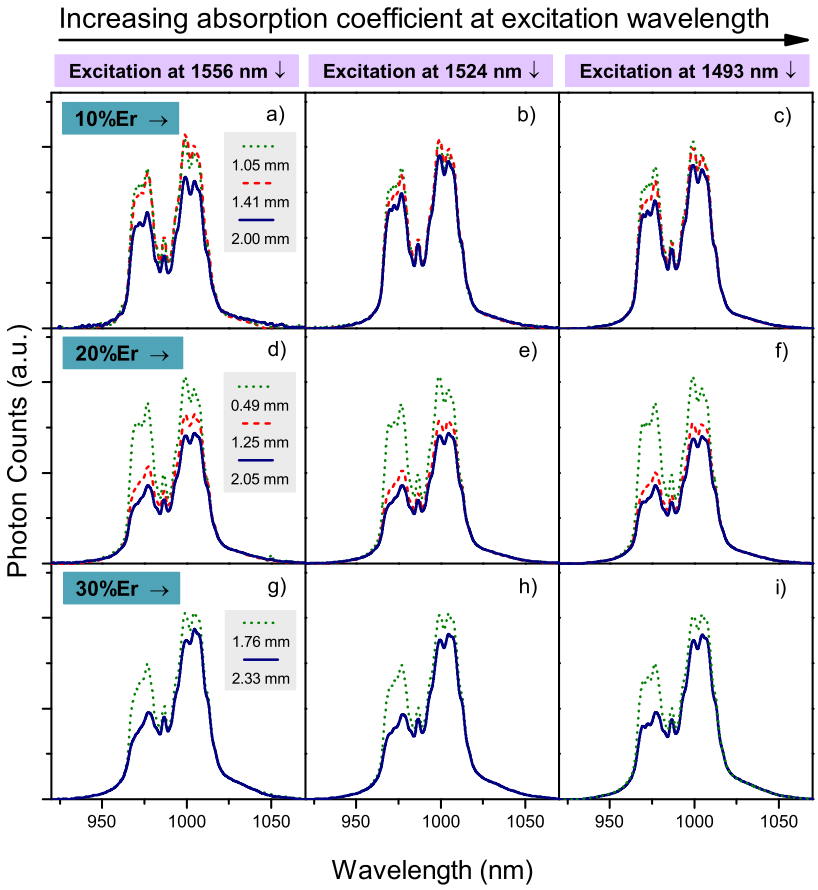

Figure 6.7: Normalized NIR photoluminescence spectra measured for 3 different excitations wavelengths: 1556 nm, 1524 nm and 1493 nm. Each subplot corresponds to a particular excitation wavelength and Er^{3+} doping level, and each one contains the normalized emission spectra measured for different thicknesses (green-dotted for the thinner sample, blue-solid for the thicker, and red-dashed for the middle thickness, when present).

This method has been already used by Ahn *et al.* [124] and Wilson *et al.* [125] to correct luminescence emission spectra in organic dyes from self-absorption losses. Applying the normalization to all measured spectra of Fig. 6.6 we obtain a new set of plots, which are represented in Fig. 6.7. According to Fig. 6.7, without any exception, the emission at shorter wavelengths (around 977 nm) tends to increase the ratio with respect to the longer wavelengths region (around 1005 nm) as the sample get thinner. As an example, in Figs. 6.7(d)–6.7(f) the emission around 1005 nm for the 2.05 mm sample is always much greater than the other, while in the 0.49 mm sample the two peaks intensity are almost equal. Hence, the ratio approaches the unity, which is still lower than the value of 1.5 calculated from Fig. 6.5, which represents a measurement not affected by self-absorption losses.

Moreover, the total intensity, which is in this case related to the iPLQY, is also increasing in thinner samples. On the whole, the measured spectra displayed in Fig. 6.7 indicates that reducing the samples' thickness the losses due to self-absorption can be reduced, but not completely eliminated. Using the same normalization method we compare the emission spectra of the thinnest samples for each Er^{3+} doping level (measured in the integrating sphere) with the emission measured without the integrating sphere, for which the self-absorption losses can be neglected.

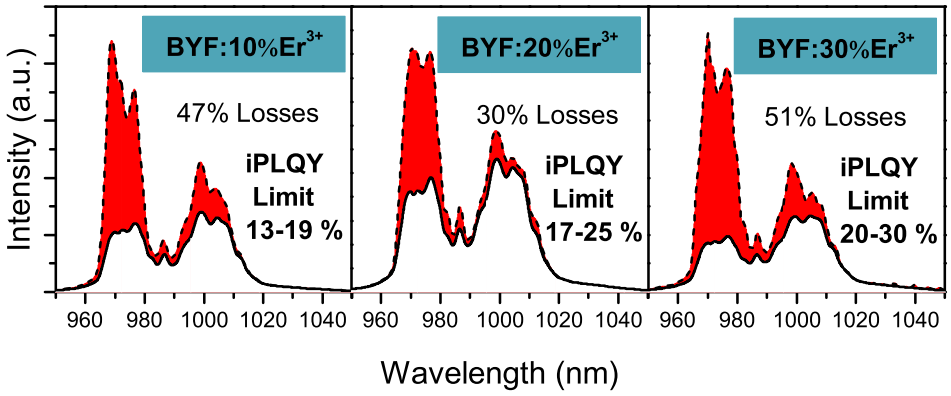

Figure 6.8: Estimated losses due to self-absorption comparing the integrated emission spectra measured in the integrating sphere (black solid line and white area) and without integrating sphere (black dash line and red area). The losses and the iPLQY limit estimation refer to the highest iPLQY samples investigated: BaY_2F_8:10%Er (1.05 mm), BaY_2F_8:20%Er (0.49 mm) and BaY_2F_8:30%Er (1.76 mm).

The results are shown in Fig. 6.8, and the percentage of losses due to self-absorption has been estimated from the ratio of the total areas. Estimated losses of 47%, 30% and 51% have been calculated for 10%Er^{3+} , 20%Er^{3+} and 30%Er^{3+} samples, respectively.

Finally, correcting the measured iPLQY of the thinnest samples (see Table 6.2) for the estimated losses we can derive the iPLQY limit (self-absorption losses equal to zero) for each concentration. iPLQY limit values resulted from the correction are in the range of 13-19 %, 17-25 % and 20-30 %, for 10%Er^{3+} , 20%Er^{3+} and 30%Er^{3+} doping level, respectively.

The normalisation has been tested also for wavelengths longer than 1020 nm up to 1050 nm to verify that our results are not affected by our particular selection. We found that the resulting normalization factors at each wavelength move away from the one calculated at 1020 nm with a relative error less than 5%. The 5% relative error due to the normalization has been taken into account when estimating the losses, resulting in a final relative error of 20%.

It results that in order to entirely remove self-absorption the sample has to be as thin as possible, but it is evident that this extreme case would reduce the pump absorption producing low ePLQY values. The finding of an optimal thickness provides the right balance between the absorption at the excitation wavelength and the minimization of self-absorption losses, but this is not enough to eliminate completely those losses.

6.4 Conclusions

In summary, we presented measurements of iPLQY and ePLQY of a Er^{3+} doped BaY_2F_8 crystal, in order to evaluate its potential for photovoltaics applications. The highest ePLQY measured in this study was 12.1±1.2 % for a BaY_2F_8:30at%Er^{3+} sample of thickness 1.75±0.01 mm, while the highest iPLQY corresponding to 14.6±1.5 % was measured in a BaY_2F_8:20at%Er^{3+} sample with a thickness of 0.49±0.01 mm. Both values were obtained under excitation at 1493 nm and an irradiance of 7.0±0.7 Wcm^{-2}. The reported iPLQY and ePLQY values are among the highest achieved in the case of a monochromatic excitation.

The UC process in this material resulted very efficient due to the low presence of defects and impurities, negligible scattering and low phonon energies of the fluoride BaY_2F_8 host (∼420 cm^{-1} [126]), which contribute to an overall reduction of non-radiative losses.

We also demonstrated that a optimal thickness exists for different cases depending on both the Er^{3+} concentration and the excitation wavelength in order to maximize the ePLQY, showing that losses due to self-absorption are substantially high. Those losses have been estimated through a normalization method in order to evaluate the maximum iPLQY achievable by the UC materials. The estimated iPLQY limit values were ∼16%, ∼21% and ∼25%, for 10%, 20% and 30% Er^{3+} doping level, respectively.

The outcome of this study suggests that thinner 30% Er^{3+} samples, compared to the one used in this work, might produce iPLQY values up to 30%. Despite of this, achieving such a value requires the use of very thin samples with low absorbance resulting in ePLQY values more likely closer to 20%. However, as predicted by the same author in [93], the reflective layer present in a UC-PV device (see Fig. 6.1) could increase the pump absorption and reduce the self-absorption losses achieving higher ePLQYs with respect to the one we can measure through photoluminescence measurements.

Another strategy that the authors suggest in order to increase the absorption would be to fabricate higher doped Er^{3+} samples, as from our study it is not clear what is the optimal Er^{3+} doping level to be used. Nevertheless, a higher Er^{3+} concentration will increase the probability for an emitted photon to be reabsorbed, or to incur into additional non-radiative losses like cross-relaxation.

Chapter 7

Conclusions

In summary, we presented a study with the aim of minimising the losses within luminescent materials coming from self-absorption of the emitted radiation. Application of DC materials to solar cells represents a challenging area. The inability to demonstrate a DC-PV device is due to the fact that the intrinsic losses happening in a DC material compete against the DC process itself. The losses coming from the self-absorption of the emitted radiation were analysed using a specifically-developed 1D optical model.

The results showed that an optimal thickness and an optimal doping concentration of the ions participating in the DC process exist in order to minimise the self-absorption and enhance the PLQY of the material. The validation through experimental measurements on DC borate glasses co-doped with Ce^{3+}-Yb^{3+} demonstrates the consistency of this model, which could be also applied to other spectral conversion systems, such as those based on luminescent downshifting and upconverting materials, but also for other technologies involving luminescent materials containing highly absorbing dopants such as Yb^{3+} ions.

We also have quantified the impact of self-absorption on the ePLQY for an UC system. The results showed that, also in a UC material, an optimal sample thickness is required to maximize the ePLQY. Two different cases have been compared; the

first in which the ePLQY of the material is measured in an integrating sphere and the second in which the effective ePLQY of a UC layer attached to the back side of a bifacial solar cell is considered. From the comparison it follows that, under optimal operating conditions, the ePLQY measured through an integrating sphere may result in an underestimation with respect to the performance that the UC material could achieve in a UC-PV device.

Moreover, it has been found that the optimal thickness and the ions' molar concentration are inversely proportional, suggesting that the condition on the optimal working condition can be translated to an optimal number of Er^{3+} ions present within the volume excited by the incident pump beam.

We presented measurements of iPLQY and ePLQY of a Er^{3+} doped BaY_2F_8 crystal, in order to evaluate its potential for UC-PV devices. The highest ePLQY measured in this study was 12.1±1.2 % for a BaY_2F_8:30at%Er^{3+} sample of thickness 1.75±0.01 mm, while the highest iPLQY corresponding to 14.6±1.5 % was measured in a BaY_2F_8:20at%Er^{3+} sample with a thickness of 0.49±0.01 mm. Both values were obtained under excitation at 1493 nm and an irradiance of 7.0±0.7 Wcm^{-2}. The reported iPLQY and ePLQY values are among the highest achieved in the case of a monochromatic excitation.

We also demonstrated that an optimal thickness exists for different cases depending on both the Er^{3+} concentration and the excitation wavelength in order to maximize the ePLQY, showing that losses due to self-absorption are substantially high. Those losses have been estimated through a normalization method in order to evaluate the maximum iPLQY achievable by the UC materials. The estimated iPLQY limit values were ∼16%, ∼21% and ∼25%, for 10%, 20% and 30% Er^{3+} doping level, respectively.

Bibliography

[1] United Nations, Department of Economic and Social Affairs, Population Division, *World Population Prospects: The 2012 Revision*, 2013. http://esa.un.org/unpd/wpp/.

[2] United Nations, Department of Economic and Social Affairs, Population Division, *World Urbanization Prospects: The 2014 Revision*, 2015. http://esa.un.org/unpd/wup/.

[3] International Energy Agency, *Key world energy statistics*, 2014. http://www.iea.org/publications/freepublications/publication/key-world-energy-statistics-2014.html.

[4] M. Höök and X. Tang, "Depletion of fossil fuels and anthropogenic climate change - a review," *Energy Policy*, vol. 52, pp. 797–809, 2013.

[5] R. L. Keeney and D. Winterfeldt, "Managing nuclear waste from power plants," *Risk analysis*, vol. 14, no. 1, pp. 107–130, 1994.

[6] G. Resch, A. Held, T. Faber, C. Panzer, F. Toro, and R. Haas, "Potentials and prospects for renewable energies at global scale," *Energy Policy*, vol. 36, no. 11, pp. 4048–4056, 2008.

[7] O. Morton, "Solar energy: A new day dawning?: Silicon valley sunrise," *Nature*, vol. 443, no. 7107, pp. 19–22, 2006.

[8] W. G. J. H. M. van Sark, G. W. Brandsen, M. Fleuster, and M. P. Hekkert, "Analysis of the silicon market: Will thin films profit?," *Energy Policy*, vol. 35, no. 6, pp. 3121–3125, 2007.

[9] A. Slade and V. Garboushian, "27.6% efficient silicon concentrator cell for mass production," in *Technical Digest, 15th International Photovoltaic Science and Engineering Conference, Shanghai*, vol. 701, 2005.

[10] W. Hoffmann, "Pv solar electricity industry: Market growth and perspective," *Solar energy materials and solar cells*, vol. 90, no. 18, pp. 3285–3311, 2006.

[11] A. Shalav, B. S. Richards, and M. A. Green, "Luminescent layers for enhanced silicon solar cell performance: Up-conversion," *Solar Energy Materials and Solar Cells*, vol. 91, no. 9, pp. 829–842, 2007.

[12] W. Shockley and W. Read Jr, "Statistics of the recombinations of holes and electrons," *Physical Review*, vol. 87, no. 5, pp. 835–842, 1952.

[13] W. Shockley and H. J. Queisser, "Detailed balance limit of efficiency of p-n junction solar cells," *Journal of Applied Physics*, vol. 32, no. 3, pp. 510–519, 1961.

[14] M. A. Green, K. Emery, Y. Hishikawa, W. Warta, and E. D. Dunlop, "Solar cell efficiency tables (version 45)," *Progress in photovoltaics: research and applications*, vol. 23, no. 1, pp. 1–9, 2015.

[15] C. H. Henry, "Limiting efficiencies of ideal single and multiple energy gap terrestrial solar cells," *Journal of Applied Physics*, vol. 51, no. 8, pp. 4494–4500, 1980.

[16] S. W. Glunz, R. Preu, and D. Biro, *Comprehensive renewable energy*, ch. Crystalline Silicon Solar Cells–State-of-the-Art and Future Developments, pp. 353–387. Elsevier, 2012.

[17] M. A. Green, *Third generation photovoltaics*. Springer, 2006.

[18] G. Conibeer, "Third-generation photovoltaics," *Materials Today*, vol. 10, no. 11, pp. 42–50, 2007.

[19] G. F. Brown and J. Wu, "Third generation photovoltaics," *Laser & Photonics Reviews*, vol. 3, no. 4, pp. 394–405, 2009.

[20] A. Braun, N. Szabó, K. Schwarzburg, T. Hannappel, E. A. Katz, and J. M. Gordon, "Current-limiting behavior in multijunction solar cells," *Applied Physics Letters*, vol. 98, no. 22, p. 223506, 2011.

[21] A. E. Becquerel, "Mémoire sur les effets électriques produits sous l'influence des rayons solaires," *Comptes rendus des séances hebdomadaires*, vol. 9, pp. 561–567, 1839.

[22] W. G. Adams and R. Day, "The action of light on selenium.," *Proceedings of the Royal Society of London*, vol. 25, no. 171-178, pp. 113–117, 1876.

[23] C. E. Fritts, "A new form of selenium cell," *American Journal of Science*, vol. 26, pp. 465+, 1883.

[24] A. Einstein, "Über einen die erzeugung und verwandlung des lichtes betreffenden heuristischen gesichtspunkt," *Annalen der Physik*, vol. 322, no. 6, pp. 132–148, 1905.

[25] R. A. Millikan, "A direct photoelectric determination of planck's "h"," *Physical Review*, vol. 7, pp. 355–388, 1916.

[26] J. Perlin, "Silicon solar cell turns 50," tech. rep., National Renewable Energy Lab., Golden, CO.(US), 2004.

[27] M. Lundstrom, "Introduction to photovoltaics," Presented at NCN Summer School , Purdue University, West Lafayette, Indiana, USA, 2011.

[28] National Renewable Energy Laboratory, National Center for Photovoltaics, *Research Cell Efficiency Records*, 2015. http://www.nrel.gov/ncpv/.

[29] A. Poullikkas, "Technology and market future prospects of photovoltaic systems," *International Journal of Energy and Environment*, vol. 1, no. 4, pp. 617–634, 2010.

[30] M. A. Green, "Silicon solar cells: state of the art," *Philosophical Transactions of the Royal Society of London A: Mathematical, Physical and Engineering Sciences*, vol. 371, no. 1996, 2013.

[31] D. M. Bagnall and M. Boreland, "Photovoltaic technologies," *Energy Policy*, vol. 36, no. 12, pp. 4390–4396, 2008.

[32] T. Saga, "Advances in crystalline silicon solar cell technology for industrial mass production," *NPG asia materials*, vol. 2, no. 3, pp. 96–102, 2010.

[33] R. Noufi and K. Zweibel, "High-efficiency cdte and cigs thin-film solar cells: highlights and challenges," in *Photovoltaic Energy Conversion, Conference Record of the 2006 IEEE 4th World Conference on*, vol. 1, pp. 317–320, IEEE, 2006.

[34] M. A. Green, "Third generation photovoltaics: Ultra-high conversion efficiency at low cost," *Progress in Photovoltaics: Research and Applications*, vol. 9, no. 2, pp. 123–135, 2001.

[35] R. D. Schaller and V. I. Klimov, "High efficiency carrier multiplication in pbse nanocrystals: implications for solar energy conversion," *Physical Review Letters*, vol. 92, no. 18, p. 186601, 2004.

[36] A. Luque, A. Martí, and C. Stanley, "Understanding intermediate-band solar cells," *Nature Photonics*, vol. 6, no. 3, pp. 146–152, 2012.

[37] P. Würfel, "Solar energy conversion with hot electrons from impact ionisation," *Solar Energy Materials and Solar Cells*, vol. 46, no. 1, pp. 43–52, 1997.

[38] T. Bauer, *Thermophotovoltaics: basic principles and critical aspects of system design*. Springer Science & Business Media, 2011.

[39] T. M. Clarke and J. R. Durrant, "Charge photogeneration in organic solar cells," *Chemical reviews*, vol. 110, no. 11, pp. 6736–6767, 2010.

[40] U. Rau, D. Abou-Ras, and T. Kirchartz, *Advanced characterization techniques for thin film solar cells*. John Wiley & Sons, 2011.

[41] P. Würfel, "The chemical potential of radiation," *Journal of Physics C: Solid State Physics*, vol. 15, no. 18, p. 3967, 1982.

[42] S. R. Taylor, "Abundance of chemical elements in the continental crust: a new table," *Geochimica et Cosmochimica Acta*, vol. 28, no. 8, pp. 1273 – 1285, 1964.

[43] A. J. Freeman and R. E. Watson, "Theoretical investigation of some magnetic and spectroscopic properties of rare-earth ions," *Physical Review*, vol. 127, no. 6, pp. 2058–2075, 1962.

[44] B. R. Judd, "Optical absorption intensities of rare-earth ions," *Physical Review*, vol. 127, no. 3, pp. 750–761, 1962.

[45] G. S. Ofelt, "Intensities of crystal spectra of rare-earth ions," *The Journal of Chemical Physics*, vol. 37, no. 3, pp. 511–520, 1962.

[46] G. H. Dieke and H. M. Crosswhite, "The spectra of the doubly and triply ionized rare earths," *Applied optics*, vol. 2, no. 7, pp. 675–686, 1963.

[47] F. Auzel, "Upconversion and anti-stokes processes with f and d ions in solids," *Chemical Reviews*, vol. 104, no. 1, pp. 139–174, 2004.

[48] T. Miyakawa and D. L. Dexter, "Cooperative and stepwise excitation of luminescence: Trivalent rare-earth ions in yb^{3+}-sensitized crystals," *Physical Review B*, vol. 1, pp. 70–80, 1970.

[49] T. Trupke, M. A. Green, and P. Würfel, "Improving solar cell efficiencies by down-conversion of high-energy photons," *Journal of Applied Physics*, vol. 92, no. 3, pp. 1668–1674, 2002.

[50] V. Badescu, A. De Vos, A. M. Badescu, and A. Szymanska, "Improved model for solar cells with down-conversion and down-shifting of high-energy photons," *Journal of Physics D: Applied Physics*, vol. 40, no. 2, p. 341, 2007.

[51] A. De Vos, A. Szymanska, and V. Badescu, "Modelling of solar cells with down-conversion of high energy photons, anti-reflection coatings and light trapping," *Energy Conversion and Management*, vol. 50, no. 2, pp. 328–336, 2009.

[52] Z. R. Abrams, A. Niv, and X. Zhang, "Solar energy enhancement using down-converting particles: A rigorous approach," *Journal of Applied Physics*, vol. 109, no. 11, p. 114905, 2011.

[53] V. Badescu, "An extended model for upconversion in solar cells," *Journal of Applied Physics*, vol. 104, no. 11, p. 113120, 2008.

[54] A. C. Atre and J. A. Dionne, "Realistic upconverter-enhanced solar cells with non-ideal absorption and recombination efficiencies," *Journal of Applied Physics*, vol. 110, no. 3, p. 034505, 2011.

[55] C. M. Johnson and G. J. Conibeer, "Limiting efficiency of generalized realistic c-si solar cells coupled to ideal up-converters," *Journal of Applied Physics*, vol. 112, no. 10, p. 103108, 2012.

[56] J. A. Briggs, A. C. Atre, and J. A. Dionne, "Narrow-bandwidth solar upconversion: Case studies of existing systems and generalized fundamental limits," *Journal of Applied Physics*, vol. 113, no. 12, p. 124509, 2013.

[57] C. M. Johnson, S. Woo, and G. J. Conibeer, "Limiting efficiency of erbium-based up-conversion for generalized realistic c-si solar cells," *Photovoltaics, IEEE Journal of*, vol. 4, no. 3, pp. 799–806, 2014.

[58] M. Yamane and Y. Asahara, *Glasses for photonics*. Cambridge University Press, 2000.

[59] D. Chen, Y. Wang, Y. Yu, P. Huang, and F. Weng, "Quantum cutting downconversion by cooperative energy transfer from Ce^{3+} to Yb^{3+} in borate glasses," *Journal of Applied Physics*, vol. 104, no. 11, p. 6105, 2008.

[60] G. Mueller, "The Czochralski method - where we are 90 years after Jan Czochralskis invention," *Crystal Research and Technology*, vol. 42, no. 12, pp. 1150–1161, 2007.

[61] M. Born and E. Wolf, "Principles of optics, 7th (expanded) ed," 1999.

[62] Perkin Elmer, *Inside the Perkin Elmer LAMBDA 950/850/650 Series*. http://www.perkinelmer.co.uk/lab-solutions/.

[63] Edinburgh Instruments, *Introduction to the FLSP920 Series of Fluorescence Spectrometers*. https://www.edinst.com/products/fls920-upgrades/.

[64] W. S. Slutter, J. Marcovecchio, R. E. Heinz, and D. A. Kolb, "Czerny-Turner monochromator," 1993. US Patent 5,192,981.

[65] S. K. MacDougall, A. Ivaturi, J. Marques-Hueso, and B. S. Richards, "Measurement procedure for absolute broadband infrared up-conversion photoluminescent quantum yields: Correcting for absorption/re-emission," *Review of Scientific Instruments*, vol. 85, no. 6, p. 063109, 2014.

[66] Labsphere Inc., *Optical-grade Spectralon Reflectance Material*, 2015. https://www.labsphere.com/labsphere-products-solutions/materials-coatings-2/coatings-materials/spectralon/.

[67] Q. Y. Zhang and X. Y. Huang, "Recent progress in quantum cutting phosphors," *Progress in Materials Science*, vol. 55, no. 5, pp. 353–427, 2010.

[68] J.-M. Meijer, L. Aarts, B. M. van der Ende, T. J. H. Vlugt, and A. Meijerink, "Downconversion for solar cells in YF_3:Nd^{3+},Yb^{3+}," *Physical Review B*, vol. 81, no. 3, p. 035107, 2010.

[69] E. Klampaftis, D. Ross, K. R. McIntosh, and B. S. Richards, "Enhancing the performance of solar cells via luminescent down-shifting of the incident

spectrum: A review," *Solar Energy Materials and Solar Cells*, vol. 93, no. 8, pp. 1182–1194, 2009.

[70] D. Ross, E. Klampaftis, J. Fritsche, M. Bauer, and B. S. Richards, "Increased short-circuit current density of production line CdTe mini-module through luminescent down-shifting," *Solar Energy Materials and Solar Cells*, vol. 103, pp. 11–16, 2012.

[71] R. T. Wegh, H. Donker, E. V. D. Van Loef, K. D. Oskam, and A. Meijerink, "Quantum cutting through downconversion in rare-earth compounds," *Journal of luminescence*, vol. 87, pp. 1017–1019, 2000.

[72] R. T. Wegh, H. Donker, K. D. Oskam, and A. Meijerink, "Visible quantum cutting in $LiGdF_4$: Eu^{3+} through downconversion," *Science*, vol. 283, no. 5402, pp. 663–666, 1999.

[73] B. Liu, Y. Chen, C. Shi, H. Tang, and Y. Tao, "Visible quantum cutting in BaF_2:Gd,Eu via downconversion," *Journal of luminescence*, vol. 101, no. 1, pp. 155–159, 2003.

[74] G. Lakshminarayana, H. Yang, S. Ye, Y. Liu, and J. Qiu, "Co-operative downconversion luminescence in Tm^{3+}/Yb^{3+}: SiO_2–Al_2O_3–LiF–GdF_3 glasses," *Journal of Physics D: Applied Physics*, vol. 41, no. 17, p. 175111, 2008.

[75] C. Feldmann, T. Jüstel, C. R. Ronda, and D. U. Wiechert, "Quantum efficiency of down-conversion phosphor $LiGdF_4$:Eu," *Journal of luminescence*, vol. 92, no. 3, pp. 245–254, 2001.

[76] J. T. Van Wijngaarden, S. Scheidelaar, T. J. H. Vlugt, M. F. Reid, and A. Meijerink, "Energy transfer mechanism for downconversion in the (Pr^{3+}, Yb^{3+}) couple," *Physical Review B*, vol. 81, no. 15, p. 155112, 2010.

[77] L. Aarts, B. M. Van der Ende, and A. Meijerink, "Downconversion for solar cells in $NaYF_4$: Er, Yb," *Journal of applied physics*, vol. 106, no. 2, p. 023522, 2009.

[78] V. D. Rodríguez, V. K. Tikhomirov, J. Méndez-Ramos, A. C. Yanes, and V. V. Moshchalkov, "Towards broad range and highly efficient down-conversion of solar spectrum by Er^{3+}–Yb^{3+} co-doped nano-structured glass-ceramics," *Solar energy materials and solar cells*, vol. 94, no. 10, pp. 1612–1617, 2010.

[79] D. Chen, Y. Wang, Y. Yu, P. Huang, and F. Weng, "Near-infrared quantum cutting in transparent nanostructured glass ceramics," *Optics letters*, vol. 33, no. 16, pp. 1884–1886, 2008.

[80] J.-L. Yuan, X.-Y. Zeng, J.-T. Zhao, Z.-J. Zhang, H.-H. Chen, and X.-X. Yang, "Energy transfer mechanisms in Tb^{3+}, Yb^{3+} codoped Y_2O_3 downconversion phosphor," *Journal of Physics D: Applied Physics*, vol. 41, no. 10, p. 105406, 2008.

[81] T. T. Basiev, Y. V. Orlovskii, K. K. Pukhov, and F. Auzel, "Multiphonon relaxation of the energy of electronic excitation in optical crystals doped with rare-earth ions," *Laser Physics*, vol. 7, no. 6, pp. 1139–1152, 1997.

[82] X. Y. Huang, D. C. Yu, and Q. Y. Zhang, "Enhanced near-infrared quantum cutting in $GdBO_3$:Tb^{3+}, Yb^{3+} phosphors by Ce^{3+} codoping," *Journal of Applied Physics*, vol. 106, p. 113521, 2009.

[83] R. Reisfeld, "Inorganic ions in glasses and polycrystalline pellets as fluorescence standard reference materials," *US Department of Commerce*, pp. 203–225, 1973.

[84] P. Vergeer, T. J. H. Vlugt, M. H. F. Kox, M. I. Den Hertog, J. P. J. M. Van der Eerden, and A. Meijerink, "Quantum cutting by cooperative energy transfer in $Yb_xY_{1-x}PO_4$:Tb^{3+}," *Physical Review B*, vol. 71, no. 1, p. 014119, 2005.

[85] Q. Y. Zhang, C. H. Yang, and Y. X. Pan, "Cooperative quantum cutting in one-dimensional $(Yb_xGd_{1-x})Al_3(BO_3)_4$:$Tb^{3+}$ nanorods," *Applied Physics Letters*, vol. 90, no. 2, p. 1107, 2007.

[86] Q. Y. Zhang, C. H. Yang, Z. H. Jiang, and X. H. Ji, "Concentration-dependent near-infrared quantum cutting in $GdBO_3$:Tb^{3+},Yb^{3+} nanophosphors," *Applied Physics Letters*, vol. 90, no. 6, p. 1914, 2007.

[87] J. J. Eilers, D. Biner, J. T. Van Wijngaarden, K. Krämer, H.-U. Güdel, and A. Meijerink, "Efficient visible to infrared quantum cutting through down-conversion with the Er^{3+}–Yb^{3+} couple in $Cs_3Y_2Br_9$," *Applied Physics Letters*, vol. 96, no. 15, p. 151106, 2010.

[88] S. Guy, "Modelization of lifetime measurement in the presence of radiation trapping in solid-state materials," *Physical Review B*, vol. 73, no. 14, p. 144101, 2006.

[89] B. S. Richards, "Luminescent layers for enhanced silicon solar cell performance: Down-conversion," *Solar energy materials and solar cells*, vol. 90, no. 9, pp. 1189–1207, 2006.

[90] N. Dai, L. Hu, and P. Lu, "Effects of Yb ion concentration on the spectral properties of lead silica glasses," *Optics communications*, vol. 253, no. 1, pp. 151–155, 2005.

[91] S. K. W. MacDougall, A. Ivaturi, J. Marques-Hueso, K. W. Krämer, and B. S. Richards, "Ultra-high photoluminescent quantum yield of β-$NaYF_4$:10%Er^{3+} via broadband excitation of upconversion for photovoltaic devices," *Optics express*, vol. 20, no. 106, pp. A879–A887, 2012.

[92] F. Auzel, G. Baldacchini, L. Laversenne, and G. Boulon, "Radiation trapping and self-quenching analysis in Yb^{3+}, Er^{3+}, and Ho^{3+} doped Y_2O_3," *Optical Materials*, vol. 24, no. 1, pp. 103–109, 2003.

[93] A. Boccolini, J. Marques-Hueso, and B. S. Richards, "Self-absorption in up-converter luminescent layers: impact on quantum yield measurements and on designing optimized photovoltaic devices," *Optics Letters*, vol. 39, no. 10, pp. 2904–2907, 2014.

[94] M. Wermuth, T. Riedener, and H. U. Güdel, "Spectroscopy and upconversion mechanisms of $CsCdBr_3$:Dy^{3+}," *Physical Review B*, vol. 57, no. 8, p. 4369, 1998.

[95] A. Boccolini, R. Faoro, E. Favilla, S. Veronesi, and M. Tonelli, "BaY_2F_8 doped with Er^{3+}: An upconverter material for photovoltaic application," *Journal of Applied Physics*, vol. 114, no. 6, p. 064904, 2013.

[96] M. Pollnau, D. R. Gamelin, S. R. Lüthi, H. U. Güdel, and M. P. Hehlen, "Power dependence of upconversion luminescence in lanthanide and transition-metal-ion systems," *Physical Review B*, vol. 61, no. 5, p. 3337, 2000.

[97] A. Ivaturi, S. K. W. MacDougall, R. Martín-Rodríguez, M. Quintanilla, J. Marques-Hueso, K. W. Krämer, A. Meijerink, and B. S. Richards, "Optimizing infrared to near infrared upconversion quantum yield of β-$NaYF_4$:Er^{3+} in fluoropolymer matrix for photovoltaic devices," *Journal of Applied Physics*, vol. 114, no. 1, p. 013505, 2013.

[98] J. F. Suyver, A. Aebischer, S. García-Revilla, P. Gerner, and H. U. Güdel, "Anomalous power dependence of sensitized upconversion luminescence," *Physical Review B*, vol. 71, no. 12, p. 125123, 2005.

[99] P. Pérez-Higueras, E. Munoz, G. Almonacid, and P. G. Vidal, "High concentrator photovoltaics efficiencies: Present status and forecast," *Renewable and Sustainable Energy Reviews*, vol. 15, no. 4, pp. 1810–1815, 2011.

[100] K. Q. Le and S. John, "Synergistic plasmonic and photonic crystal light-trapping: Architectures for optical up-conversion in thin-film solar cells," *Optics express*, vol. 22, no. 101, pp. A1–A12, 2014.

[101] P. E. Keivanidis, S. Baluschev, G. Lieser, and G. Wegner, "Inherent photon energy recycling effects in the up-converted delayed luminescence dynamics of Poly (fluorene)–PtIIoctaethyl Porphyrin blends," *ChemPhysChem*, vol. 10, no. 13, pp. 2316–2326, 2009.

[102] L. Wondraczek, M. Batentschuk, M. A. Schmidt, R. Borchardt, S. Scheiner, B. Seemann, P. Schweizer, and C. J. Brabec, "Solar spectral conversion for improving the photosynthetic activity in algae reactors," *Nature communications*, vol. 4, 2013.

[103] E. Heumann, S. Bär, K. Rademaker, G. Huber, S. Butterworth, A. Diening, and W. Seelert, "Semiconductor-laser-pumped high-power upconversion laser," *Applied physics letters*, vol. 88, no. 6, p. 061108, 2006.

[104] K. S. Abedin, T. F. Taunay, M. Fishteyn, M. F. Yan, B. Zhu, J. M. Fini, E. M. Monberg, F. V. Dimarcello, and P. W. Wisk, "Amplification and noise properties of an erbium-doped multicore fiber amplifier," *Optics Express*, vol. 19, no. 17, pp. 16715–16721, 2011.

[105] F. Wang, Y. Han, C. S. Lim, Y. Lu, J. Wang, J. Xu, H. Chen, C. Zhang, M. Hong, and X. Liu, "Simultaneous phase and size control of upconversion nanocrystals through lanthanide doping," *Nature*, vol. 463, no. 7284, pp. 1061–1065, 2010.

[106] Y. Liu, D. Tu, H. Zhu, and X. Chen, "Lanthanide-doped luminescent nanoprobes: controlled synthesis, optical spectroscopy, and bioapplications," *Chemical Society Reviews*, vol. 42, no. 16, pp. 6924–6958, 2013.

[107] H.-Q. Wang, M. Batentschuk, A. Osvet, L. Pinna, and C. J. Brabec, "Rare-earth ion doped up-conversion materials for photovoltaic applications," *Advanced Materials*, vol. 23, no. 22-23, pp. 2675–2680, 2011.

[108] G. Liu, "Advances in the theoretical understanding of photon upconversion in rare-earth activated nanophosphors," *Chemical Society Reviews*, vol. 44, no. 6, pp. 1635–1652, 2015.

[109] P. Gibart, F. Auzel, J.-C. Guillaume, and K. Zahraman, "Below band-gap IR response of substrate-free GaAs solar cells using two-photon up-conversion," *Japanese Journal of Applied Physics*, vol. 35, no. 8R, p. 4401, 1996.

[110] A. Shalav, B. S. Richards, T. Trupke, K. W. Krämer, and H. U. Güdel, "Application of $NaYF_4$: Er^{3+} up-converting phosphors for enhanced near-infrared silicon solar cell response," *Applied Physics Letters*, vol. 86, no. 1, p. 013505, 2005.

[111] B. S. Richards and A. Shalav, "Enhancing the near-infrared spectral response of silicon optoelectronic devices via up-conversion," *Electron Devices, IEEE Transactions on*, vol. 54, no. 10, pp. 2679–2684, 2007.

[112] S. Fischer, J. C. Goldschmidt, P. Löper, G. H. Bauer, R. Brüggemann, K. Krämer, D. Biner, M. Hermle, and S. W. Glunz, "Enhancement of silicon solar cell efficiency by upconversion: Optical and electrical characterization," *Journal of Applied Physics*, vol. 108, no. 4, p. 044912, 2010.

[113] F. Pellé, S. Ivanova, and J.-F. Guillemoles, "Upconversion of 1.54 μm radiation in Er^{3+} doped fluoride-based materials for c-Si solar cell with improved efficiency," *EPJ photovoltaics*, vol. 2, p. 20601, 2011.

[114] R. Martín-Rodríguez, S. Fischer, A. Ivaturi, B. Froehlich, K. W. Kramer, J. C. Goldschmidt, B. S. Richards, and A. Meijerink, "Highly efficient IR to NIR upconversion in Gd_2O_2S: Er^{3+} for photovoltaic applications," *Chemistry of Materials*, vol. 25, no. 9, pp. 1912–1921, 2013.

[115] S. Fischer, E. Favilla, M. Tonelli, and J. C. Goldschmidt, "Record efficient upconverter solar cell devices with optimized bifacial silicon solar cells and monocrystalline BaY_2F_8:30%Er^{3+} upconverter," *Solar Energy Materials and Solar Cells*, vol. 136, pp. 127–134, 2015.

[116] S. K. W. MacDougall, A. Ivaturi, J. Marques-Hueso, K. W. Krämer, and B. S. Richards, "Broadband photoluminescent quantum yield optimisation of Er^{3+}-doped β-$NaYF_4$ for upconversion in silicon solar cells," *Solar Energy Materials and Solar Cells*, vol. 128, pp. 18–26, 2014.

[117] S. Fischer, B. Fröhlich, K. W. Krämer, and J. C. Goldschmidt, "Relation between excitation power density and Er^{3+} doping yielding the highest absolute

upconversion quantum yield," *The Journal of Physical Chemistry C*, vol. 118, no. 51, pp. 30106–30114, 2014.

[118] R. Naccache, F. Vetrone, and J. A. Capobianco, "Lanthanide-doped upconverting nanoparticles: Harvesting light for solar cells," *ChemSusChem*, vol. 6, no. 8, pp. 1308–1311, 2013.

[119] S. Fischer, H. Steinkemper, P. Löper, M. Hermle, and J. C. Goldschmidt, "Modeling upconversion of erbium doped microcrystals based on experimentally determined einstein coefficients," *Journal of Applied Physics*, vol. 111, no. 1, p. 013109, 2012.

[120] J. E. McDonald, "Direct absorption of solar radiation by atmospheric water vapor," *Journal of Meteorology*, vol. 17, no. 3, pp. 319–328, 1960.

[121] J. M. Khosrofian and B. A. Garetz, "Measurement of a gaussian laser beam diameter through the direct inversion of knife-edge data," *Applied Optics*, vol. 22, no. 21, pp. 3406–3410, 1983.

[122] B. Cannon, T. S. Gardner, and D. K. Cohen, "Measurement of 1-μm diam beams," *Applied Optics*, vol. 25, no. 17, pp. 2981–2983, 1986.

[123] A. Boccolini, J. Marques-Hueso, D. Chen, Y. Wang, and B. Richards, "Physical performance limitations of luminescent down-conversion layers for photovoltaic applications," *Solar Energy Materials and Solar Cells*, vol. 122, pp. 8–14, 2014.

[124] T.-S. Ahn, R. O. Al-Kaysi, A. M. Müller, K. M. Wentz, and C. J. Bardeen, "Self-absorption correction for solid-state photoluminescence quantum yields obtained from integrating sphere measurements," *Review of Scientific Instruments*, vol. 78, no. 8, p. 086105, 2007.

[125] L. R. Wilson, B. C. Rowan, N. Robertson, O. Moudam, A. C. Jones, and B. S. Richards, "Characterization and reduction of reabsorption losses in luminescent solar concentrators," *Applied Optics*, vol. 49, no. 9, pp. 1651–1661, 2010.

[126] A. A. Kaminskii, O. Lux, J. Hanuza, H. Rhee, H. J. Eichler, J. Zhang, D. Tang, D. Shen, H. Yu, J. Wang, *et al.*, "Monoclinic β-BaY_2F_8 - a novel crystal simultaneously active for SRS and Ln^{3+}-ion lasing," *Laser Physics*, vol. 25, no. 1, p. 015801, 2014.